OPTIMIZING THE REFURBISHMENT PROCESS OF OLD 44 MVA HYDRO GENERATOR: A STUDY ON ALTERNATING WINDING TYPE AND VIBRATIONAL BEHAVIOR

A THESIS SUBMITTED TO
THE GRADUATE SCHOOL OF NATURAL AND APPLIED SCIENCES
OF
MIDDLE EAST TECHNICAL UNIVERSITY

BY

MUHAMMET SAMET YAKUT

IN PARTIAL FULFILLMENT OF THE REQUIREMENTS
FOR
THE DEGREE OF MASTER OF SCIENCE
IN
ELECTRICAL AND ELECTRONICS ENGINEERING

DECEMBER 2024

Approval of the thesis:

OPTIMIZING THE REFURBISHMENT PROCESS OF OLD 44 MVA HYDRO GENERATOR: A STUDY ON ALTERNATING WINDING TYPE AND VIBRATIONAL BEHAVIOR

submitted by **MUHAMMET SAMET YAKUT** in partial fulfillment of the requirements for the degree of **Master of Science in Electrical and Electronics Engineering Department, Middle East Technical University** by,

Prof. Dr. Naci Emre Altun
Dean, Graduate School of **Natural and Applied Sciences** _____

Prof. Dr. İlkay Ulusoy
Head of Department, **Electrical and Electronics Engineering** _____

Assoc. Prof. Dr. Ozan Keysan
Supervisor, **Electrical and Electronics Engineering, METU** _____

Examining Committee Members:

Prof. Dr. Murat Göl
Electrical and Electronics Engineering, METU _____

Assoc. Prof. Dr. Ozan Keysan
Electrical and Electronics Engineering, METU _____

Assist. Prof. Dr. Keyvan Firuzi
Electrical and Electronics Engineering, METU _____

Assist. Prof. Dr. Erhan Demirok
Electrical - Electronics Engineering, İzmir Katip Çelebi Uni. _____

Assist. Prof. Dr. Bülent Dağ
Electrical and Electronics Engineering, Gazi Uni. _____

Date: 30.12.2024

I hereby declare that all information in this document has been obtained and presented in accordance with academic rules and ethical conduct. I also declare that, as required by these rules and conduct, I have fully cited and referenced all material and results that are not original to this work.

Name, Surname: Muhammet Samet Yakut

Signature :

ABSTRACT

OPTIMIZING THE REFURBISHMENT PROCESS OF OLD 44 MVA HYDRO GENERATOR: A STUDY ON ALTERNATING WINDING TYPE AND VIBRATIONAL BEHAVIOR

Yakut, Muhammet Samet
M.S., Department of Electrical and Electronics Engineering
Supervisor: Assoc. Prof. Dr. Ozan Keysan

December 2024, 105 pages

Refurbishing hydro generators extends their lifespan and improves their efficiency. Aging machines often experience reduced reliability, lower efficiency, and frequent breakdowns, leading to significant economic challenges. The primary goals of refurbishment are to enhance cooling systems, upgrade materials, and improve performance. Modifying the winding configuration, although rare, can offer substantial benefits but often requires changes to the slot number, adding complexity to the redesign. Adjusting the slot number affects the slots per pole per phase ratio, which can significantly alter the machine's vibration characteristics. This study focuses on the refurbishment of a 68–year–old hydro generator, originally built by Westinghouse Electric Corporation in 1956 and equipped with lap windings. The proposed refurbishment replaces the lap windings with Roebel bars, necessitating a change in the slot number. Three alternative designs–270, 300, and 324 slots—-are evaluated, with one derived through multi-objective optimization, others through analytical design approach. While all designs achieve similar efficiencies of 98.1–98.3%, their vibration characteristics differ due to low–order spatial force harmonics caused by fractional slot windings. The 270 slot design exhibits dangerous vibration levels due

to a 6^{th} spatial harmonic close to the power frequency (100 Hz), raising mechanical stability concerns. The 300–slot design, however, offers the best balance between electromagnetic performance and vibration stability, making it the most viable option. This study provides valuable guideline for hydro generator designers by demonstrating the importance of addressing both electromagnetic and vibrational performance in refurbishment projects.

Keywords: Hydro generator, Refurbishment, Rewinding, Vibration

ÖZ

ESKİ 44 MVA HİDRO GENERATÖRÜN YENİLENMESİ SÜRECİNİN OPTİMİZASYONU: SARGI TİPİ DEĞİŞTİRME VE TİTREŞİM DAVRANIŞLARI ÜZERİNE BİR ÇALIŞMA

Yakut, Muhammet Samet
Yüksek Lisans, Elektrik ve Elektronik Mühendisliği Bölümü
Tez Yöneticisi: Doç. Dr. Ozan Keysan

Aralık 2024 , 105 sayfa

Hidro generatörlerin yenilenmesi kullanım ömürlerini uzatır ve verimliliklerini artırır. Eskiyen makineler genellikle daha az güvenilirlik, daha düşük verimlilik ve sık sık arıza yaşar ve bu da önemli ekonomik zorluklara yol açar. Yenilemenin birincil hedefleri soğutma sistemlerini geliştirmek, malzemeleri yükseltmek ve performansı artırmaktır. Sargı konfigürasyonunun değiştirilmesi nadiren de olsa önemli faydalar sağlayabilir, ancak genellikle slot sayısında değişiklik yapılmasını gerektirir ve bu da yeniden tasarıma karmaşıklık katar. Slot sayısının ayarlanması, faz başına kutup başına slot oranını etkiler ve bu da makinenin titreşim özelliklerini önemli ölçüde değiştirebilir. Bu çalışma, ilk olarak 1956 yılında Westinghouse Electric Corporation tarafından inşa edilen ve kapalı tip sargılarla donatılmış 68 yıllık bir hidro generatörün yenilenmesine odaklanmaktadır. Önerilen yenileme, kapalı tip sargıların Roebel sargılarıyla değiştirerek slot sayısında bir değişiklik yapılmasını gerektirmektedir. Üç alternatif tasarım – 270, 300 ve 324 slot– değerlendirilmiştir; bunlardan biri çok amaçlı optimizasyon, ikisi ise analitik tasarım yaklaşımı ile elde edilmiştir. Tüm tasarımlar

%98.1-98.3 arasında benzer verimlilikler elde ederken, kesirli slot sargılarının neden olduğu düşük dereceli uzaysal kuvvet harmonikleri nedeniyle titreşim özellikleri farklılık göstermektedir. 270 slotlu tasarım, güç frekansına (100 Hz) yakın bir 6. uzaysal harmonik nedeniyle tehlikeli titreşim seviyeleri sergilemekte ve mekanik stabilite endişelerini artırmaktadır. Bununla birlikte 300 slotlu tasarım, elektromanyetik performans ve titreşim kararlılığı arasında en iyi dengeyi sunarak en uygun seçenek haline gelmektedir. Bu çalışma, yenileme projelerinde hem elektromanyetik hem de titreşim performansının ele alınmasının önemini göstererek hidro generatör tasarımcıları için kılavuz görevi görmektedir.

Anahtar Kelimeler: Hidro generatör, Yenileme, Geri sarma, Titreşim

To my lovely family...

ACKNOWLEDGMENTS

First, I would like to express my sincere gratitude to Assoc. Prof. Dr. Ozan Keysan for mentorship, guidance, and endless support. This thesis would not be possible without his expertise and encouragement.

I would also like to thank dear committee members: Prof. Dr. Murat Göl, Assist. Prof. Dr. Erhan Demirok, Assist. Prof. Dr. Keyvan Firuzi, and Assist. Prof. Dr. Bülent Dağ for helping me to improve my thesis work.

I wish to express my heartfelt gratitude to Nail Tosun, Enes Ayaz, Yusuf Basri Yılmaz, Görkem Gülletutan, Yunus Çay, Ogün Altun, Özgür Gülsuna and Furkan Tokgöz for their invaluable contributions throughout this journey. Their instructive guidance, thoughtful insights, and our many enjoyable discussions significantly enriched my research experience. I am truly thankful for their collaboration and unwavering support, which made this process both enlightening and fulfilling. Moreover, I would like to thank everyone in METU PowerLab for creating an enjoyable atmosphere within the team.

I am also thankful to TÜBİTAK, the Scientific and Technological Research Council of Türkiye, for granting me their M.S studies scholarship, BİDEB 2210.

I sincerely thank my family for their endless encouragement, understanding, and love, which have been a constant source of strength and inspiration.

To my beloved wife, Miray: Your incredible patience and endless support have been the foundation of my strength throughout this journey. Your understanding and love have carried me through every challenge, and I am endlessly grateful for your unwavering presence by my side. You are my heart, my peace, and my greatest joy.

TABLE OF CONTENTS

ABSTRACT v

ÖZ vii

ACKNOWLEDGMENTS x

TABLE OF CONTENTS xi

LIST OF TABLES xiv

LIST OF FIGURES xvi

LIST OF ABBREVIATIONS xxi

CHAPTERS

1 INTRODUCTION TO HYDRO ELECTRICITY 1

1.1 Hydro Power in Turkey 2

1.2 Research Motivation 4

1.3 Outline of Thesis 5

2 UNDERSTANDING HYDRO GENERATORS 7

2.1 Electrically Excited Synchronous Machines 7

2.2 Main Structure of Hydro Generators 12

2.2.1 Stator Assembly 13

2.2.2 Rotor Assembly 16

3 DESCRIPTION AND ANALYTICAL MODELLING OF EXISTING GENERATOR 19

3.1 Generator Under Concern: Sarıyar Hydro Power Plant Unit III 20

3.2 Analytical Modelling of Existing Generator 26

3.3 Analytical Calculation of Characteristic Machine Reactances and Time Constants 32

3.4 Results & Discussions 39

4 ANALYTICAL DESIGN AND OPTIMIZATION OF REFURBISHMENT . 43

4.1 Design of Roebel Bar 43

4.2 Analytical Approach to Refurbishment and Alternating Winding Configuration for the Existing Generator 48

4.3 Optimization Algorithm: Non–Dominated Sorted Genetic Algorithm – II 57

4.4 Conclusion 62

5 FINITE ELEMENT VALIDATION AND VIBRATION ANALYSIS 67

5.1 Finite Element Modelling and Validation of Westinghouse Generator 67

5.1.1 Open–Circuit Curve of Existing Generator 71

5.1.2 Short–Circuit Curve of Existing Generator 73

5.2 Analytical Modelling of Vibrational Deformations 74

5.3 Vibration Characteristics of Generators 78

5.3.1 Airgap Magnetic Field Distribution 81

5.3.2 Radial Forces Exerting on the Stator 86

5.3.3 Vibration Levels of Generators 90

5.3.4 Cogging Torque and Zeroth Mode Deformation 92

5.4 Conclusions 94

6 CONCLUSIONS 97

6.1 Outcomes and Discussions 97

6.2 Potential Improvements and Future Work 100

REFERENCES 101

LIST OF TABLES

TABLES

Table 3.1 Characteristics of generator under concern. 21

Table 3.2 Dimensions of generator under concern. 25

Table 3.3 Comparison of copper losses (P_{cu}), core losses (P_{core}), and efficiency between commissioning test results and analytical model predictions.. 39

Table 3.4 Comparison of machine characteristic parameters between commissioning test results and analytical model predictions. 40

Table 4.1 Comparison of the electromagnetic performance of the existing generator equipped with Roebel bars. 51

Table 4.2 Amortization table for core material selection. 51

Table 4.3 Candidate designs for refurbishment. 53

Table 4.4 Comparison of existing and new design generators in terms of sizing, and winding configurations. 56

Table 4.5 Dimensions of the selected optimal design. 60

Table 4.6 Loss distribution of the selected optimal design. 62

Table 5.1 Winding type of design candidates. 78

Table 5.2 Reference machine parameters. 79

Table 5.3 Resonant frequencies for various modes, based on analytical calculations given between Equations (5.7)–(5.9). FEM calculation is 92.19 Hz for $h = 6$. 91

Table 5.4 Vibration analyses pertaining to the amplification of resonance for various slot numbers. 92

Table 5.5 Comparison of candidate machines in vibrational perspective. 95

Table 6.1 Comparison of vibration levels of 270 and 300 slot designs. 99

Table 6.2 Comparison of the existing Westinghouse generator and new design machine. 99

LIST OF FIGURES

FIGURES

Figure 1.1 Illustration of a typical hydropower plant, adapted from [1]. . . . 1

Figure 1.2 World's annual renewable energy sharing by years, adapted from [2]. 2

Figure 1.3 Hydro–power station installations over years in Turkey, adapted from [6]. 3

Figure 2.1 Basic representation of and EESM, adapted from [10]. 8

Figure 2.2 Salient–pole rotor EESM (a) and cylindirical rotor EESM (b). . . 9

Figure 2.3 Equivalent circuit of a typical electrically excited synchronous machine. 9

Figure 2.4 Phasor diagram of a cylindrical rotor electrically excited synchronous machine. 10

Figure 2.5 Phasor diagrams illustrating various operating modes of Electrically Excited Synchronous Machines (EESMs). 11

Figure 2.6 Rotor assembly of a hydro generator, adapted from [12]. 12

Figure 2.7 Stator assembly of a hydro generator, adapted from [13]. 13

Figure 2.8 Stator core lamination. 14

Figure 2.9 Slot packing of a hydro generator, adapted from [19]. 15

Figure 2.10 Sarıyar Hydro Power Plant Units–I and III: Generator installed by AEG (a) and Westinghouse (b). 15

Figure 2.11 Magnetic field distribution accross a slot, adapted from [16]. . . 16

Figure 2.12 Rotor pole assembly, adapted from [12]. 17

Figure 3.1 Sarıyar Hydro Power Plant Units–I and III: Generator installed by AEG (a) and Westinghouse (b). 19

Figure 3.2 Nameplate of the Sarıyar HPP Unit III 20

Figure 3.3 Fingers of the Westinghouse generator. 22

Figure 3.4 Comparison of winding configurations for Sarıyar Hydro Power Plant Unit III: (a) design from production documents and (b) current configuration in operation. 23

Figure 3.5 Dimensioning of the pole, adapted from [26]. 24

Figure 3.6 Winding factors of existing generator. 28

Figure 3.7 Flux and flux density distribution among a slot when rotor surface is assumed to be smooth, adapted from [10]. 29

Figure 3.8 Geometric variables related to windings used in reactance calculations, adapted from [31]. 34

Figure 3.9 Emprically determined demagnetizing factor with respect to ratio of pole embrace to pole pitch. 35

Figure 3.10 Geometric variables related to field leakage reactance, adapted from [31]. 36

Figure 3.11 Reduction ratios for zero, positive, and negative sequence reactances. The figure is adapted from [31]. 38

Figure 3.12 Open circuit test comparison of analytical and original machine. 40

Figure 4.1 Illustration of Roebel bar (a) and inverted–turn (b), adapted from [16]. 45

Figure 4.2 Illustration of slot leakage fluxes across a slot, adapted from [10]. 45

Figure 4.3 Eddy current distribution with respect to strand size, adapted from [16]. 46

Figure 4.4 B field distribution accross a slot. 47

Figure 4.5 Iterative Roebel bar design procedure. 49

Figure 4.6 Design methodology accounting for operational and structural limitations, adapted from [6]. 50

Figure 4.7 Temperature distribution along the axial length for the existing design (a) and the new design (b), with an ambient temperature of 25°C. 54

Figure 4.8 Flux density distribution of the new design. 55

Figure 4.9 Variation of AC and DC resistances with respect to number of strands. 55

Figure 4.10 Variation of stator copper loss and height of the strands with respect to number of strands. 56

Figure 4.11 Flowchart illustrating the optimization algorithm process. 60

Figure 4.12 Convergence among the generations of optimization algorithm. . 61

Figure 4.13 Distribution of optimal designs within the cost space. 62

Figure 4.14 Winding diagrams. 65

Figure 5.1 Finite element (FE) model of the existing Westinghouse generator (1/16 symmetry). 69

Figure 5.2 B field distribution of the existing Westinghouse generator. . . . 70

Figure 5.3 Pole–pair B field distribution of the existing Westinghouse generator. 70

Figure 5.4 Open–circuit (OC) curves of the original machine tested after manufacturing, compared with the finite element (FE) and analytical model results. 72

Figure 5.5 Open–circuit (OC) curves of the original machine commissioning test, compared with the on–site test conducted in 2023. 72

Figure 5.6 Sustained short–circuit curve of the Westinghouse generator, where I_a is rated armature current. 73

Figure 5.7 Visualization of mode numbers [43]. 77

Figure 5.8 Flux density distribution of the 270 slot machine, obtained from ANSYS Maxwell FE environment. 80

Figure 5.9 Flux density distribution of the 300 slot machine, obtained from ANSYS Maxwell FE environment. 80

Figure 5.10 Flux density distribution of the 324 slot machine, obtained from ANSYS Maxwell FE environment. 81

Figure 5.11 Airgap magnetic field under inductive load (lagging with 0.9 power factor). (a) and (b) are the results of existing generator, (c) and (d) are the 270 slot machine, (e) and (f) are the 300 slot machine, (g) and (h) are belonging to the 324 slot machine. 83

Figure 5.12 Spatial harmonic spectrum of airgap flux density. (a) and (b) are the results of existing generator, (c) and (d) are the 270 slot machine, (e) and (f) are the 300 slot machine, (g) and (h) are belonging to the 324 slot machine. 84

Figure 5.13 Spatial harmonic spectrum of airgap radial flux density. (a), (b), (c), and (d) are the results of existing generator with 240 slot, 270 slot, 300 slot, and 324 slot machines, respectively. 85

Figure 5.14 Radial force densities in the airgap. (a), (b), (c), and (d) are the results of existing generator, 270 slot, 300 slot, and 324 slot machines, respectively. 86

Figure 5.15 Spatial harmonic spectrum of radial force density. 87

Figure 5.16 Dangerous modes of radial force density. (a), (b), and (c) are the results of 270 slot, 300 slot, and 324 slot machines, respectively. 88

Figure 5.17 Eigenfrequency analysis of the investigated generator. 92

Figure 5.18 Cogging torques of reference (existing generator) and candidate machines. 93

LIST OF ABBREVIATIONS

AC	Alternating Current
DC	Direct Current
EESM	Electrically Excited Synchronous Machine
FE	Finite Element
FEA	Finite Element Analysis
FEM	Finite Element Method
GA	Genetic Algorithm
GCD	Greatest Common Divisor
HPP	Hydro Power Plant
MLT	Mean Length per Turn
MMF	Magneto–Motive Force
NSGA–II	Non–Dominated Sorting Genetic Algorithm – II
OC	Open Circuit
SC	Short Circuit
SCR	Short Circuit Ratio

CHAPTER 1

INTRODUCTION TO HYDRO ELECTRICITY

Hydropower plants (HPPs) convert the potential energy of water into electrical energy. Water stored in a dam is directed to the turbine through a pipe system known as a penstock. As the water moves through the pipes and turbine, its potential energy is converted into kinetic energy. The rotation of the turbine drives the shaft and, consequently, the rotor. The rotating magnetic field generated by the rotor induces the required voltage in the stator windings, thereby generating electricity. As the name suggests, a hydrogenerator refers to the rotor and stator assemblies used in this process. The overall configuration of a typical HPP is illustrated in Figure 1.1.

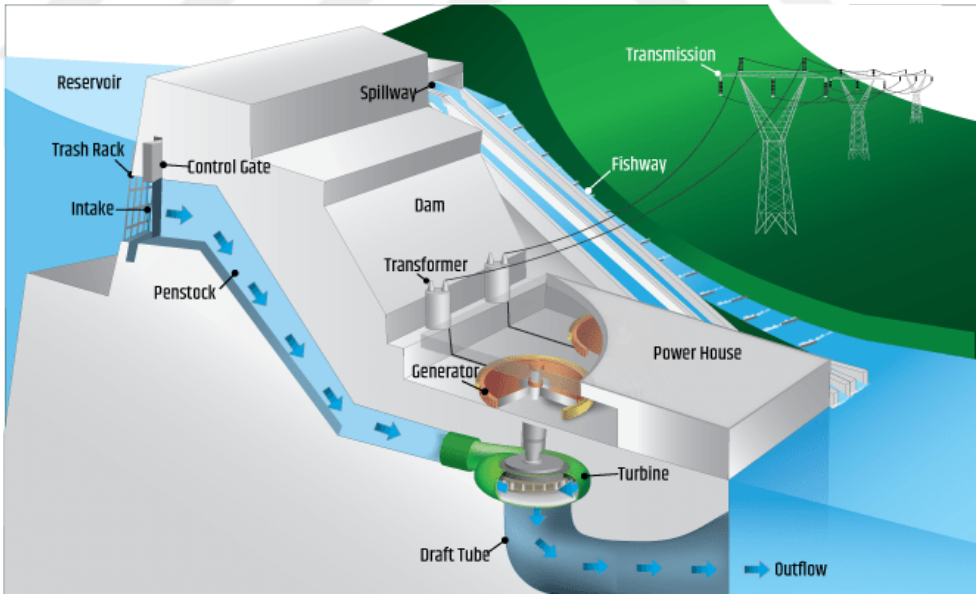

Figure 1.1: Illustration of a typical hydropower plant, adapted from [1].

Hydropower is the world's largest source of renewable energy, surpassing the combined output of other renewable sources [2, 3, 4]. It is projected to remain the domi-

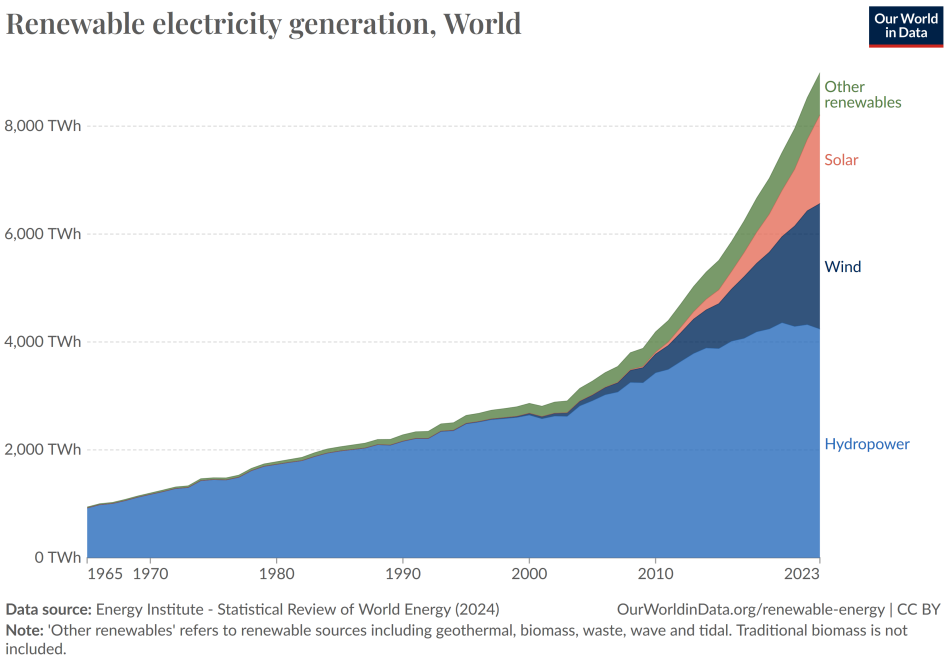

Figure 1.2: World's annual renewable energy sharing by years, adapted from [2].

nant renewable energy source until 2028. Consequently, hydropower plays an important role in decarbonizing the power system [3].

A key advantage of hydropower plants is their ability to serve as a dispatchable energy source. In other words, HPPs can provide backup support to other variable renewable energies, such as wind and solar. While solar and wind energy are expected to exceed hydropower in total capacity, hydropower will continue to play a significant role in the energy mix [3]. Figure 1.2 illustrates the total energy generated by the renewable energy resources. It is evident from Figure 1.2 that hydropower continues to play a crucial role among clean energy resources.

1.1 Hydro Power in Turkey

In Turkey, feasibility analyses and construction of hydroelectric power plants (HPPs) began in the early 20^{th} century. The country's first hydroelectric power plant, the Tarsus Dam, with an installed capacity of 60 kW, commenced operations in 1902. Following feasibility studies in the 1920s and 1930s, the State Hydraulic Works (DSİ)

was established. Subsequently, Turkey began constructing its first large–scale HPPs, Seyhan and Sarıyar, in 1956, with installed capacities of 59 MW and 160 MW, respectively.

This initial progress marked a significant increase in HPP investments, with installed capacity growing at an average rate of 10% per year between 1970 and 2020 [5]. During the latter half of the 20th century, Turkey's three largest HPPs—-Atatürk, Karakaya, and Keban—-began operations.

Figure 1.3 illustrates hydroelectric power stations in Turkey, organized by their commissioning dates and installed capacities. In the figure, both the horizontal axis and the size of the bubbles represent the installed power. Lateral lines indicate the age of the generators. The interested generator is located in Sarıyar HES(4x40 MW). The top three largest hydro–power stations, Ataturk HES, Karakaya HES, and Keban HES are also indicated in the graph. Of Turkey's total installed capacity of 24.35 GW, HPPs with over 60 years of operation contribute approximately 2%, while those with over 40 years account for 12.4% [6].

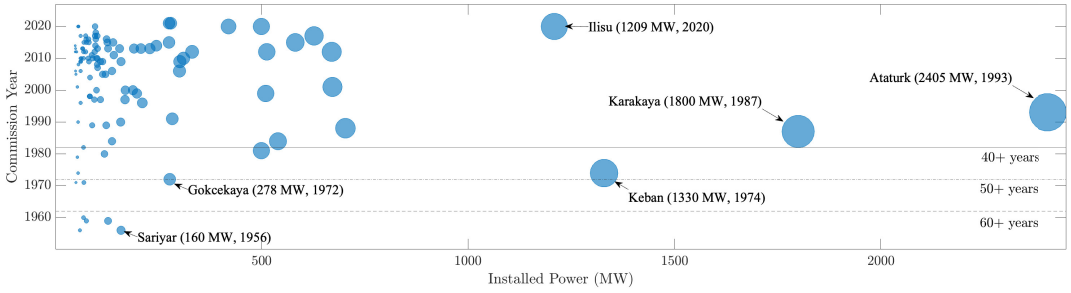

Figure 1.3: Hydro–power station installations over years in Turkey, adapted from [6].

As of the end of 2021, hydroelectric power plants accounted for 21.5% of electricity generation in Turkey [7]. The installed capacity of hydroelectric power is projected to reach 35.1 GW by 2035, allowing it to retain a substantial role in the energy mix despite the expansion of other renewable energy sources.

1.2 Research Motivation

The operational half–life of hydro generators typically ranges between 30 and 60 years, depending on the robustness of the original design and the operational stresses encountered throughout their service life. The generator's half–life is marked by the significant degradation or complete failure of one or more active electrical components. As a result, faults in hydro generators often increase notably after the first half–life. This period commonly represents the optimal time to undertake upgrades and capacity enhancements, as well as comprehensive refurbishment, to extend the generator's functional life for a "second half-life" [8].

As illustrated in Figure 1.3, approximately 31.9% of Turkey's hydroelectric power plants have reached their operational half–life [6]. Furthermore, the Ministry of Energy and Natural Resources indicates that Turkey is nearing its maximum hydroelectric capacity [7]. With both a significant number of HPPs reaching their half–life and the nation nearing its hydroelectric capacity, a strategic approach is needed to ensure the continued safe operation of HPPs and grid reliability. Upgrading or uprating hydro generators provides a cost–effective means to address these issues [8].

An upgrade to a hydro generator involves refurbishing the equipment without increasing output power, whereas an uprate includes both refurbishment and an increase in output power. Given that older hydro generators were often conservatively designed due to historical material limitations, power output increases of up to 25% are feasible [8]. However, increased output may necessitate upgrades to the switchyard and new licensing for the elevated power levels.

Generator refurbishment is time–intensive and may extend beyond a year. Considering the generator's downtime and lost energy generation, associated costs can be significant. Therefore, refurbishment processes should be streamlined to minimize downtime, ideally by replacing only essential components to expedite completion.

A further consideration is that generator size is often constrained by the existing concrete base constructed as part of the dam. Enlarging the generator would usually entail additional construction, which is often undesirable for operators due to substantial cost implications. Additionally, the maximum achievable power output is

constrained by the dam height, pipe capacity, and turbine design, limiting potential power increases during refurbishment.

Refurbishment efforts must also account for mechanical aspects to ensure long–term reliability. Altering the winding type of a hydro generator during refurbishment typically necessitates modifications to the slot number, which subsequently impacts the machine's vibrational characteristics due to changes in the spatial harmonic distribution of the airgap magnetic field [9]. Consequently, vibrational analysis becomes essential in such refurbishment projects. Where necessary, enhancements to structural components, such as the generator's frame, may be required to ensure extended operational life. As a result, most refurbishment processes presented in the literature generally avoid changes to the winding type [8].

Given these factors, the refurbishment of Turkey's hydro generators is essential, both due to the age of the installed fleet and the cost–effective capacity gains achievable through refurbishment. This study focuses on the refurbishment of an aged hydro generator located in Sarıyar, Ankara, specifically addressing a change in winding type. It proposes a systematic methodology for the refurbishment process, with particular emphasis on the vibrational behavior of the machine.

1.3 Outline of Thesis

Chapter 2 introduces the fundamental principles of electrically excited synchronous machines (EESMs), providing an overview of the main EESM topologies and their role in energy generation. This chapter also explains why EESMs are well–suited for applications in hydroelectric generation, where control over reactive power and voltage regulation are essential. Additionally, it covers hydro generators, detailing their components and structural configuration.

Chapter 3 focuses on the analytical modeling of the existing generator, with the purpose of understanding its current operational characteristics, identifying opportunities for efficiency optimization, and calculating characteristic parameters that inform design constraints. This chapter includes calculations of the machine's loadings, loss distributions, and efficiency, as well as an in-depth examination of characteristic re-

actances and time constants. The origins of alternating current (AC) copper losses and their calculation methods are also discussed.

Chapter 4 details the analytical optimization process using the non–dominated sorting genetic algorithm II (NSGA–II). The NSGA–II optimization method is employed to evaluate design trade–offs and prioritize candidate configurations that best balance output power, efficiency, and durability within the specified constraints. Generator sizing based on these limitations, along with the winding schematic, is addressed. Candidate designs are evaluated and presented.

Chapter 5 covers finite element method (FEM) and modelling including the validation of the analytical model through comparison with finite element analysis (FEA) results. The FEA results serve to provide critical insights into the generator's real–world performance, particularly in terms of magnetic flux density (B) distribution within the airgap and vibrational response. This chapter also evaluates the vibrational characteristics of the generator based on FEA results.

CHAPTER 2

UNDERSTANDING HYDRO GENERATORS

A typical electrical machine consists of two primary components: the stator and the rotor. Based on their stator and rotor designs, and operating principles, electrical machines can be classified into several types, including synchronous reluctance machines, permanent magnet machines, and electrically excited synchronous machines (EESMs). A hydro generator is a notable example of an EESM. To fully comprehend the operation of a hydro generator, it is essential to first understand the principles governing EESMs. This foundational knowledge allows for a more in–depth analysis of hydro generators and their performance.

2.1 Electrically Excited Synchronous Machines

Electrically excited synchronous machines (EESMs) are a class of electrical machines in which the magnetic field is generated by an externally supplied direct current (DC). A cross–sectional view of an EESM is presented in Figure 2.1. Electrical excitation is applied to the field windings around the rotor, and the combination of rotor rotation with the DC excitation produces a rotating magnetomotive force (MMF) within the airgap. This MMF induces a voltage in the stator windings, enabling energy conversion within the machine.

EESMs are widely favored in industrial applications due to their capacity for precise control over reactive power and voltage regulation, unlike permanent magnet machines. This ability to modulate excitation current makes them highly suitable for applications where constant speed under varying load conditions is essential. Furthermore, these machines offer flexible control over reactive power compensation,

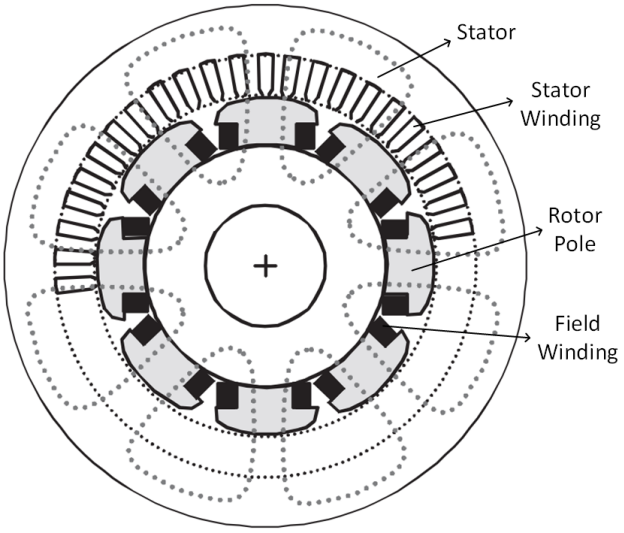

Figure 2.1: Basic representation of and EESM, adapted from [10].

making them integral in stabilizing power grids and regulating voltage profiles.

The stator of an EESM is typically composed of three–phase windings connected to an alternating current (AC) source. When the rotor's magnetic field rotates in synchrony with the stator's rotating magnetic field, the machine makes energy conversion–either mechanical to electrical or electrical to mechanical energy. The speed of this rotation is directly proportional to the frequency of the stator voltage and inversely proportional with the number of poles.

Electrically excited synchronous machines (EESMs) are classified into two main categories based on rotor pole configuration: cylindrical rotor and salient–pole rotor machines, which are shown in Figure 2.2. In cylindrical rotor EESMs, the rotor surface is smooth, with poles distributed evenly along the rotor's circumference, allowing for high–speed operation with minimal windage losses, making them suitable for applications such as steam turbine generators. In contrast, salient–pole rotor EESMs have poles that extend outward from the rotor, making them suitable for lower–speed applications, such as hydroelectric generators, where high torque is prioritized over speed.

Torque in synchronous machines can be written as:

$$T = \frac{1}{2}\mathbf{I}_\mathbf{t}^* \frac{d\mathbf{L}}{d\theta}\mathbf{I} \tag{2.1}$$

where $\mathbf{L}$ is the inductance matrix, and $\mathbf{I}$ is the current matrix. The inductance matrix is composed of both self and mutual inductances of the phases (L and M). In cylindrical rotor EESMs, the airgap is constant, which results in constant inductance with respect to position $\left(\frac{dL}{d\theta} = 0\right)$. On the other hand, airgap is varying due to rotor pole geometry in salient–pole EESMs, thus inductance is also changing with respect to position $\left(\frac{dL}{d\theta} \neq 0\right)$. Therefore, in cylindrical rotor EESMs, there is only synchronous torque $\left(\text{torque due to } \frac{dM}{d\theta} \text{ term}\right)$. As a result, utilizing both reluctance and synchronous torque enables the salient–pole machines to have higher torque density.

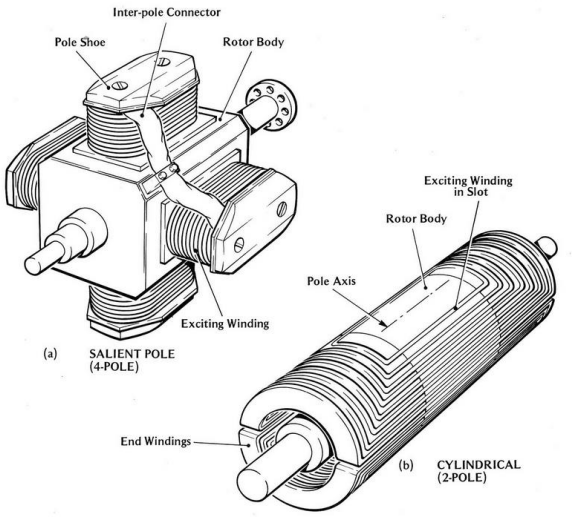

Figure 2.2: Salient–pole rotor EESM (a) and cylindirical rotor EESM (b).

A standard approach to analyze an electrically excited synchronous machine (EESM) involves the use of its per–phase equivalent circuit, as shown in Figure 2.3. In this

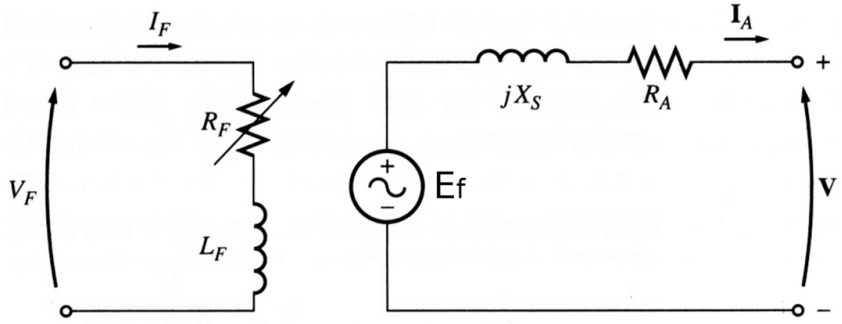

Figure 2.3: Equivalent circuit of a typical electrically excited synchronous machine.

figure, the left–side circuit represents the field circuit, while the right–side circuit depicts the stator (armature) circuit. Here, V_F denotes the applied DC field voltage, R_F the equivalent resistance of the field circuit, L_F the inductance of the field windings, and I_F the DC field current. For the stator circuit, E_f represents the induced voltage within the stator windings, and it is proportional with the I_F, if saturation is ignored. X_S is the synchronous armature reactance, R_A denotes the armature resistance, I_A is the armature current, and V is the terminal voltage of the stator.

To facilitate the analysis of the equivalent circuit, phasor diagrams are commonly employed. By converting the alternating current (AC) components into the phasor domain, the time dependency of the analysis is removed, allowing for a simplified approach using vectors. For illustrative purposes, an example phasor diagram is provided in Figure 2.4. In Figure 2.4, δ is defined as load angle, and θ is the power

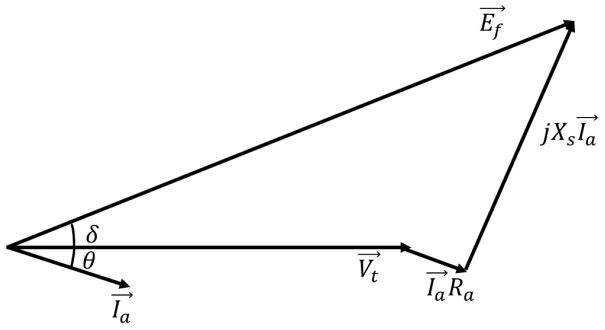

Figure 2.4: Phasor diagram of a cylindrical rotor electrically excited synchronous machine.

factor angle. Mathematically expressing the phasor diagram yields:

$$\vec{E_f} = \vec{V_t} \pm \vec{I_a}(R_a + jX_s) \tag{2.2}$$

Electrically excited synchronous machines (EESMs) can function as both a generator and a motor, depending on the phase angle between the induced voltage and the terminal voltage. When the induced voltage leads the terminal voltage, the machine operates in generator mode; conversely, if it lags, the machine operates in motor mode.

The machine is termed over–excited if the magnitude of the induced voltage exceeds the terminal voltage, whereas it is under–excited when the induced voltage is lower. This excitation level determines the direction of reactive power flow: reactive power flows from the over–excited side to the under–excited side. The various operating modes of an EESM are illustrated in Figure 2.5.

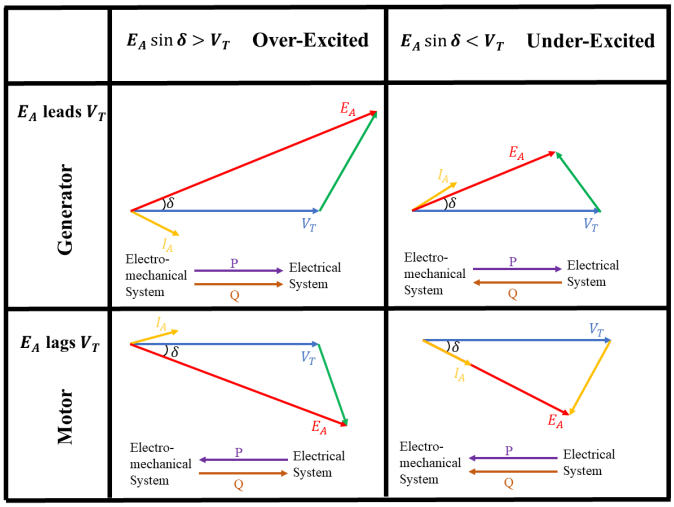

Figure 2.5: Phasor diagrams illustrating various operating modes of Electrically Excited Synchronous Machines (EESMs).

As illustrated in Figure 2.5, an over–excited machine supplies reactive power to the electrical system, while an under–excited machine absorbs reactive power from it. A notable application of Electrically Excited Synchronous Machines (EESMs) is in synchronous condensers, which are no-load synchronous machines used exclusively for reactive power compensation and grid voltage regulation. These condensers can operate in either over–excited or under–excited modes, depending on the required direction of reactive power flow to support system stability [11].

In addition to synchronous condensers, synchronous generators commonly operate in an over–excited mode to support voltage regulation and enhance grid stability. By providing or absorbing reactive power as needed, both synchronous condensers and generators play essential roles in maintaining voltage levels and stabilizing electrical networks.

Hydro generators serve as a prime example of Electrically Excited Synchronous Machines (EESMs) that play a critical role in maintaining grid stability. As previously noted, their rapid start–up and synchronization capabilities make hydro generators highly suitable as dispatchable energy resources. This responsiveness enables hydro generators to effectively support grid stability, offering quick adjustments to balance supply and demand in real time. Therefore, a thorough understanding of hydro generators and the ongoing maintenance of their operation are essential for ensuring grid stability and reliability.

2.2 Main Structure of Hydro Generators

As in the case of an EESM, hydro generator consists of two primary components: rotor and stator. The rotor is typically constructed using the magnetic core and the conductors wound around the salient–poles, which can be seen in Figure 2.6. The

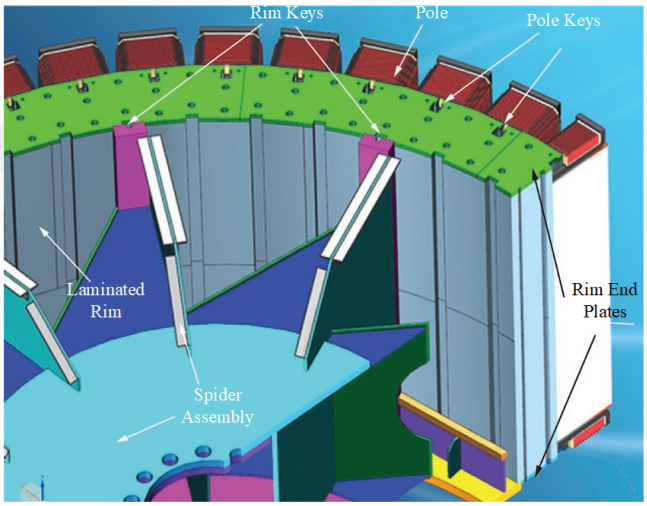

Figure 2.6: Rotor assembly of a hydro generator, adapted from [12].

rotor body and poles are made from magnetic material to guide and enhance the magnetic field. When direct current (DC) is applied to the pole windings, the rotational motion of the rotor generates a rotating magnetic field.

For voltage generation, the only remaining requirement is to place conductors within the varying magnetic field, which is the role of the stator. The stator, like the rotor, is constructed with a magnetic core and windings (see Figure 2.7). The windings

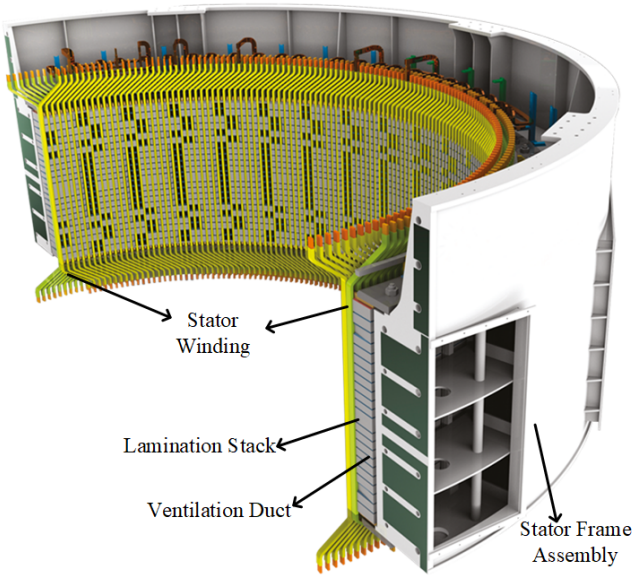

Figure 2.7: Stator assembly of a hydro generator, adapted from [13].

are housed in slots punched into the core, while the magnetic core itself amplifies the magnetic field within the air gap between the rotor and stator.

2.2.1 Stator Assembly

As previously discussed, stator is responsible for inducing necessary voltage with the help of rotating magnetic field. The stator is constructed with magnetic material, which is called core, and the windings are made up of copper.

The stator core is housed within the stator frame, which provides structural support against the forces acting on the core. Additionally, the stator frame bears the entire weight of the stator assembly [14]. The housing of the stator core is utilized via keybars placed in outer periphery of the stator core and welded to the stator frame. The generator's cooling units are also mounted on the outer perimeter of the stator frame [12].

To minimize eddy current losses caused by the varying magnetic field, the stator core is made from thinly laminated electrical steel (see Figure 2.8). These laminations are typically cut from silicon steel sheets using either punch presses or laser cutting techniques. Thickness of silicon steel sheets typically range between 0.35 mm to

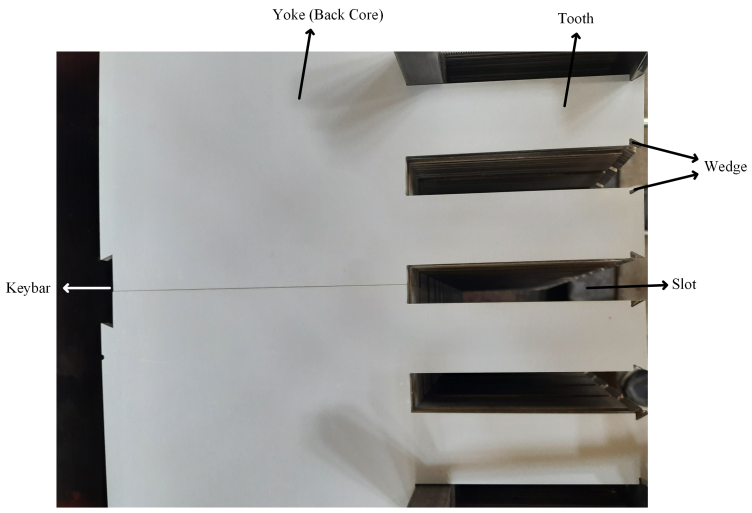

Figure 2.8: Stator core lamination.

0.50 mm [12]. The laminations are then stacked both radially and axially to form the stator core assembly.

In earlier designs, the laminations were stacked off–site to make the construction process easier. However, these pre–stacked stator cores were often sectioned into 2, 3, or 4 radial segments (or more, depending on the generator size) to facilitate transport. In modern designs, sectioning is avoided due to its negative impact on the structural stiffness and electromagnetic performance of the generator, resulting from the gaps between the sections [12, 14]. As a result, most generators today are constructed on–site without segmenting the stator core.

Stator windings are tasked with carrying the required current and withstanding the induced voltage in the stator. In hydro generators, they are typically configured in a three-phase star connection with a grounded neutral. The windings are usually designed as double-layer, fractional slot, and distributed types to facilitate manufacturing and minimize both time and space harmonic distortions. They are secured within the stator slots using wedges, ripple springs, spacers, and semiconductive paper (see Figure 2.9) [15, 16, 17, 18].

Stator windings can be made using either single–turn or multi–turn coils (as illustrated in Figure 2.10), with no difference in electromagnetic performance. The choice between these two designs is typically based on the manufacturing practices of the

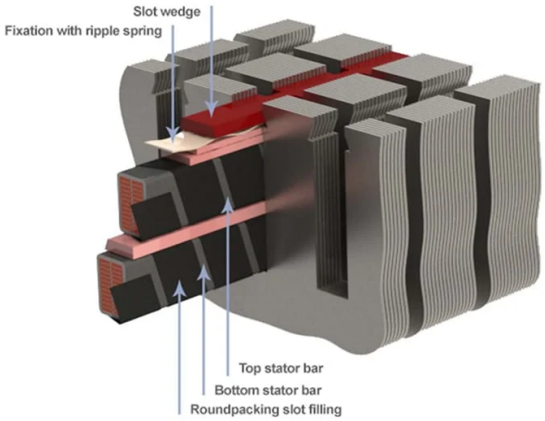

Figure 2.9: Slot packing of a hydro generator, adapted from [19].

producer or operator companies. Multi–turn coils are generally manufactured as diamond (or lap) windings, which is more suitable for mass production; however, they require the removal of more coils if a fault occurs in the windings [6, 15]. In contrast, single–turn coils are manufactured using Roebel bars, which are increasing production effort, offer significant time and cost savings during maintenance. Roebel bars are commonly used by European countries, whereas lap windings are generally used by American countries [16]. Regardless of coil type, all coils are constructed using strands to mitigate the skin effect. An example of stranded coils can be seen in Figure 2.11. In addition to the skin effect, circulating currents also arise within

(a) Roebel bar. (b) Diamond coil.

Figure 2.10: Sarıyar Hydro Power Plant Units–I and III: Generator installed by AEG (a) and Westinghouse (b).

the windings due to the non–homogeneous magnetic field distribution inside the slot.

This variation in magnetic flux density is primarily caused by slot leakage fluxes and the varying distance from the rotor [10]. An example of the magnetic flux density distribution across the slot is shown in Figure 2.11.

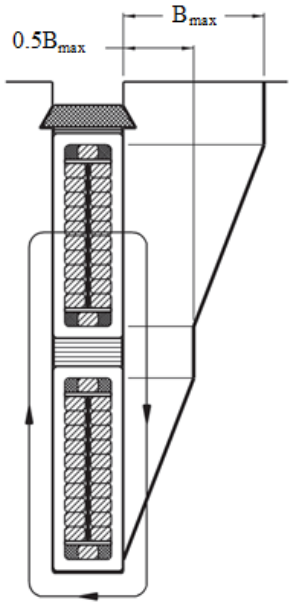

Figure 2.11: Magnetic field distribution accross a slot, adapted from [16].

The electrical insulation between the stator core and windings, as well as between individual windings, is provided by insulating materials wrapped around the coils. An example of a winding with a complete insulation system is previously shown in Figure 2.9.

2.2.2 Rotor Assembly

As previously discussed, hydro generators are predominantly designed with a salient–pole rotor geometry. Fundamentally, the rotor assembly consists of the spider rim, ventilation fan, rotor core, poles, field windings, and damper windings. The spider rim (or rotor spider) transfers shaft rotation and torque to the rotor. While rotor spiders are typically produced using casting methods, both cast and fabricated versions exist [12]. Additionally, the spider rim contributes to the mechanical rigidity of the rotor. The ventilation fan aids in cooling the generator by circulating air, and is generally

installed at both the top and bottom of the rotor.

The rotor core and poles are constructed from laminated steel, designed to create and guide the rotating magnetic field. From an electromagnetic perspective, the purpose of lamination is to reduce core losses, particularly eddy current losses. Ideally, eddy current losses are minimized because the rotor rotates synchronously with the magnetic field, thus experiencing a constant (DC) magnetic field. However, in practice, due to variations in the airgap caused by the slotted stator and the salient poles, harmonics that rotate at different speeds arise, leading to eddy current losses.

The lamination thickness of rotor steel is generally greater than that of stator steel, typically ranging from 1 to 1.5 mm. This increased thickness is necessary to withstand the significant mechanical stresses generated by rotor rotation, thereby ensuring the rotor's structural integrity [12].

The rotor pole is designed such that the airgap, and consequently the reluctance, varies with its position. This variation in reluctance creates a reluctance torque due to the rotor geometry. Optimizing the rotor shape can help minimize time and spatial harmonics, thereby enhancing machine performance. For instance, a secondary radius can be incorporated into the outer perimeter of the pole. Each pole consists of magnetic steel, field windings, and damper windings, with a representative pole geometry illustrated in Figure 2.12. As previously noted, due to the mechanical stresses acting on the rotor poles, such as centrifugal forces, their laminations are thicker than those of the stator.

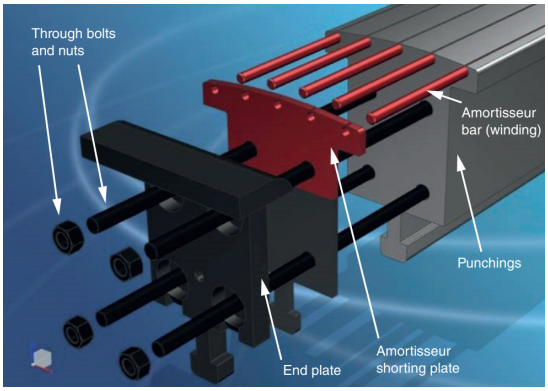

Figure 2.12: Rotor pole assembly, adapted from [12].

The field windings generate the magnetic field, while the damper windings mitigate higher–order harmonics and enhance stability. Compared to stator windings, the field windings are relatively simple, as they are excited by DC current, which ideally prevents the occurrence of skin effects or circulating currents. However, maintaining mechanical rigidity during rotation presents a significant challenge [12]. The field windings are functioning like an electromagnet. In simple terms, the current–carrying windings wound around the magnetic material create a magnetic field.

In addition to the field windings, rotor poles also contain damper bars (see Figure 2.12). Damper windings are simply copper bars that placed into pole tips and short–circuited at both ends. In synchronous motors, these damper windings enable self–starting capability, while in hydro generators, they serve to enhance the generator's stability. Specifically, when there is a sudden change in load, the power angle shifts accordingly. Damper windings help prevent the machine from oscillating around the new power angle and losing synchronism. The concept behind damper bars in hydro generators is damping the counter–rotating fields [10, 12, 20, 21].

Under steady–state conditions, damper bars help reduce losses at the pole face, which primarily result from the slotted geometry of the stator [22]. The stator's slotted configuration distorts the magnetic field across the airgap, introducing harmonics known as slot harmonics. Since these harmonics occur at frequencies different from the fundamental frequency, they induce currents in the damper bars.

CHAPTER 3

DESCRIPTION AND ANALYTICAL MODELLING OF EXISTING GENERATOR

The generator under inspection and refurbishment is located in Sarıyar, Ankara, Turkey. Sarıyar Hydroelectric Power Plant (HPP) consists of four units (4×40 MW), and operated by government company, The Electricity Generation Corporation (EÜAŞ). Two of the units were installed by AEG, while the remaining two were installed by Westinghouse. Although all four units share identical power and voltage ratings, the AEG units are constructed using Roebel bars, whereas the Westinghouse generators are wound with diamond-type coils. Figure 3.1 illustrates two of the generators.

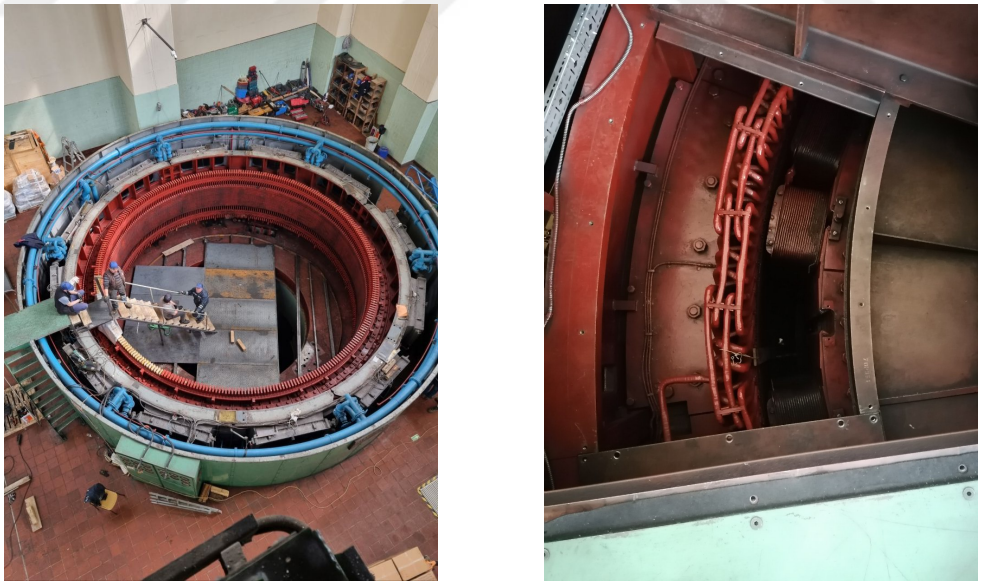

(a) AEG (b) Westinghouse

Figure 3.1: Sarıyar Hydro Power Plant Units–I and III: Generator installed by AEG (a) and Westinghouse (b).

This chapter offers an in–depth examination of the generator under study, specifically the Sarıyar Hasan Polatkan Hydro Power Plant Unit–3, which was originally designed by Westinghouse Electric Co. It addresses the inherent complexities involved in modeling large, existing hydro generators, highlighting specific challenges related to the aging infrastructure and incomplete design documentation. Additionally, the chapter details the analytical modeling approach applied to the generator, providing a comprehensive comparison with data from the commissioning tests. This analytical model will serve as a foundational tool for generator sizing and performance evaluation in subsequent optimization studies.

3.1 Generator Under Concern: Sarıyar Hydro Power Plant Unit III

The installation of the generators began in 1956, and they have been in operation for over 60 years. The generator under consideration was designed by Westinghouse Electric Corporation, with its nameplate shown in Figure 3.2. The characteristics of the generator are provided in Table 3.1.

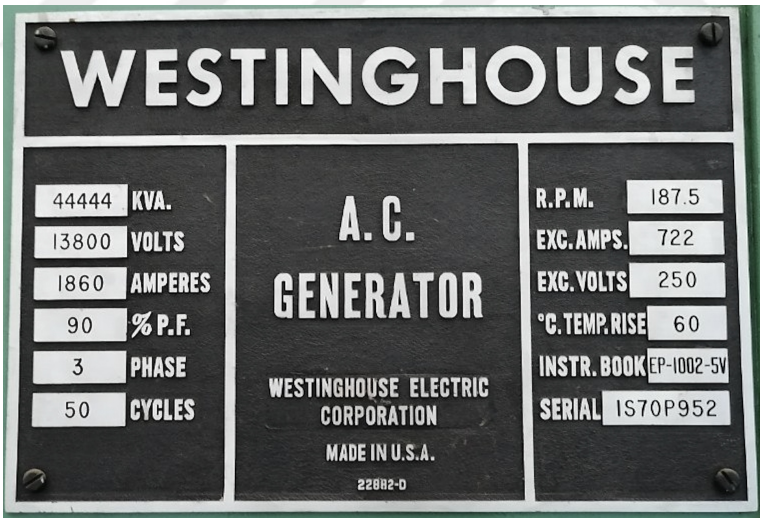

Figure 3.2: Nameplate of the Sarıyar HPP Unit III

The generator under concern is a three–phase, star–connected, 50 Hz salient–pole synchronous machine with a rated power of 44.444 MVA, a rated power factor of 0.9, and a rated voltage of 13.8 kV. It has 32 poles, resulting in a rotor speed of 187.5

Westinghouse Generator Characteristics	
Rated Power	44.444 (MVA)
Rated Voltage	13.8 (kV)
Rated Speed	187.5 (rpm)
Rated Phase Current	1860 (A)
Rated Power Factor	0.9
Rated Field Current	722 (A)
Number of Slots	240
Number of Poles	32
Turns per Winding	5
Parallel Circuits	4
Strands per Winding	50
Number of Field Turns	41

Table 3.1: Characteristics of generator under concern.

rpm. The machine contains 240 slots and is wound as a three–phase, double–layer, star–connected system with a grounded neutral. The windings are lap windings with five turns and four parallel circuits, yielding 100 turns per phase. Each turn consists of 10 strands, resulting in 50 strands per winding.

Nowadays, the Westinghouse generator typically operates at a unity power factor with an output of 40 MW. On average, it runs for 8 hours per day, resulting in a daily generation of 320 MWh per generator. Annually, a single Westinghouse generator produces approximately 119 GWh of electrical energy [23]. In 2002, one of the diamond coils failed due to a strand–to–strand short circuit. The maintenance operations lasted for 21 days and incurred a cost of approximately 3.47 M€, including the cost of lost energy during the outage. The extended duration of the maintenance was due to the nature of the diamond coils, as previously discussed, which require the disassembly of multiple coils, significantly increasing the fault–clearing time.

The stator core material of the generator in question is M400-50A low–loss electrical steel, with a thickness of 0.5 mm. This material typically exhibits core losses of 4 W/kg at a magnetic flux density of 1.5 T. However, current industry practice favors

using the highest–quality off–the–shelf steel, as the initial cost difference is quickly recovered through reduced operational losses [14, 24]. The stator is radially divided into two sections and stacked with 16 ventilation ducts arranged axially. All ventilation ducts have a uniform thickness of 9 mm. To minimize eddy current losses at the machine's ends, the axial ends of the stator and the fingers are cut, as shown in Figure 3.3.

Figure 3.3: Fingers of the Westinghouse generator.

The production documents indicate that the main insulation thickness of the generator's diamond windings is 6.5 mm, while the turn insulation thickness is 3 mm. The strands are arranged such that half are uninsulated and the remaining strands are insulated, as shown in Figure 3.4. However, the windings consist of five turns in practice, as illustrated in Figure 3.4. In older generators, such discrepancies in documentation are not uncommon [25]. As a result, the modelling of older machines requires additional review and careful examination.

The steel grade and thickness of the rotor laminations in the Westinghouse generator are unknown, as no production documents regarding the rotor are available. Additionally, there are inconsistencies in the available information concerning the airgap

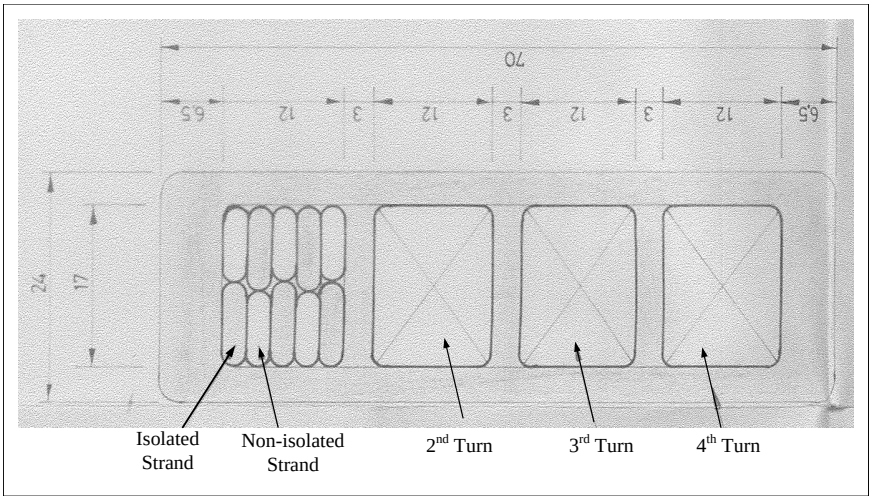

(a) Winding cross–section of Westinghouse generator, adapted from the production documents.

(b) Existing winding in operation.

Figure 3.4: Comparison of winding configurations for Sarıyar Hydro Power Plant Unit III: (a) design from production documents and (b) current configuration in operation.

and rotor diameter. While the production documents indicate an airgap of 12.7 mm (0.5 inches), on–site measurements show an airgap of 18 mm. Another discrepancy

pertains to the pole design. There are no documents providing details about the pole, but on–site visual inspections reveal the absence of a secondary pole arc and the presence of five damper bars per pole. However, no information is available regarding the dimensions of the damper bars. The pole dimensions, including body width, body height, shoe width, and shoe height, (refer to Figure 3.5) were measured on-site by disassembling one of the poles, as illustrated in Figure 3.1(b).

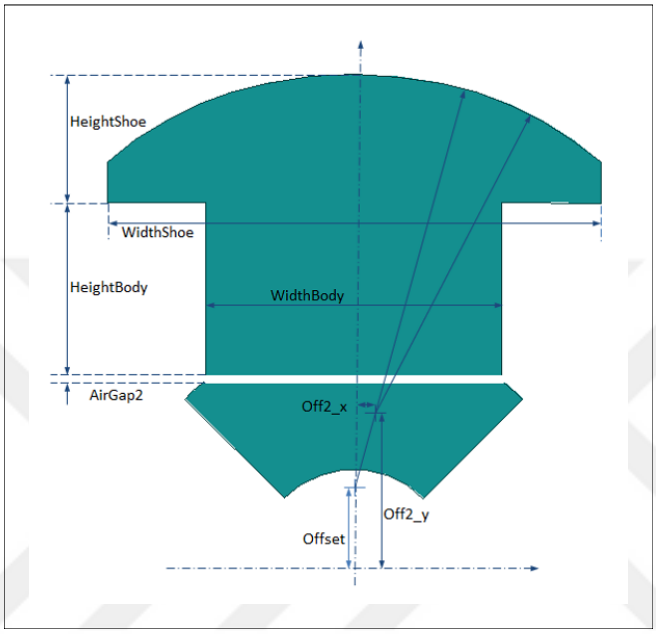

Figure 3.5: Dimensioning of the pole, adapted from [26].

A further inconsistency concerns the rotor height. According to the machine drawings, the rotor height is 900 mm, while the stator height is 925 mm.

On–site inspections confirm that the axial lengths of both the rotor and stator are identical, measuring 925 mm.

The outer diameter, however, remains unclear due to contradictory information in the production documents. Two different outer diameters are reported: 6857.6 mm and 6868 mm. Although the difference is small, accurately modelling the generator is essential for future parametric optimizations. This discrepancy results in an overdefined lamination drawing. In other words, the lamination cannot be accurately drafted due to these inconsistencies. Given that most components of the generator were designed using imperial units, it is likely that the correct outer diameter is 6858 mm

(270 inches).

The dimensions of the machine are provided in Table 3.2.

Westinghouse Generator Dimensions	
Rotor Diameter	6161.6 mm
Airgap	18 mm
Stator Inner Diameter	6197.6 mm (244")
Stator Outer Diameter	6858 mm (270")
Slot Width	25.4 mm (1")
Slot Height	152 mm (≈6")
Axial Length	925 mm
Number of Ventilation Ducts	16
Height of Ventilation Duct	9 mm (≈0.35")
Pole Body Width	343 mm (13.5")
Pole Body Height	252 mm (≈10")
Pole Shoe Width	406 mm (≈16")
Pole Shoe Height	45 mm (≈1.75")

Table 3.2: Dimensions of generator under concern.

Due to the generator's age, exceeding 60 years, various discrepancies in the available documentation exist. These inconsistencies contribute to the increased complexity of the modelling process. Therefore, several key metrics must be compared to validate the model.

The first step is to ensure that the open–circuit curve of the model closely matches that of the existing generator. Following this, the short–circuit (SC) curves should also be compared. If both tests are validated, the machine's characteristic impedances and time constants should be reviewed for further accuracy [25].

While these calculations can be easily performed analytically by neglecting magnetic saturation, saturation is the primary source of discrepancies in the results. Additionally, analytically determining the time constants is a highly complex and time–consuming process. Consequently, finite element analysis (FEA) is required for ac-

curate model validation. Initially, analytical calculations are conducted, after which a finite element (FE) model is developed using ANSYS Maxwell software [26].

Another challenge is that conducting open–circuit tests on–site is relatively straightforward and low-risk, whereas short–circuit testing may pose a risk of damage [27]. As a result, the operating company does not permit short–circuit tests on the generator. Therefore, the open–circuit curve is validated using data from on–site testing and manufacturing records, while the short–circuit curve is validated solely against commissioning data.

3.2 Analytical Modelling of Existing Generator

Analytically modelling and analyzing an electric machine with a non–linear core material may not yield highly accurate results. However, it offers a fast and computationally efficient method to obtain reasonably accurate outcomes. Moreover, it allows for observing trends in results relative to specific parameters without significant computational effort. Therefore, it is advantageous to begin with an analytical model.

The first step is to calculate the winding parameters. This process begins by determining the slot and pole pitches. As the term suggests, pitch refers to the distance between adjacent slots or poles. It can be expressed either as an angular measurement or a linear distance. The slot pitch, in terms of angle, can be calculated as follows:

$$\alpha_s = \frac{2\pi}{Q} \approx 0.026 \text{ rad} \tag{3.1}$$

or as a distance

$$\tau_s = \frac{\pi \times D_g}{Q} \approx 80.9 \text{ mm} \tag{3.2}$$

where τ_s is the slot pitch, D_g is the airgap diameter of the machine, and Q is the number of slots. Pole pitch as an angle can be calculated as follows:

$$\alpha_p = \frac{2\pi}{p} \approx 0.20 \text{ rad} \tag{3.3}$$

or as a distance

$$\tau_p = \frac{\pi \times D_g}{p} \approx 606.7 \text{ mm} \tag{3.4}$$

where p is the number of poles. Another parameter related to the winding configuration is the number of slots per pole per phase.

$$q = \frac{Q}{mp} = 2\frac{1}{2} \tag{3.5}$$

where q is the slots per pole per phase, and m is the number of phases.

Machines with non–integer values of slots per pole per phase (q) are referred to as fractional slot machines. The majority of hydrogenerators are designed with fractional slots to minimize cogging torque by reducing zig–zag leakage reactance and space harmonics [6].

Subsequently, the coil pitch (y) must be determined to calculate the winding factors for both the fundamental component and harmonics. Coil pitch refers to the number of slots that a single coil spans. Once the coil, slot, and pole pitches, as well as the number of slots per pole per phase, are known, the winding factors can be computed.

Hydro generators typically employ short–pitched, distributed, and double–layer windings. The term 'distributed' indicates that the coils are spread across multiple slots rather than being concentrated in a single slot, meaning phase windings are distributed throughout the slots. When the coil span equals the pole pitch, it is referred to as a full–pitch winding. Depending on the coil span's length, the winding can be classified as short–pitch, full–pitch, or long–pitch.

If there is no skew in the generator, two key factors characterize the winding factor: the pitch factor and the distribution factor. The pitch factor is defined as the ratio between the flux of a short–pitch coil and that of a full–pitch coil.

$$k_{p,n} = \sin\left(n\frac{y}{2}\right) \tag{3.6}$$

where n is the order of harmonic, and y is the coil pitch in radians.

The distribution factor is defined as the ratio of the vector sum of the voltage phasors to the algebraic sum of the voltage phasors. This factor is always less than 1, except in the case where $q = 1$ [10].

$$k_{d,n} = \frac{\sin\left(nq\frac{\alpha_s}{2}\right)}{q\sin\left(n\frac{\alpha_s}{2}\right)} \tag{3.7}$$

The winding factor illustrates the magnitude of the coil voltage in comparison to that of a full–pitch and concentrated winding. It is expressed as follows:

$$k_{w,n} = k_{p,n} \times k_{d,n} \tag{3.8}$$

Calculated winding factors are presented in Figure 3.6.

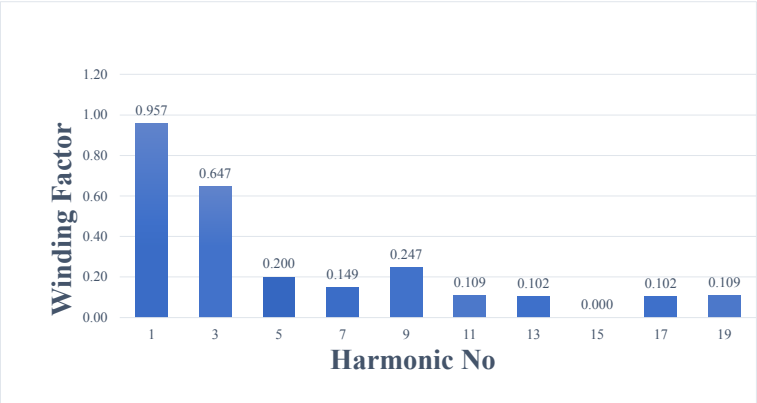

Figure 3.6: Winding factors of existing generator.

Once the winding parameters have been identified, the electrical and magnetic loadings can be calculated. The output power of the machine is directly related to its electrical and magnetic loadings; therefore, understanding the machine's loadability provides essential information regarding its rated power.

Electrical loading is also associated with copper losses, which in turn affects the thermal loadability of the machine. It can be calculated as follows:

$$\bar{A} = \frac{mN_{ph}I_{ph}}{\pi D_g} \approx 57.32\ \mathrm{kA/m} \tag{3.9}$$

where I_a is the rated phase current in RMS, and N_{ph} is the number of turns per phase.

$$N_{ph} = \frac{z_Q}{2pq} = 100 \tag{3.10}$$

where z_Q is number of conductors per slot. Alternatively, electrical loading can be calculated as

$$\bar{A} = \frac{JA_{cu,s}}{\tau_s} \tag{3.11}$$

where J is the linear current density of windings, and $A_{cu,s}$ is the total copper area inside a slot.

Magnetic loading is directly associated with core losses and is defined as the average magnetic flux density in the airgap. It is important to note that the airgap varies due to the saliency of the rotor poles and the presence of slots in the stator. Consequently, solving the magnetic circuit becomes quite complex, as the flux density decreases at the slot openings.

To determine an effective airgap and simplify analytical calculations, Carter's coefficient is employed [28]. Assuming rotor surface is smooth, and stator remains slotted yield a magnetic field distribution among a slot as in the Figure 3.7. In the figure, $B(\alpha)$ is magnetic flux density distribution accross a slot pitch as a function of α, where b_1 is the actual slot opening, and b_e is the effective slot opening. Then, b_e is

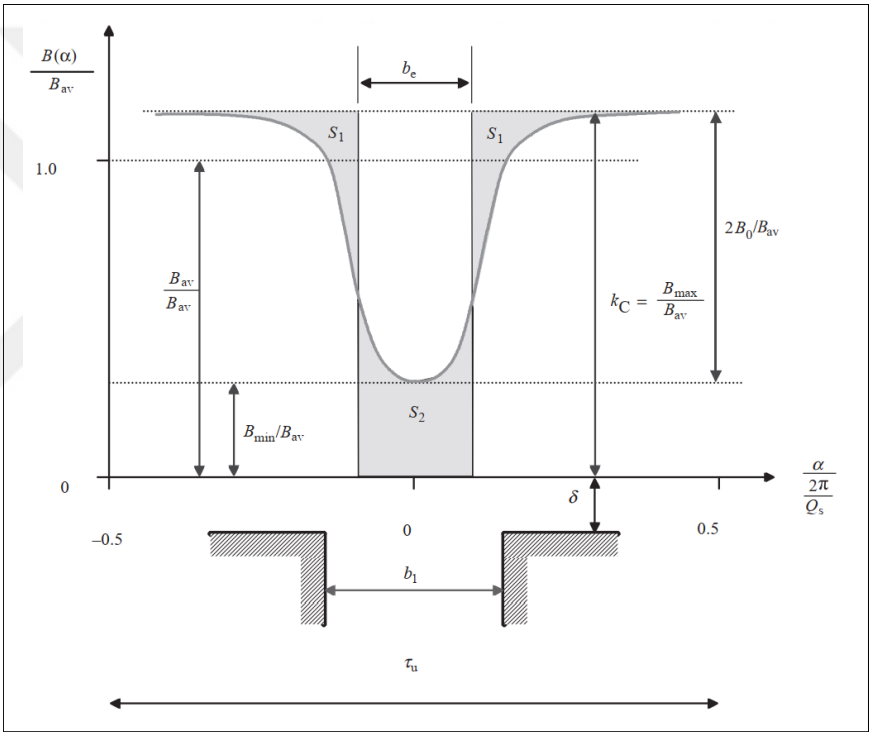

Figure 3.7: Flux and flux density distribution among a slot when rotor surface is assumed to be smooth, adapted from [10].

defined as

$$b_e = \kappa b_1 \tag{3.12}$$

where

$$\kappa = \frac{b_1/g}{5 + b_1/g} \tag{3.13}$$

g is being equal to the airgap. Then, Carter's coefficient for stator is defined as follows:

$$k_{Cs} = \frac{\tau_s}{\tau_s - \kappa b_1} = 1.07 \tag{3.14}$$

Carter's coefficient for the rotor is calculated in a similar manner. However, instead of the slot opening, the distance between adjacent poles is utilized in the calculations, while the remaining aspects remain unchanged. Ultimately, the total Carter's coefficient is expressed as follows:

$$k_C = k_{Cs} k_{Cr} = 1.4 \tag{3.15}$$

k_{Cr} is the Carter's coefficient for rotor. Carter's coefficient also defined as the ratio of the peak flux density to the average flux density in the airgap.

$$k_C = \frac{\hat{B}_g}{B_{g,avg}} \tag{3.16}$$

Once the total Carter's coefficient has been calculated, the effective air gap (g') can then be determined using the following expression.

$$g' = k_C \times g = 25.12 \text{ mm} \tag{3.17}$$

Other than stator slots and rotor saliency, there also exist ventilation ducts in the stator. The same methodology is applied for calculating the effective axial length. In other words, to calculate κ and Carter's coefficient, the slot opening term (b_1) is replaced with duct height (b_v), and the pitch term (τ) is replaced with duct pitch. Then, the effective duct height (b_{ve}) is calculated. Finally, the effective axial length becomes

$$L' = L - n_v b_{ve} + 2g \approx 913.3 \text{ mm} \tag{3.18}$$

where L' is the effective axial length, L is the actual axial length, and n_v is the number of ventilation ducts. In this equation, the term $2g$ accounts for the stray flux at the core ends. Essentially, it serves as an approximation, assuming that stray fluxes extend approximately a distance of g at each end of the core [10].

After finding the effective airgap and axial length, Ampere's Circuital Law can be applied to find the average magnetic flux density in the airgap.

$$\hat{\phi_p} = \frac{N_f I_f}{R_g} = 0.37 \text{ Wb} \tag{3.19}$$

where $\hat{\phi_p}$ is the flux per pole, N_f is the number of field turns, and I_f is the field current. R_g is the reluctance of the airgap and calculated as

$$R_g = \frac{g'}{\mu_0 L' \tau_p} \tag{3.20}$$

Note that in Equation 3.19, it is assumed that there is no magnetic voltage drop across the magnetic core, as the core material possesses a significantly higher permeability than air, typically on the order of several thousand.

Finding out the peak value of the B field from flux per pole gives

$$\hat{B_g} = \frac{\mu_0 N_f I_f}{g'} = 1.23 \text{ T} \tag{3.21}$$

Finally, magnetic loading can be calculated from Equation 3.16 as following.

$$B_{g,av} = \frac{\mu_0 N_f I_f}{k_C g'} = 0.9 \text{ T} \tag{3.22}$$

By applying Faraday's Law of Induction exclusively to the fundamental component of the flux and assuming it to be a sinusoid with a frequency of f, one obtains

$$\begin{aligned} e_{rms} = 4.44 k_w f N_{ph} \hat{\phi_p} &= 7860 \text{ V (phase)} \\ &= 13760 \text{ V (line} - \text{to} - \text{line)} \end{aligned} \tag{3.23}$$

Subsequently, the flux densities at the teeth and yoke can be calculated using the flux per pole ($\hat{\phi_p}$). It is important to note that $\hat{\phi_p}$ passes through the number of teeth per pole, with half of it traversing the yoke. Therefore, the flux densities at the teeth and yoke can be expressed as

$$B_t = \frac{\hat{\phi_p} p}{Q b_t L'} \approx 1.80 \text{ T} \tag{3.24}$$

where b_t is width of tooth.

$$B_y = \frac{\hat{\phi_p}}{2 t_y L'} \approx 1.15 \text{ T} \tag{3.25}$$

where t_y is the radial thickness of yoke.

Upon determining the flux densities at the teeth and yoke, the core losses can be calculated using the Steinmetz equation and the Bertotti model [29, 30]. The volumetric core loss density over one cycle can be expressed as

$$p_{core} = k_{hys} f |B|^{\alpha} + k_{edd} f^2 |B|^2 + k_{exc} f^{1.5} |B|^{1.5} \tag{3.26}$$

In this equation, k_{hys}, k_{edd}, and k_{exc} represent the coefficients for hysteresis, eddy current, and excess losses, respectively, while α denotes a material–dependent coefficient. By integrating the aforementioned equation over the volume of the core and time–averaging the results, the core losses (P_{core}) of the machine can be determined.

To assess the efficiency, copper losses can be easily calculated with the well known formula

$$P_{cu} = mI_{ph}^2 R_{ph} = 130\,\text{kW at } 75^\circ C \tag{3.27}$$

Then, the efficiency of the generator is

$$\eta = \frac{P_{out}}{P_{out} + \sum P_{loss}} \approx 97.9\% \tag{3.28}$$

3.3 Analytical Calculation of Characteristic Machine Reactances and Time Constants

For the initial iterations, such an analytical model suffices. However, subsequent iterations will necessitate calculations of machine characteristic parameters. For instance, to construct the machine phasor diagram, it is essential to determine the direct and quadrature axis reactances. Additionally, for transient performance analyses, knowledge of transient and subtransient reactances, along with their corresponding time constants, is required.

Calculating these parameters necessitates comprehensive knowledge of the machine's geometry, which includes the configurations of the poles, dampers, and windings [31]. Nevertheless, as previously mentioned, obtaining this information for an aged existing generator may prove challenging. Consequently, analytical calculations of the machine's reactances and time constants may yield substantial discrepancies from the actual values.

In the analytical model, the geometry of the pole and dampers is approximated based on extracted information from photographs and on–site measurements, allowing for the calculation of reactances and time constants. Kilgore's approach begins with the computation of a reactance factor [31]. The reactance factor is defined as the percent

reactance for a unit specific permeance, which represents the effective flux per pole per unit core length generated by unit ampere–turns per pole.

The reactance factor is calculated as follows:

$$X = \frac{I_{ph}}{E_{ph}} f L m p \left(q \frac{z_Q}{a} k_p k_d \right)^2 10^{-8} \tag{3.29}$$

where E_{ph} represents the rated phase voltage and a denotes the number of parallel branches in the armature circuit. The specific permeances are then calculated to evaluate the machine's reactances. The direct–axis synchronous reactance (X_d) and quadrature–axis synchronous reactance (X_q) significantly influence the steady–state performance of the machine. These reactances are composed of various reactance components. Mathematically,

$$X_d = X_{ad} + x_l \tag{3.30a}$$

$$X_q = X_{aq} + x_l \tag{3.30b}$$

where X_{ad} and X_{aq} represent the direct and quadrature–axis armature reactances, respectively. The term x_l denotes the armature leakage reactance, which is calculated as follows:

$$x_l = X(\lambda_s + \lambda_e) \tag{3.31}$$

In this equation, λ_s represents the specific permeance for slot leakage, and is calculated as follows:

$$\lambda_s = C_x \frac{20}{mq} \left(\frac{h_2}{b_1} + \frac{h_1}{3b_1} \right) \tag{3.32}$$

Here, C_x denotes the slot leakage factor, h_1 is the depth of conductors in the stator slot, and h_2 represents the depth of the stator slot until the windings, as illustrated in Figure 3.8. C_x is calculated as

$$C_x = \frac{\frac{3y}{mq} + 1}{4} \tag{3.33}$$

λ_e is the specific permeance of the end winding, and it is calculated as follows:

$$\lambda_e = \frac{4}{L}(l_{e1} + 2l_{e2}) \tag{3.34}$$

l_{e1} and l_{e2} are parameters related to the dimensions of the end winding, as shown in Figure 3.8.

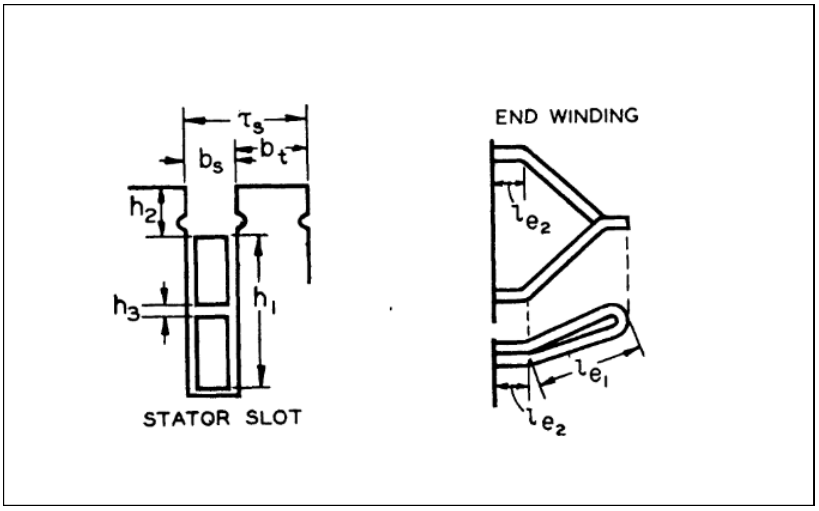

Figure 3.8: Geometric variables related to windings used in reactance calculations, adapted from [31].

X_{ad} is calculated as follows:

$$X_{ad} = \frac{4}{\pi} X C_m \lambda_a \tag{3.35}$$

where C_m is the demagnetizing factor, and for majority of the hydro generators, it is equal to 0.88 [32]. It is experimentally determined as in Figure 3.9. λ_a is the airgap specific permeance and calculated as follows:

$$\lambda_a = 6.38 \frac{D_i}{pg'} \tag{3.36}$$

where D_i is the inner diameter of the stator. Subsequently, X_{aq} is calculated as

$$X_{aq} = X \lambda_a (\alpha_p - \sin(\alpha_p \pi)/\pi) \tag{3.37}$$

where α_p is the pole embrace, and it is equal to ratio of shoe width to the pole pitch.

After determining the steady–state reactances, it is essential to calculate the transient reactances to assess the transient performance of the machine. The direct axis transient reactance (X'_d) can be calculated as follows:

$$X'_d = x'_F + x_l \tag{3.38}$$

where x'_F is the effective field leakage reactance, and calculated as

$$x'_F = X_{ad} \left(1 - \frac{1}{C_m \left[\frac{\pi^2}{8} + \frac{\lambda_{Fs} + \lambda_{Fe}}{\lambda_a} \right]} \right) \tag{3.39}$$

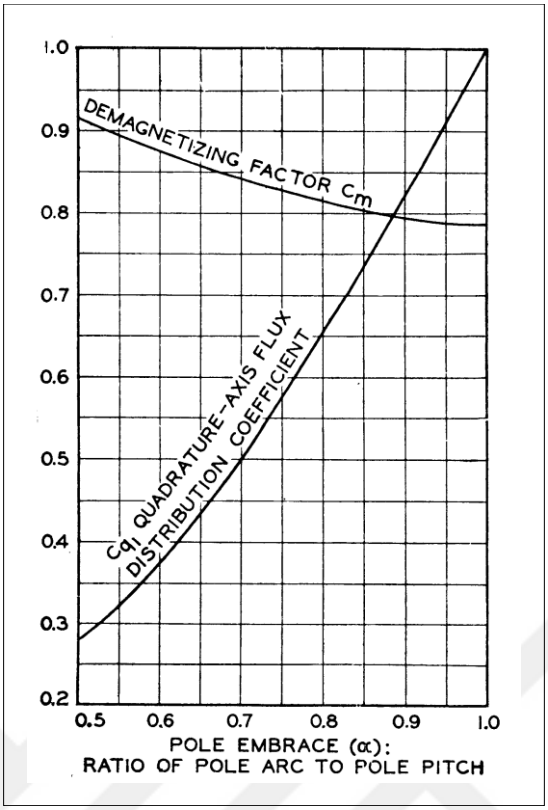

Figure 3.9: Emprically determined demagnetizing factor with respect to ratio of pole embrace to pole pitch.

where λ_{Fs} and λ_{Fe} are the specific permeances of pole side leakage, and pole end leakage, respectively. λ_{Fs} and λ_{Fe} are calculated as follows, and geometrical variables related to equations are presented in Figure 3.10.

$$\lambda_{Fs} = 4.25 \left[\frac{3\left(h_h + g - 0.055\tau_p\right)}{\tau_p - b_h} + \frac{h_{f1} + 3h_{f2} + 0.1\tau_p\left(1 - \frac{10}{p}\right)}{\left(\frac{\pi}{p}\left(D_r - 2h_h - 0.4h_{f1} - b_p\right)\right)} \right] \tag{3.40}$$

$$\lambda_{Fe} = 3.19 \left[\frac{4\left(l_h - l\right) + 2h_{f1} + 0.5b_p}{L} \right] \tag{3.41}$$

Once the transient direct axis reactance is determined, the subtransient reactance must be calculated. The subtransient reactances of the machine can be obtained as follows:

$$X''_d = x_l + X'_{Dd} \tag{3.42a}$$

$$X''_q = x_l + X'_{Dq} \tag{3.42b}$$

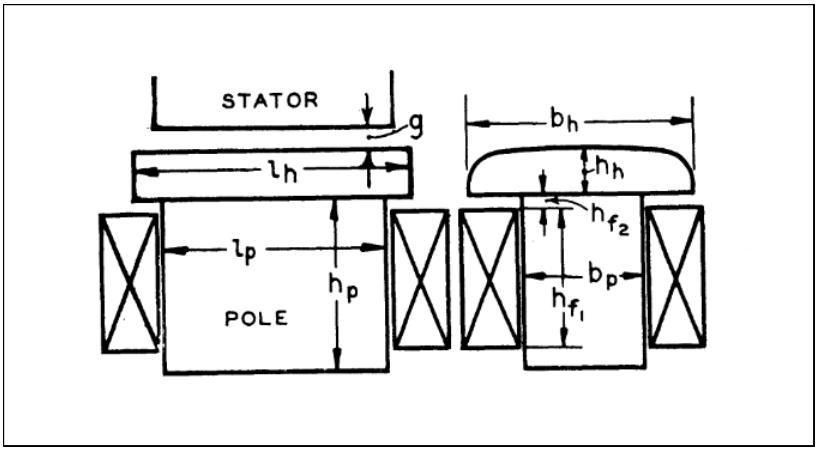

Figure 3.10: Geometric variables related to field leakage reactance, adapted from [31].

where X''_d and X''_q are direct, and quadrature axis subtransient reactances, respectively. For machines without damper windings, $X''_q = X_q$ [31]. Moreover, Sherwin and Wright empirically showed that $X''_q \approx X''_d \approx X_2$, where X_2 is negative sequence reactance [33]. X'_{Dd} is direct axis subtransient armature reactance, and calculated as

$$X'_{Dd} = X\lambda_{Dd} \tag{3.43}$$

where λ_{Dd} is specific permeance of subtransient d–axis reactance, and equal to

$$\lambda_{Dd} = \left[\cos\left(\frac{(n_b - 1)\,\tau_b\pi}{2\tau_p}\right)\right]\left[\frac{(\lambda_b + \lambda_{pt})\,\lambda_F}{\lambda_b + \lambda_{pt} + \lambda_F}\right] \tag{3.44}$$

where n_b is the number of damper bars per pole, τ_b is the pitch of damper bars, and λ_F is the specific permeance of effective pole leakage which is equal to $\lambda_{Fe} + \lambda_{Fs}$. λ_b is the specific permeance of the end damper bar and calculated like specific permeance of slot leakage (λ_s). λ_{pt} is the specific permeance of the airgap over pole shoe, and calculated as follows:

$$\lambda_{pt} = 6.38\left[\frac{b_h - \tau_b\,(n_b - 1)}{3g'}\right] \tag{3.45}$$

Quadrature axis subtransient armature reactance (X'_{Dq}) is calculated as follows:

$$X'_{Dq} = X\lambda_{Dq} \tag{3.46}$$

where λ_{Dq} is specific permeance of quadrature axis subtransient reactance, and calculated as

$$\lambda_{Dq} = \frac{20\tau_b}{\tau_r}\left[0.5 + \frac{h_{b1}}{3b_{b1}}\frac{h_{b2}}{b_{b2}} + \frac{g}{\tau_b}\right] \tag{3.47}$$

where h_{b1}, h_{b2}, b_{b1}, and b_{b2} are variables defining the damper geometry, and defined as a similar way to that of stator slots can be seen in Figure 3.8.

Negative sequence reactance (X_2) is determined as the average of the direct and quadrature axis subtransient reactances [31], i.e.,

$$X_2 = \frac{X'_d + X''_d}{2} \tag{3.48}$$

Zero sequence reactance (X_0) can be calculated as follows:

$$X_0 = X\left(\lambda_{i0} + \lambda_{B0} + 0.2\lambda_e\right) \tag{3.49}$$

where λ_{i0} is the specific permeance of slot and tooth tip leakage reactance, and λ_{B0} is the specific permeance of belt leakage reactance. Specific permeance of slot and tooth tip leakage reactance is calculated as

$$\lambda_{i0} = \left[\lambda_i \frac{k_{x0}}{k_x} + \left(\frac{20}{mqk_p^2k_d^2}\right)\left(\frac{h_1 + 2h_3}{12b_1}\right)\right] \tag{3.50}$$

In this equation, k_{x0} and k_x are reduction factors applied to the reactances of zero and positive/negative sequences, respectively. These values are selected based on Figure 3.11, as outlined in [31]. k_{x0} represents the reduction factor for zero sequence reactance, while k_x is used for both positive and negative sequence reactances in the figure.

Furthermore, the specific permeance of belt leakage reactance is approximated by reducing the direct–axis damper leakage specific permeance (λ_{Dd}) by the ratio $\frac{k_{x0}}{k_x}$, as expressed mathematically:

$$\lambda_{B0} = \frac{k_x 0}{k_x}\lambda_{Dd} \tag{3.51}$$

Once the characteristic reactances of the machine are determined, the open–circuit transient, and direct–axis transient time constants can be computed. However, calculating the direct–axis subtransient time constant is not straightforward and is typically obtained empirically through a three-phase sudden short circuit test [27, 33]. As suggested by Sherwin and Wright, and supported by the IEEE-115 standard, the subtransient time constant typically ranges between half and several cycles (10 ms to 40 ms) [27, 33], for salient–pole synchronous generators with damper windings. The

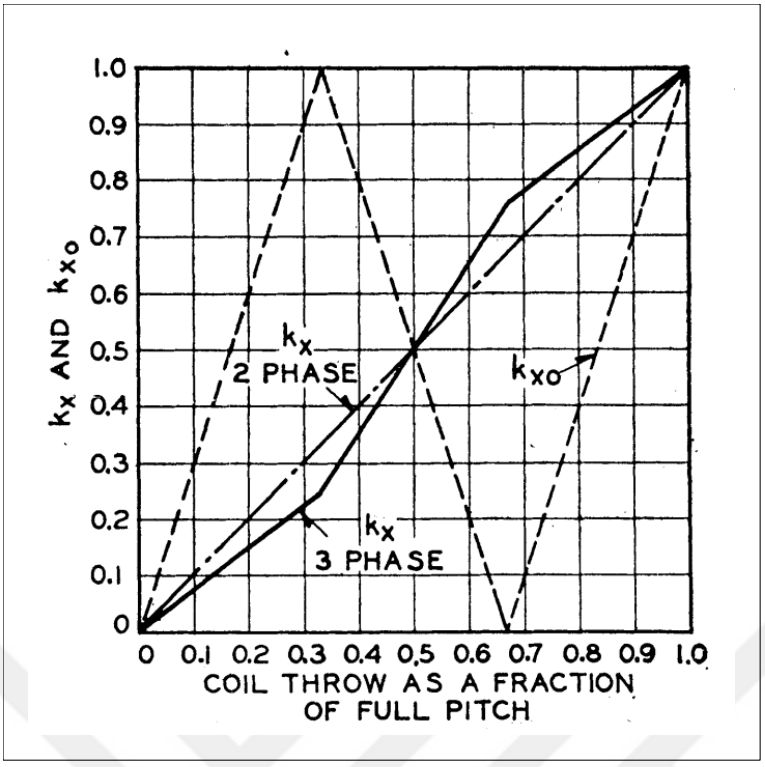

Figure 3.11: Reduction ratios for zero, positive, and negative sequence reactances. The figure is adapted from [31].

open–circuit transient time constant (T'_{do}), on the other hand, corresponds to the time constant of the field circuit and is mathematically expressed as [31]:

$$T'_{do} = \frac{L_f}{R_f} = 2.63 \text{ sec} \tag{3.52}$$

where L_f is inductance of field circuit, and R_f is resistance of field circuit. Finally, direct–axis transient time constant (T'_d) can be calculated as

$$T'_d = T'_{do}\frac{X'_d}{X_d} \approx 0.68 \text{ sec} \tag{3.53}$$

Analytically extracting the open–circuit curve is complex due to the saturation in the core material. However, the airgap line (the open-circuit curve without considering saturation) can be derived and compared with both finite element analysis (FEA) and test results. The airgap lines from the analytical model, FEA, and test results are presented in the preceding subsection.

Additionally, the three–phase sudden short circuit test can be applied analytically using the formulas provided in the IEEE Guide for Test Procedures for Synchronous

Machines [27]:

$$I_{sc} = \sqrt{2}E_{ll}\left[\frac{1}{X_d} + \left(\frac{1}{X'_d} - \frac{1}{X_d}\right)e^{\frac{-t}{T'_d}} + \left(\frac{1}{X''_d} - \frac{1}{X'_d}\right)e^{\frac{-t}{T''_d}}\right] \tag{3.54}$$

where E_{ll} represents the line-to-line rated voltage of the machine. It is important to note that this formula provides the envelope of the phase currents, meaning it represents the maximum values that the phase currents can reach during a sudden short circuit event. This approximation is widely used for assessing the machine's response under fault conditions.

3.4 Results & Discussions

The results obtained from the analytical model and commissioning test are presented in Table 3.3 and Table 3.4. As shown in Table 3.3, copper losses are slightly overestimated, primarily due to uncertainties regarding the end–winding geometry. Conversely, core losses are minimally overestimated, attributed to the lack of precise data on the characteristics of the core material. For the analytical model, M400–50A steel was assumed as the core material.

Regarding machine characteristic reactances, the analytical model calculations fall within a $\pm 10\%$ deviation range compared to commissioning test values. This discrepancy largely arises from incomplete information about the geometry of the rotor, poles, and damper bars. Greater accuracy in the reactance calculations could be achieved by further clarifying these geometrical details.

Table 3.3: Comparison of copper losses (P_{cu}), core losses (P_{core}), and efficiency between commissioning test results and analytical model predictions..

	Commissioning Test Result	**Analytical Modelling**
$P_{cu,s}$ (Stator)	125.5 kW	130 kW
$P_{cu,r}$ (Rotor)	130.2 kW	135.5 kW
P_{cu}	255.7 kW	265.5 kW
P_{core}	220 kW	187.4 kW
Efficiency	97.8%	97.9%

Table 3.4: Comparison of machine characteristic parameters between commissioning test results and analytical model predictions.

	Commissioning Test Result	**Analytical Modelling**
R_a	12.1 mΩ	12.5 mΩ
X_d	0.98 $p.u.$	0.91 $p.u.$
X_q	0.55 $p.u.$	0.45 $p.u.$
X_d'	0.26 $p.u.$	0.23 $p.u.$
X_d"	0.23 $p.u.$	0.22 $p.u.$
X_2	0.25 $p.u.$	0.21 $p.u.$
X_0	0.14 $p.u.$	0.17 $p.u.$

As previously discussed, open-circuit (OC) test serves as effective tool for validating the model. Figure 3.12 presents the OC test results comparing analytical calculations with commissioning data. It is evident that the analytical model accurately represents the linear region of the existing generator. Incorporating saturation effects into the analytical model is complex and time–consuming, as finite element analysis (FEA) will inherently account for saturation in its modeling process.

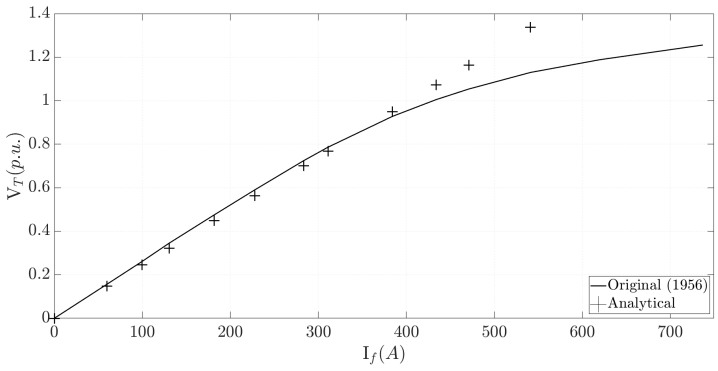

Figure 3.12: Open circuit test comparison of analytical and original machine.

In summary, the analytical model results slightly overestimate copper and core losses due to uncertainties in end–winding geometry and core material assumptions. Reactance calculations are within $\pm 10\%$ of commissioning values, with deviations linked to incomplete geometric data on the rotor and damper bars. Open–circuit tests confirm

that the analytical model accurately represents the generator's linear region, while finite element analysis (FEA) is preferred for modeling saturation due to its complexity.

CHAPTER 4

ANALYTICAL DESIGN AND OPTIMIZATION OF REFURBISHMENT

As previously stated, this study provides a comprehensive methodology and guidance for the refurbishment of hydro generators, including geometry optimization. Additionally, an analytical design approach, based on the analytical model described in the previous section, is employed to develop an initial design. This analytical model serves as the foundation for both the main dimensioning of the machine and the design of Roebel bars, which are essential components of the refurbishment process. Furthermore, the optimization algorithm also builds upon this analytical framework.

This chapter begins by presenting the Roebel bar design algorithm in detail. Subsequently, utilizing the previously introduced analytical model and Roebel bar design guidelines, a candidate machine is designed and its characteristics are analyzed. The chapter then introduces the optimization algorithm, followed by a discussion of its results.

The outcomes from the analytical design approach and the optimization process are not only crucial for identifying optimal design parameters but also serve as key inputs for evaluating the vibration characteristics of the machines in subsequent chapters.

4.1 Design of Roebel Bar

Stator winding copper losses constitute between 15% and 25% of the total machine losses, depending on the specific machine design. In the context of machine upgrading or uprating, minimizing copper losses is a critical design consideration to ensure that the new winding will: maintain an acceptable temperature rise, and enhance

overall machine efficiency at the increased rating [16].

Total copper losses in a hydro generator consist of both DC and AC copper losses. DC copper losses can be calculated straightforwardly using the physical parameters of the winding and the established I^2R formula. However, calculating the additional AC losses is more complex, yet essential, as these losses contribute significantly to temperature rise. Therefore, designing for reduced copper losses necessitates a comprehensive analysis of both DC and AC copper losses.

The calculation of DC copper losses remains relatively straightforward given the known winding geometry.

$$R_{DC} = \rho \frac{MLT \times N_{ph}}{A_{cu}} \qquad \Omega \tag{4.1}$$

where MLT stands for mean length per turn, and ρ is the material resistivity at the operating temperature.

AC losses in a hydro generator consist of three main components: skin effect, circulating currents, and eddy current losses. The skin effect is mitigated by employing stranded windings, which involve constructing the winding from multiple small conductors. By selecting strand dimensions smaller than the skin depth, a nearly uniform current density distribution across the strands can be achieved.

To reduce circulating currents, the primary approach is to transpose the strands so that each occupies all possible positions within the slot along the length of the winding. In multi–turn and diamond–type windings, the inverted–turn approach is used for transposition, whereas single–turn and wave windings employ Roebel bars. The inverted–turn method alternates the order of turns between adjacent slots, ensuring that each turn spans all positions throughout the slot. In contrast, Roebel bars transpose the strands directly, similar to litz wire construction.

Transpositions are commonly implemented at angles of 180°, 360°, 540°, 720°, and so forth. Due to the relatively short axial length of hydro generators, 180° and 360° transpositions are the most feasible. When a 180° transposition is applied within a slot, strands must either be transposed at the connection points or within the end windings, which can increase labor during installation and maintenance. Consequently, 360° transpositions are typically preferred in hydro generators [12, 16]. The Roebel

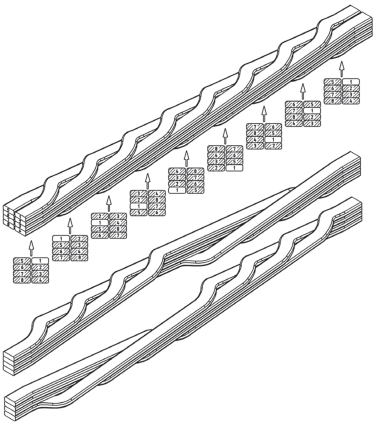

(a)

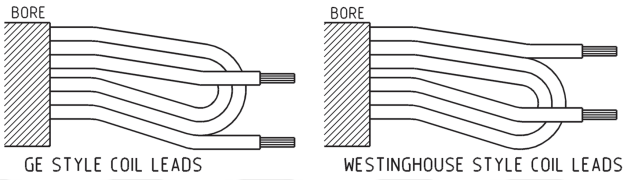

(b)

Figure 4.1: Illustration of Roebel bar (a) and inverted–turn (b), adapted from [16].

transposition and inverted–turn methods are illustrated in Figure 4.1.

Only remaining loss term is the eddy current losses. The eddy current loss in hydro generator windings is caused by the tangential slot leakage fluxes (see Figure 4.2). In more detail, tangential slot leakage fluxes creates a non–homogeneous current distribution inside the strand.

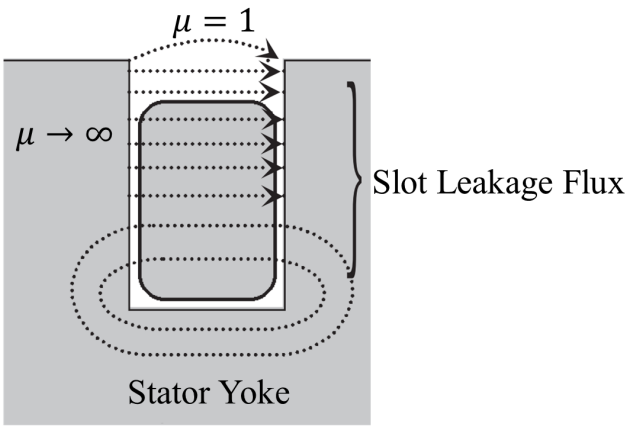

Figure 4.2: Illustration of slot leakage fluxes across a slot, adapted from [10].

Given that the core material possesses a relative permeability thousands of times greater than that of air, it is assumed that the core is infinitely permeable in the representation of slot leakage flux illustrated in Figure 4.2. Additionally, the eddy current distribution corresponding to various strand designs is depicted in Figure 4.3. It is

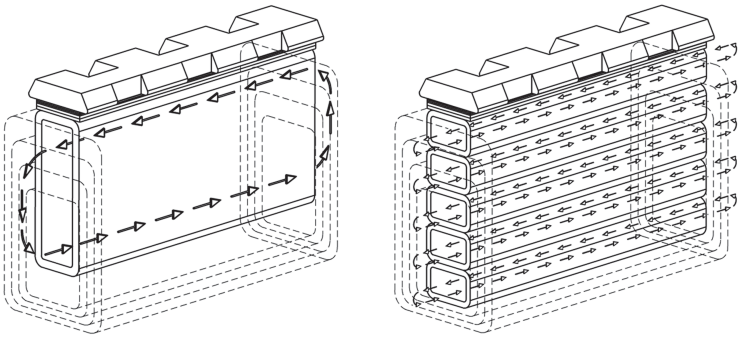

Figure 4.3: Eddy current distribution with respect to strand size, adapted from [16].

evident from Figure 4.3 that by appropriately designing the number and size of the strands, eddy current losses can be minimized.

Copper loss due to eddy currents can be calculated with the formula given below.

$$P_{cu,eddy} = \frac{\pi^2}{6\rho} B_{max}^2 f^2 h^2 V \tag{4.2}$$

In this equation, ρ is the material resistivity at operating temperature, h is the height of the strand, and V is the volume of the strand.

To obtain the AC losses, the slot dimensions, insulation thicknesses, strand dimensions, and rated armature current must be known. Afterwards, the DC copper losses can be easily calculated once the copper geometry is established. On the other hand, the B field distribution inside the slot must be known to obtain the AC losses.

To get the magnetic field distribution across the slot, Ampère's Circuital Law is applied for each strand. The B field distribution inside a slot is represented in Figure 4.4. The calculation of B_{max} presented in Figure 4.4 is as follows.

$$B_{max} = \frac{2\mu_0 I_{ph}}{b_1} \tag{4.3}$$

Combining Equations 4.2 and 4.3, eddy losses can be easily calculated.

This methodology allows for an iterative approach to designing the Roebel bar, rather

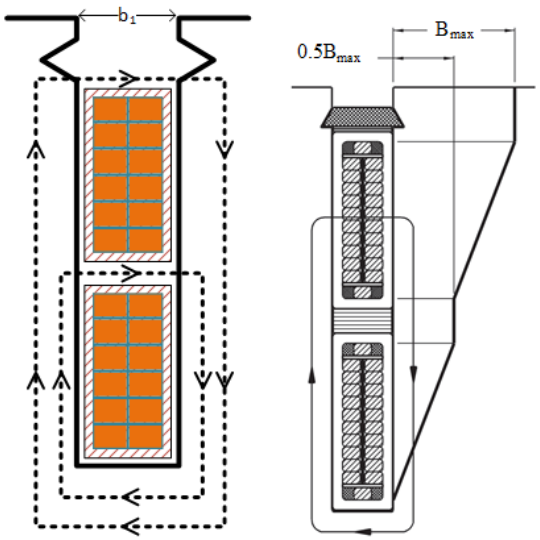

Figure 4.4: B field distribution accross a slot.

than merely analyzing it. Specifically, given the slot dimensions, axial length, and coil pitch, the Roebel bar can be systematically designed through repeated iterations. The flowchart shown in Figure 4.5 outlines the iterative design procedure for a Roebel bar featuring a 360–degree transposition, with a focus on optimizing strand number, strand dimensions, and minimizing copper losses. The process can be described in the following step–by–step sequence:

1. **Initial Strand Number:** The design process begins with an initial estimation of the strand number. Parameters such as slot dimensions, axial length, and coil pitch are defined, as they directly influence the strand configuration and copper losses.

2. **Dimensioning Strands:** Based on the slot dimensions and given strand number, the individual strand dimensions are calculated. This step ensures the strands fit within the given slot while maintaining optimal spacing for insulation and maximum copper area.

3. **Magnetic Field Distribution:** The magnetic field distribution within the slot is computed. This information is crucial for estimating AC copper losses, as it directly impacts eddy currents in the winding.

4. **Resistance and Loss Calculations:**

(a) DC Resistance: The DC resistance of the strand configuration is determined.

(b) DC Copper Losses: Using the DC resistance, the DC copper losses are calculated, providing a baseline for total copper losses.

(c) AC Copper Losses: AC copper losses are then derived based on the magnetic field distribution, considering additional losses due to eddy current.

(d) Total Copper Loss: The total copper loss is obtained by combining DC and AC copper losses. This value reflects the overall efficiency of the current strand configuration.

(e) AC Resistance: Once the total copper loss is achieved, the AC resistance of the strand configuration is extracted as the final output. This parameter is essential for further performance analysis of the Roebel bar in operational conditions.

5. **Optimization Check:** The total copper loss is checked to see if it has reached a minimum value. If not, the strand number is increased, and the design process iterates through the previous steps to refine the strand configuration further. This iterative refinement continues until the optimal strand configuration is achieved, ensuring minimized copper losses and enhanced overall efficiency.

4.2 Analytical Approach to Refurbishment and Alternating Winding Configuration for the Existing Generator

The existing Westinghouse generator utilizes diamond coils with 5 turns and 4 parallel circuits (winding diagram can be seen in Figure 4.14). Transitioning from this diamond winding configuration to a wave winding with Roebel bars and a single turn generally necessitates an increase in slot number. This requirement arises because maintaining the same slot number while using Roebel bars reduces the electrical loading, which, to maintain output power, demands an increase in magnetic loading. However, increasing magnetic loading can lead to further saturation within the

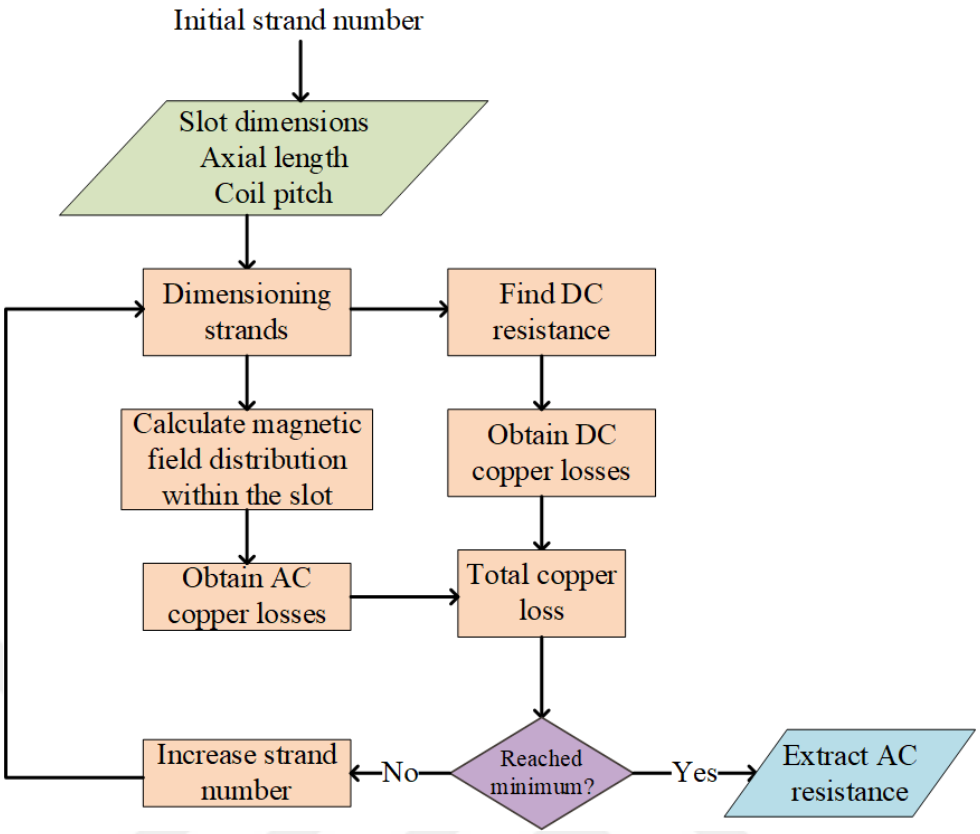

Figure 4.5: Iterative Roebel bar design procedure.

machine. Therefore, to facilitate a successful change in winding type, an increase in slot number is essential.

To quantitatively demonstrate the necessity of increasing the number of slots, the electromagnetic performance of the existing generator is compared to its version constructed with Roebel bars (see Table 4.1). The results indicate that equipping the existing generator with Roebel bars not only results in inferior electromagnetic performance but also increases the rated field current to 722 A, exceeding the rated current of exciter. Therefore, increasing the number of slots is essential to address these issues.

The refurbishment approach begins by outlining the constraints. Mechanical limitations are introduced to streamline the design and manufacturing process; the rotor geometry and stator outer diameter are kept constant. In other words, from a mechanical standpoint, the goal is to alter as few components as possible. Electrically,

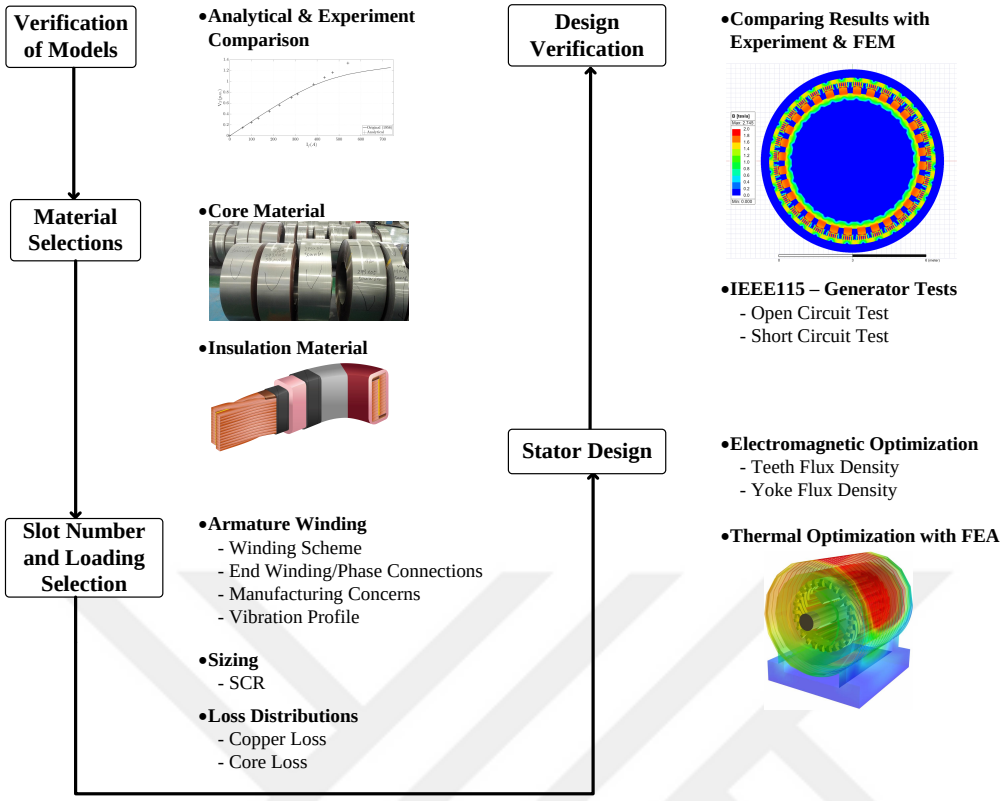

Figure 4.6: Design methodology accounting for operational and structural limitations, adapted from [6].

the output voltage and apparent power are also maintained, and the exciter system remains unchanged. Consequently, the field current must not exceed the exciter circuit's rated limit (722 A) under normal operating conditions. With these constraints in place, the design process proceeds by identifying feasible slot numbers that align with these limitations.

The methodology for the refurbishment design process is illustrated in Figure 4.6. Initially, material selection is carried out. Specifically, the analytical model of the existing generator is used to evaluate the effects of different core materials. An amortization table, shown in Table 4.2, is developed to compare various core materials and assist in selecting the most suitable option. The amortization table shows that using the best core material is a smart choice, as it allows the initial investment to be returned in a short period compared to the generator's lifetime. Therefore, M270–50A

Table 4.1: Comparison of the electromagnetic performance of the existing generator equipped with Roebel bars.

	Existing Generator (Diamond Coil)	**Existing Generator (Roebel Bar)**
# of Parallel Circuit	4	1
Turns/Coil	5	1
Turns/Phase	100	80
Electrical Loading (kA/m)	57.3	45.85
Magnetic Loading (T)	0.9	1.1
Cogging Torque (kN.m)	18.4	28.5
Rated Exciting Current (A)	722	830
Core Losses (kW)	220	280
Rotor Copper Losses (kW)	130.2	179.1
Stator Copper Losses (kW)	125.5	99.9
Total Copper and Core Losses (kW)	475.7	559
Efficiency (%)	97.8	97.6
SCR	1.02	1.67
Teeth Flux Density (T)	1.82	1.98
Yoke Flux Density (T)	1.48	1.42

has been selected as the core material for the new design.

Table 4.2: Amortization table for core material selection.

Amortization Time in Years		**Reference**					
		M270-50AC6	**M290-50AC5**	**M310-50AC5**	**M330-50AC5**	**M350-50AC5**	**M400-50AC3**
Selection	**M270-50AC6**	-	8.56	1.88	2.03	1.61	1.61
	M290-50AC5		-	0.64	1.20	1.11	1.27
	M310-50AC5			-	2.42	1.41	1.50
	M330-50AC5				-	0.99	1.32
	M350-50AC5					-	1.63
	M400-50AC3						-

Additionally, the fundamental winding factor is calculated across various slot num-

bers to establish a look–up table for coil pitch selection. Maintaining an appropriate fundamental winding factor is essential to ensure consistent generator output voltage.

After determining the winding factor variation, candidate machine configurations can be identified. The primary criterion for sizing the new machine is the short-circuit ratio (SCR), which is the inverse of the direct–axis synchronous reactance. SCR is directly related to both machine and grid stability. For hydro generators, an SCR value between 0.8 and 1.6 is typically desired [12]. Therefore, the new design is constrained to maintain SCR within this range.

Analytical computations are carried out using the model presented in Chapter 3. The design of Roebel bars follows the previously outlined methodology. Following the initial design iterations, three candidate configurations were identified, featuring 288 slots, 300 slots, and 324 slots, respectively. Increasing the slot number leads to an increase in electrical loading. To maintain the same output power, magnetic loading is subsequently reduced. As a result, core losses decrease, while copper losses exhibit an increase. The electromagnetic performance of these designs is presented in Table 4.3. The results indicate that the differences in electromagnetic performance among the configurations are relatively minor.

However, the configuration with 300 slots was selected for several reasons:

1. The use of 300 slots can be implemented without modifications to the stator frame, reducing manufacturing costs.

    (a) The current stator frame consists of 60 keybars. Configuring the design with 300 slots results in an allocation of 5 slots per keybar, which does not necessitate any structural modifications. In contrast, configurations with 288 or 324 slots correspond to 4.8 and 5.4 slots per keybar, respectively, requiring adjustments to the lamination angle and modifications to the press plate.

2. The exciter system limits are respected.

3. Cogging torque is significantly reduced (see Table 4.3).

4. Operating temperature of the machine is lowered by 10 to 15°C (refer to Fig-

ure 4.7).

Table 4.3: Candidate designs for refurbishment.

	Existing Gen.	**288/9**	**300/9**	**324/10**
Electrical Loading (kA/m)	57.3	55.1	57.3	61.8
Magnetic Loading (T)	0.90	0.92	0.90	0.80
Cogging Torque (kN.m)	18.4	44.1	5.7	5.6
Core Loss (kW)	220	182	160	151
Stator Copper Loss (kW)	125.5	117	120	131
Field Copper Loss (kW)	130.2	80.3	93.6	98.4
Total Copper and Core Losses (kW)	475.7	394.3	373.6	380.4
Rated Exciting Current (A)	722	551	595	610
Efficiency (%)	97.8	98.1	98.1	98.1
SCR	1.02	1.1	1.1	1.1
Teeth Flux Density (T)	1.82	1.80	1.90	1.70
Yoke Flux Density (T)	1.15	1.30	1.20	1.20

The sizing of the machine is conducted through a parametrized analysis approach. This involves systematically varying slot dimensions, airgap, and winding configuration within a defined parameter space. The final sizing is achieved by verifying compliance with key constraints, especially SCR. The ventilation ducts were redesigned by reducing their thickness and increasing their quantity. This modification enhances the cooling efficiency [8], as demonstrated by the computational fluid dynamics (CFD) analyses comparing the existing and newly designed generators (see Figure 4.7). The flux density distribution for the newly designed machine with 300 slots is presented in Figure 4.8.

As discussed in the previous section, the design of the Roebel bars follows the methodology outlined earlier. Figures 4.9 and 4.10 present the total copper losses, AC resistance, and strand dimensions for varying strand numbers.

As shown in Figure 4.9, for a small number of strands, increasing the strand num-

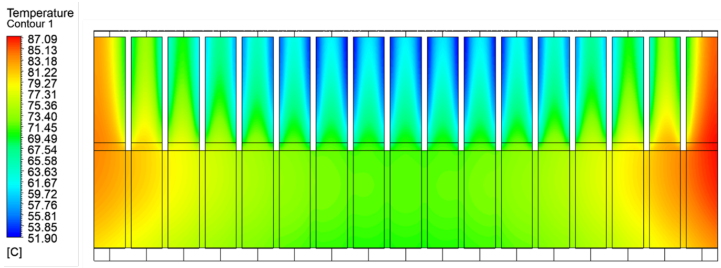

(a) Existing Westinghouse generator (16 ducts with 9 mm duct height).

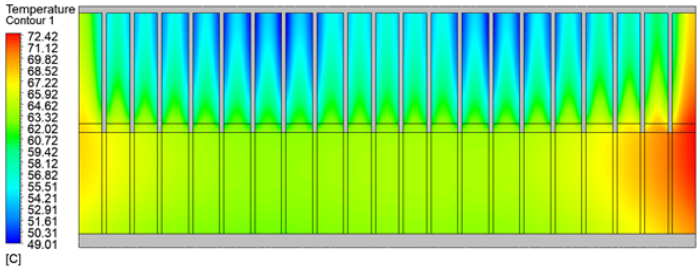

(b) New design with 300 slots (20 ducts with 6.5 mm duct height).

Figure 4.7: Temperature distribution along the axial length for the existing design (a) and the new design (b), with an ambient temperature of 25°C.

ber significantly reduces the AC resistance. However, due to the strand insulation thickness, the DC resistance exhibits a slight increase.

In Figure 4.10, it is observed that the total copper losses decrease significantly up to a certain strand number, even though DC copper losses slightly increase. Beyond a specific 70 strands, the reduction in total copper loss ceases, and a slight increase occurs as the insulation thickness becomes dominant.

Based on these observations, selecting a strand number between 42 and 60 is deemed an optimal choice. Finally, Table 4.4 compares the dimensions of the new and existing designs, highlighting the parameters that have been modified.

In summary, Table 4.1 demonstrates that converting the existing generator's diamond winding to a wave winding with Roebel bars without increasing the number of slots is not a viable option, as the rated field current exceeds the exciter's capacity. Furthermore, maintaining the same number of slots results in a decrease in the generator's efficiency.

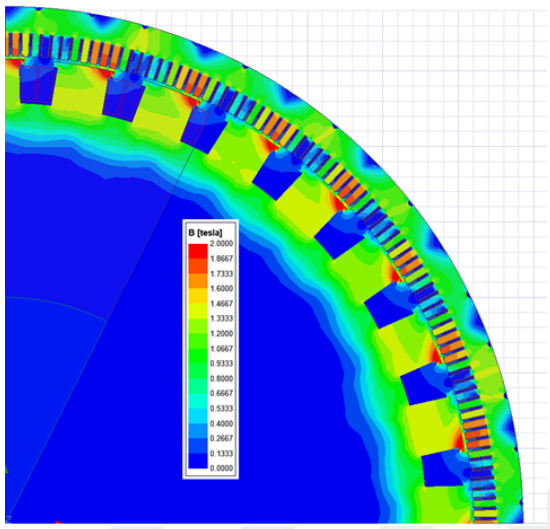

Figure 4.8: Flux density distribution of the new design.

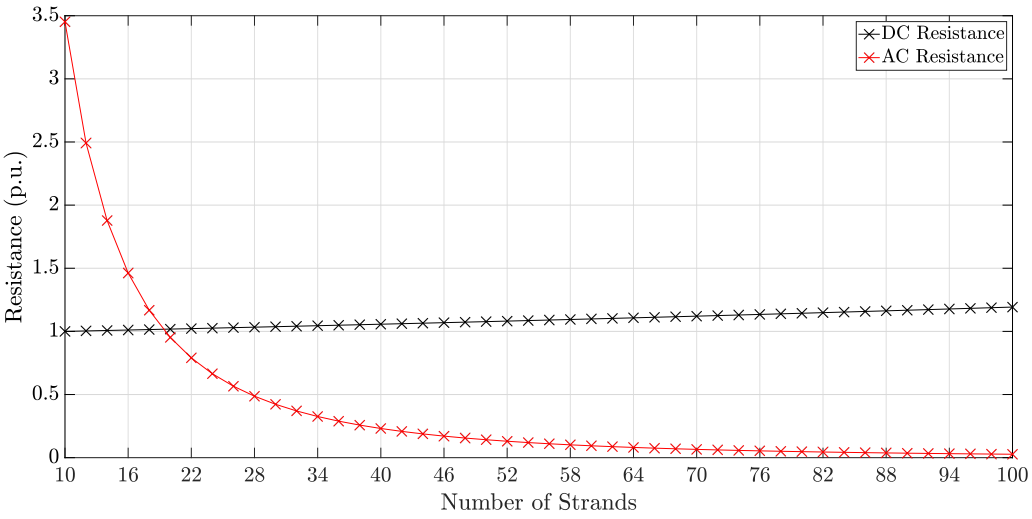

Figure 4.9: Variation of AC and DC resistances with respect to number of strands.

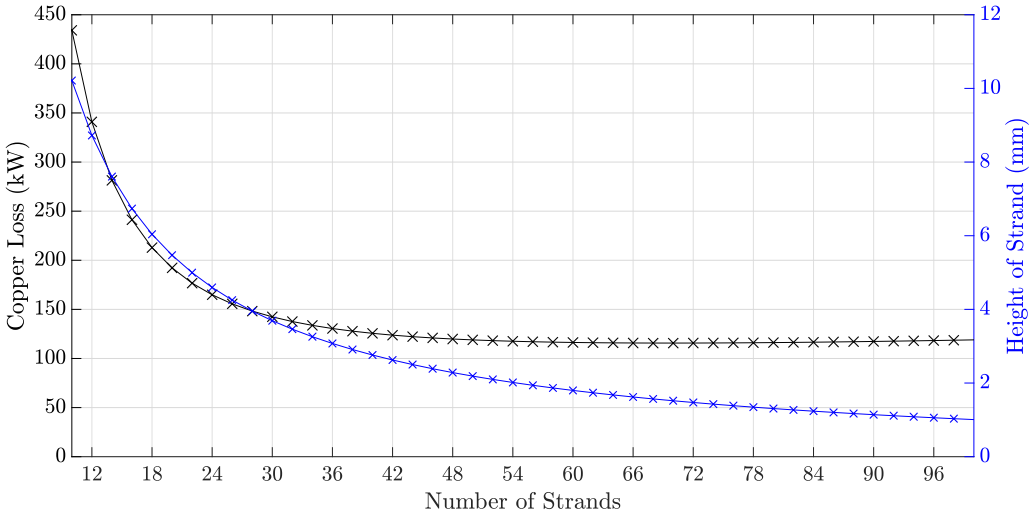

Figure 4.10: Variation of stator copper loss and height of the strands with respect to number of strands.

Table 4.4: Comparison of existing and new design generators in terms of sizing, and winding configurations.

	Existing Generator	**New Design**
Winding Type	Diamond	Roebel
# of Slots	240	300
# of Poles	32	32
Coil Pitch	7	9
Turns per Phase	100	100
# of Lamination Sectors	2	1
Inner Diameter (mm)	6161.6	6161.6
Outer Diameter (mm)	6858	6858
Airgap (mm)	18	18
Slot Width (mm)	25.4	22
# of Ventilation Ducts	16	20
Duct Thickness (mm)	8.5	6.5

In contrast, increasing the number of slots to 300 not only enhances the electromagnetic performance of the machine but also alleviates these limitations. Additionally, the new design with 300 slots leads to a reduction in cogging torque, which is a

primary source of vibration in electrical machines. A more detailed analysis of the vibrational characteristics will be presented in Chapter 5.

4.3 Optimization Algorithm: Non–Dominated Sorted Genetic Algorithm – II

For successful optimization, it is crucial to identify the variables influencing the design. In the context of generator refurbishment, these variables include key machine dimensions and the winding configuration. It should be noted that the outer diameters of the stator and rotor are fixed due to manufacturing limitations set by the operator, EÜAŞ. Expanding the stator's outer diameter would entail significant additional construction costs, resulting in substantial time and financial investment. Consequently, the variables under consideration are the airgap, axial length, and the number and dimensions of the slots.

Once the variables are defined, the objective functions must be established. Objective functions serve as the cost criteria to be minimized within the optimization process. In this specific application, the objectives include minimizing the return on investment measured in terms of operational hours, and enhancing efficiency.

Additionally, any conditions that impose constraints on the design should be formulated as penalty functions. A primary constraint in this case is the short circuit ratio (SCR), which plays a critical role in determining the stability of the generator by indicating the relationship between transient and subtransient performance. The SCR is approximately the inverse of the generator's synchronous reactance (X_s), or for salient pole synchronous machines, the direct–axis reactance (X_d). For hydro generators, the SCR typically ranges between 0.8 and 1.6, with designs adhering to these limits to ensure stability [12]. To safeguard both the generator and grid stability, an SCR value below 0.8 is defined as a penalty condition.

The optimization algorithm defines two objective functions: maximizing efficiency and minimizing the return on investment. Additionally, following constraints are imposed:

- **Rated Power and Voltage:** Maintained at 44.444 MVA and 13.8 kV to comply

with transformer limitations.

- **Field Current:** The existing exciter system will be utilized in the new design. Therefore, the field current must remain within the rated capacity of the exciter system, specified as 722 A.
- **Geometry:** The outer diameter of the stator is preserved to avoid modifications to the stator frame and the generator's concrete base. Additionally, the slot configuration must ensure compatibility with the stator geometry, while the number of slots is constrained to be a multiple of three. Rotor geometry remains unchanged to minimize production costs and downtime.
- **Rated Speed:** The unmodified rotor geometry necessitates maintaining the same rated operating speed.

To further ensure machine safety and facilitate convergence of the optimization algorithm, a penalty function is introduced, mandating that the short circuit ratio (SCR) be greater than 0.8. The algorithm flowchart is presented in Figure 4.11.

Mathematically, the optimization problem is formulated as follows:

$$f_1\left(g, L_s, b_2, h_2, Q\right) = \frac{1}{\eta} \tag{4.4}$$

$$f_2\left(g, L_s, b_2, h_2, Q\right) = \frac{m_{Cu}C_{Cu} + m_{steel}C_{steel}}{\left(\eta - \eta_{old}\right) P_{out} C_e} \tag{4.5}$$

where g denotes the airgap, L_s is the axial length of the stator, b_2 represents the slot opening, h_2 is the slot height, and Q is the number of slots. In the above equations, η represents efficiency as a percentage, m_{Cu} and m_{steel} are the total copper and steel masses, respectively, including wastage, η_{old} is the efficiency of the existing generator (97.8%), and C_e denotes the electricity price. Thus, f_1 represents the maximization of efficiency, while f_2 represents the return on investment.

The constraints are defined as follows:

$$b_2 Q < \pi D_i \tag{4.6}$$

$$D_i + 2h_2 < D_o \tag{4.7}$$

$$Q \mod 3 = 0 \tag{4.8}$$

Penalty function is defined as:

$$p\left(g, L_s, b_2, h_2, Q\right) = \begin{cases} A\left(\frac{1}{SCR}\right)^4 & SCR < 0.8 \\ 0 & \text{otherwise} \end{cases} \tag{4.9}$$

Genetic algorithms (GAs) are optimization techniques inspired by the principles of natural selection and evolutionary dynamics. The core approach of GAs involves iteratively evolving an initial population of solutions to converge toward an optimal or near–optimal result. They are versatile tools that can be employed for both single-objective and multi–objective optimization tasks. The Non–Dominated Sorting Genetic Algorithm–II (NSGA–II) was developed to address the limitations of earlier multi–objective genetic algorithms, which included high computational complexity, absence of elitism, and inflexibility in handling dynamically changing population sizes [34].

NSGA–II has been chosen for this study because of its ability to perform multi–objective optimization with relatively lower computational complexity than other multi–objective GAs. The optimization algorithm is empirically tuned for parameters such as population size, number of iterations, mutation rate, and crossover rate, following the guidelines in [34]. The NSGA–II algorithm is executed with a population size of 200, over 100 generations, utilizing a mutation rate of 0.05 and a crossover rate of 0.7. The convergence plots for both objective functions are presented in Figure 4.12.

Figure 4.13 illustrates that as efficiency increases, the return on investment in years also increases. However, compared to the generator's typical lifetime of approximately 60 years, this increase is marginal. Consequently, this finding emphasizes the importance of selecting the most efficient machine configuration.

One of the optimal designs is constructed with 270 slots, offering an efficiency of 98.33% and a return on investment of 4.7 years. The selection of the 270 slot design is based on the observation that if the design with the highest efficiency were chosen instead, it would require more than half the generator's expected lifetime (over 30 years) to amortize the cost. This observation holds true for other design candidates as well. Consequently, the optimal design can be selected based on specific opera-

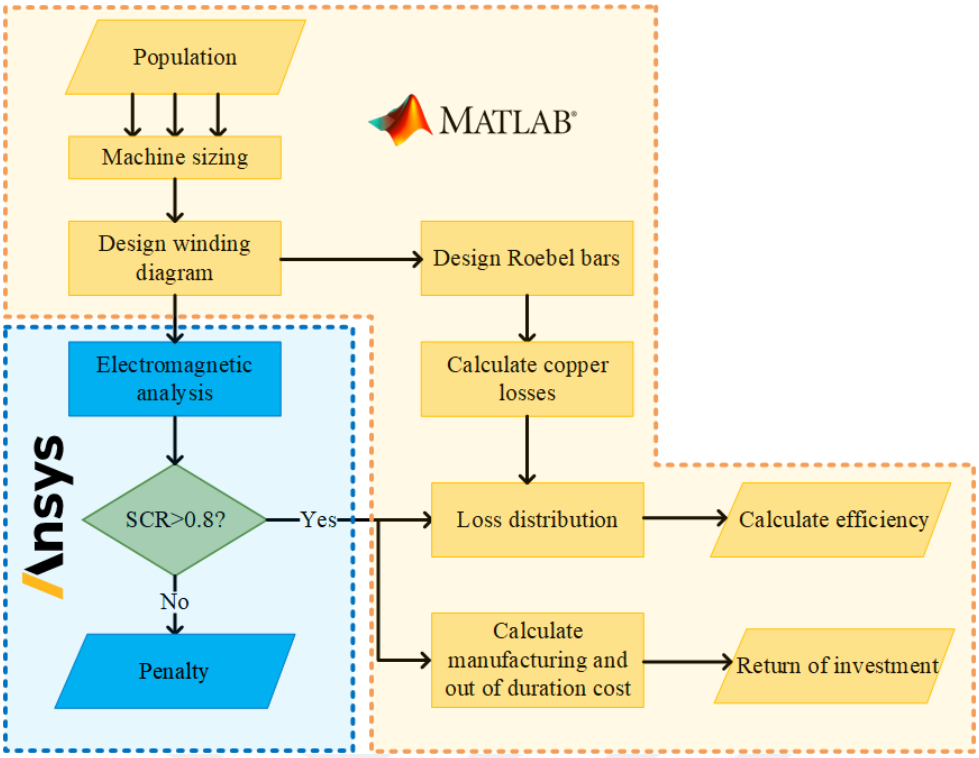

Figure 4.11: Flowchart illustrating the optimization algorithm process.

tional or economic requirements. The dimensions and loss distribution of the selected design are presented in Tables 4.5 and 4.6.

Table 4.5: Dimensions of the selected optimal design.

270 Slot Machine	
D_o (mm)	6858
D_i (mm)	6182.8
g (mm)	10.6
D_r (mm)	6161.6
b_2 (mm)	24.5
h_2 (mm)	98
L_s (mm)	890

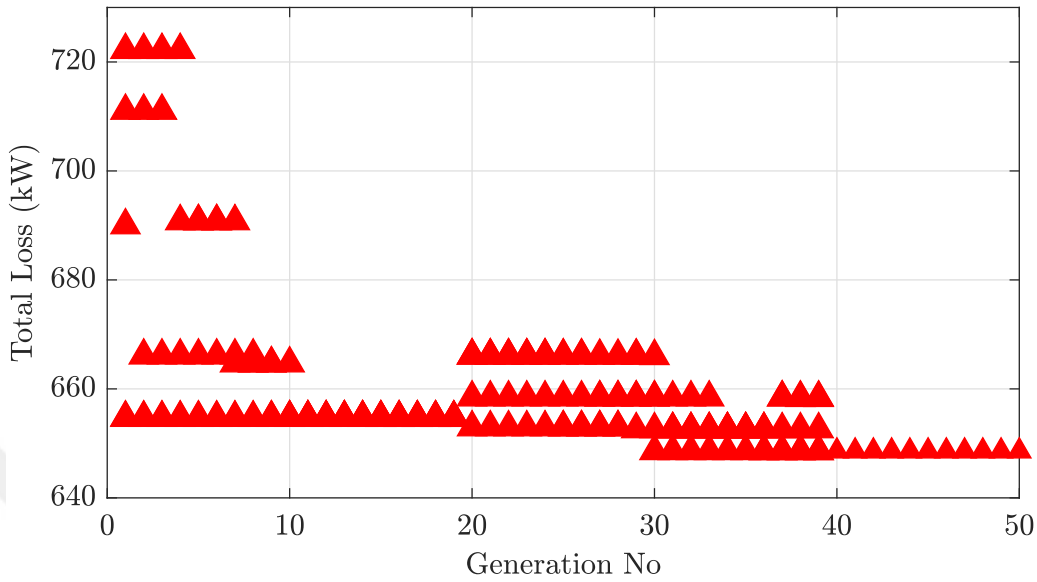

(a) Convergence plot of f_1.

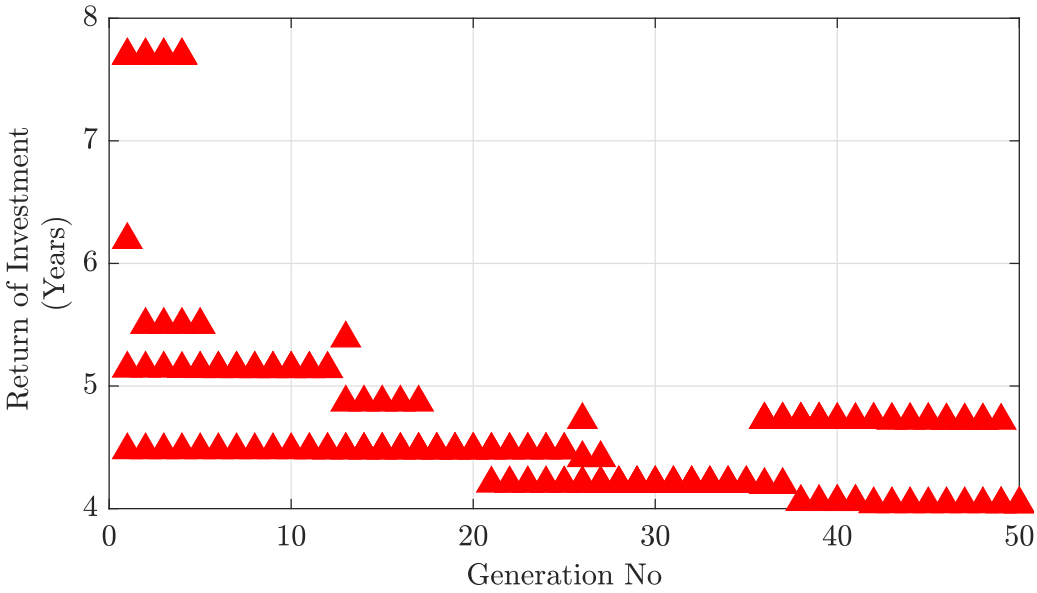

(b) Convergence plot of f_2.

Figure 4.12: Convergence among the generations of optimization algorithm.

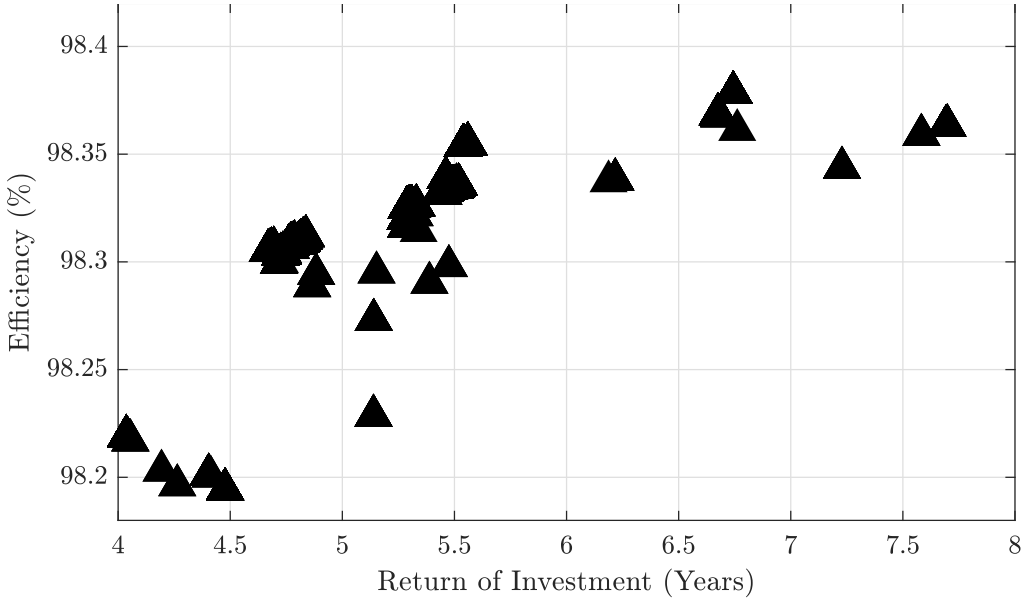

Figure 4.13: Distribution of optimal designs within the cost space.

Table 4.6: Loss distribution of the selected optimal design.

270 Slot Machine	
Stator Copper Loss (kW)	85
Field Copper Loss (kW)	65
Core Loss (kW)	190
Efficiency (%)	98.3

4.4 Conclusion

The analytical approach for refurbishment demonstrates that minor modifications to the existing generator can significantly enhance its efficiency. Furthermore, analytical optimization reveals that efficiency improvements can surpass those achieved with the analytically designed 300 slot machine. However, relying solely on analytical design and optimization can be misleading, as generators are inherently multi–physics systems requiring consideration of thermal and mechanical aspects in addition to electromagnetic performance.

Incorporating mechanical behavior into the optimization process necessitates conducting a 2D finite element analysis to accurately determine the airgap magnetic flux

density (B–field) distribution. While this step ensures a more precise evaluation of the machine's electromagnetic and mechanical performance, it significantly increases computational cost and time (analytically solving an individual takes approximately 10 seconds, whereas FE solution is obtained in approximately 10–15 minutes). To address this, a two-step hybrid approach is adopted:

- **Analytical Electromagnetic Assessment:** Initially, candidate designs are evaluated based on their electromagnetic performance using analytical methods. This phase allows for a faster and computationally efficient screening process to identify promising designs.
- **Mechanical Verification:** From the pool of analytically optimized candidates, designs that satisfy mechanical constraints are selected with vibrational analysis. This strategy reduces the overall computational burden while ensuring that the selected design meets both electromagnetic and mechanical requirements.

By decoupling electromagnetic analysis and mechanical verification, the computational cost is minimized, and significant time savings are achieved without compromising design accuracy.

To summarize, an analytical design procedure has been successfully integrated into the optimization algorithm presented in this chapter. The results demonstrate that, within the imposed design constraints—-including constant rated power, operating voltage, exciter system limitations, rotor geometry, and outer diameter—-the generator's efficiency can be improved up to approximately 98.4%. This enhancement is primarily limited by windage, stray, and excess losses.

Furthermore, the analysis indicates that the initial investment cost can be amortized in a maximum period of 8 years, which corresponds to approximately one–tenth of a typical generator's operational lifespan. The selection of an optimal design depends heavily on the initial budget and specific operational constraints. In this study, the 270 slot configuration was chosen, as it offers a return on investment (ROI) of approximately 4.5 years—equivalent to 5.5% of a generator's expected lifetime—while achieving an improved efficiency of 98.3%.

However, it is crucial to emphasize that the selected design must also be carefully

evaluated from a vibrational perspective to ensure mechanical stability and long–term reliability under operational conditions.

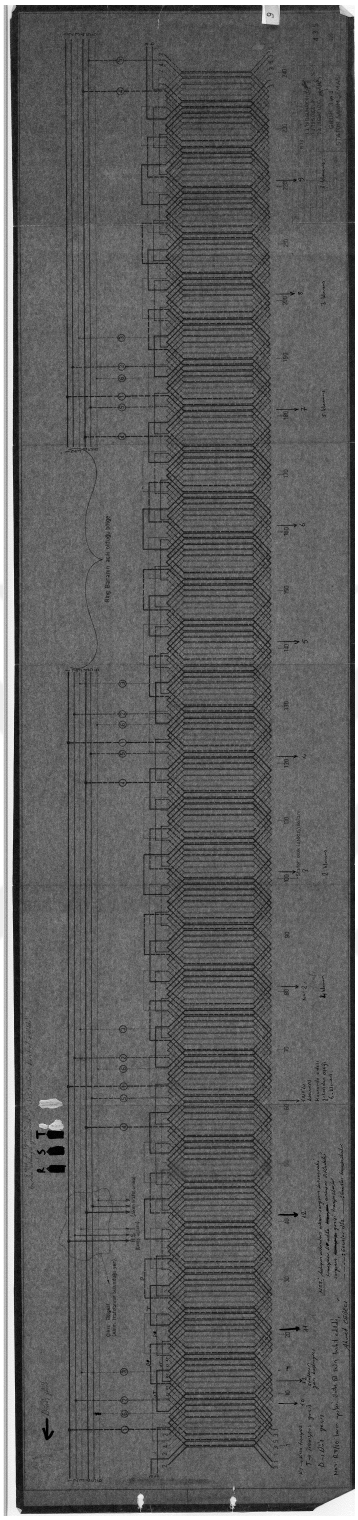

(a) Existing Westinghouse generator (Lap winding).

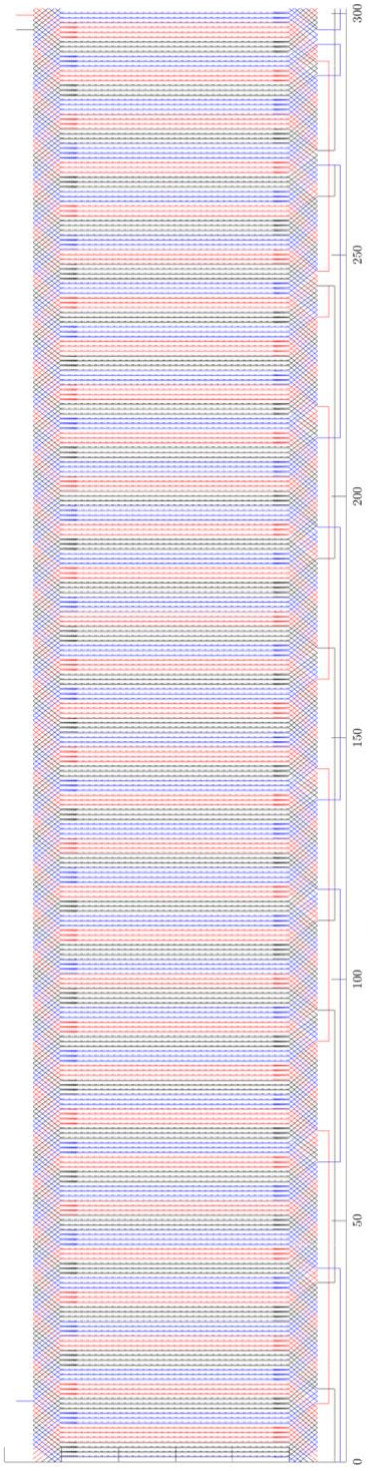

(b) New design with 300 slots (Wave winding).

Figure 4.14: Winding diagrams.

CHAPTER 5

FINITE ELEMENT VALIDATION AND VIBRATION ANALYSIS

Designs based solely on analytical models can lead to inaccurate results, as these models may oversimplify the complexities of real–world systems. Therefore, validating the design with finite element (FE) modeling is crucial to ensure accuracy. Similarly, focusing only on electromagnetic performance can overlook critical mechanical aspects, such as vibration characteristics, which are essential for achieving a longer operational lifespan for the generator.

This chapter details the finite element modeling and validation process for the existing generator. The model is validated using open–circuit (OC) and short–circuit (SC) test results to confirm its accuracy. Based on this validated model, FE models of the candidate designs are developed to ensure their reliability and accuracy.

Additionally, the theory of vibration characteristics is introduced, providing a framework for assessing the vibrational behavior of the candidate designs. The vibration characteristics of each candidate design are then analyzed using this framework. Finally, the chapter discusses the results of these analyses, offering insights into the mechanical and vibrational performance of the proposed designs.

5.1 Finite Element Modelling and Validation of Westinghouse Generator

The finite element method (FEM) is widely utilized for precise modelling of electrical machines. Although it demands significant computational resources, FEM provides highly accurate results. However, this level of modelling requires comprehensive knowledge of the machine's geometry, which can be challenging in older large hydro

generators, as exact geometric details may no longer be available. In such cases, open and short circuit tests are often used to validate the model.

FEM software operates by solving Maxwell's equations over small subdivisions of the machine, referred to as "*meshes*". This approach allows for the calculation of the magnetic flux density (B) within each mesh, revealing a non–homogeneous distribution of the field that analytical models may not capture. Once the field distribution across the machine is determined, the results can be further processed to extract essential parameters such as harmonics, reactances, and losses.

The finite element (FE) model is created in the ANSYS Maxwell environment [26], which offers three distinct solvers for electromagnetic analysis: magnetostatic, transient, and eddy current.

- The magnetostatic solver computes static magnetic fields arising from sources such as DC currents, permanent magnets, and external magnetic fields. This solver is used for time–independent static solutions.
- The transient solver handles time–dependent current and voltage sources, offering a time–dependent solution by analyzing the geometry at different time steps. It also allows for the simulation of translational or rotational motion.
- The eddy current solver simulates the effects of time-varying currents in parallel conductor structures, including eddy current effects in conductors. This is particularly useful for harmonic losses in electrical machines.

In the case of electrical machines, magnetostatic and transient solvers are predominantly employed to compute the magnetic field distribution. While the eddy current solver is typically used for high–frequency excitations, it may also be applied for calculating harmonic losses. Importantly, the modelling approach, including boundary conditions and meshing strategies, remains the same for both magnetostatic and transient solvers. Boundary conditions are critical to utilize the symmetry of the machine within the simulation. Exploiting symmetry in the model can significantly reduce computational time without sacrificing accuracy.

The Westinghouse generator features 240 slots and 32 poles, yielding a slots per pole

per phase ratio of $2\frac{1}{2}$. The machine's symmetry can be analyzed based on the slots per pole per phase value, denoted as q. Specifically, assuming $q = \frac{q_1}{q_2}$, the repetitive section of the machine consists of q_2 poles when q_2 is even. If q_2 is odd, however, the repetitive section comprises $2q_2$ poles [35]. Consequently, the existing generator can be modeled using a $1/16$ symmetry, which includes 2 poles and 15 slots per repetitive section. This approach leverages the machine's inherent periodicity to significantly reduce computational complexity while maintaining accuracy in the analysis.

The resulting finite element (FE) model is illustrated in Figure 5.1. In this representation, the light blue regions correspond to the air surrounding the machine, while the darker blue areas denote the core materials. The rotor and stator windings are depicted in pink and yellow, respectively. The outer diameter of the model is assigned as a vector potential boundary condition. Specifically, this approach reflects the principle that the magnetic field approaches zero at an infinite distance from the source. However, it is not feasible to solve an infinitely large volume in practice. Consequently, a vector potential boundary is employed, designating the outer diameter of the model with a specified vector potential, which is typically set to zero. The model comprises a total

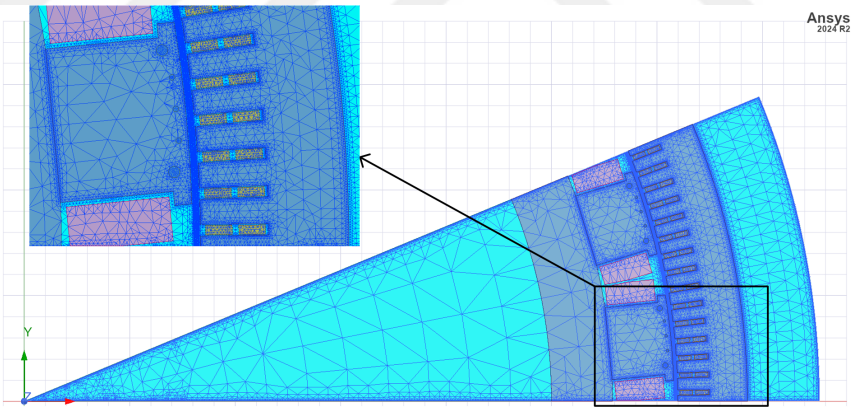

Figure 5.1: Finite element (FE) model of the existing Westinghouse generator (1/16 symmetry).

of 122,146 meshes, with a concentration of mesh elements around critical areas such as the pole tips, airgap, and stator teeth. This strategic meshing approach enhances the accuracy of the finite element analysis by ensuring a finer resolution in regions where variations in the magnetic field and other physical parameters are most significant. The open–circuit B field distribution of the existing Westinghouse generator, as

obtained from FEA, is presented in Figure 5.2.

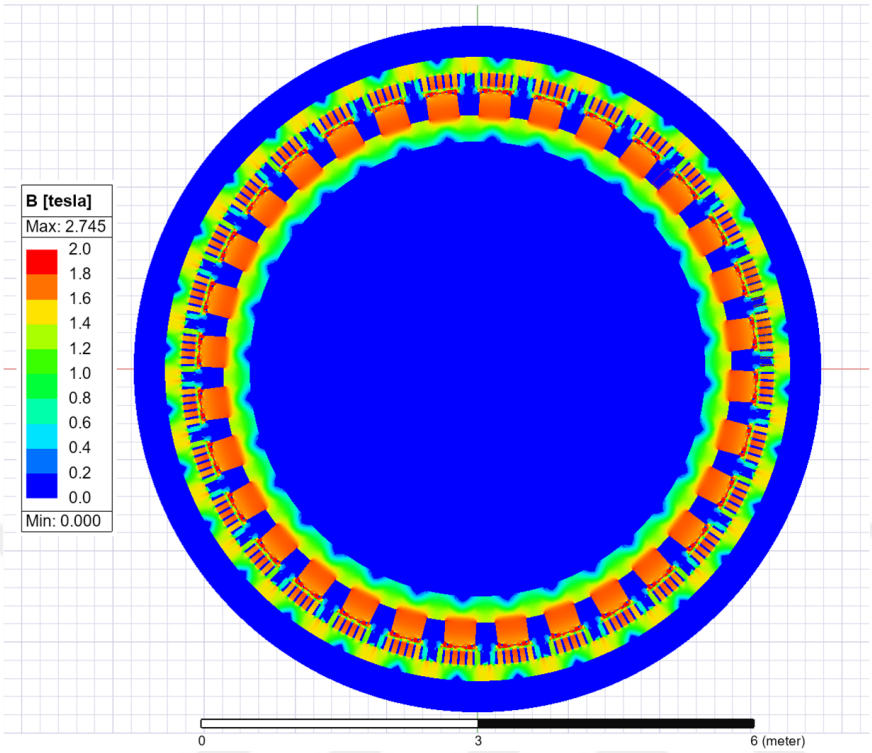

Figure 5.2: B field distribution of the existing Westinghouse generator.

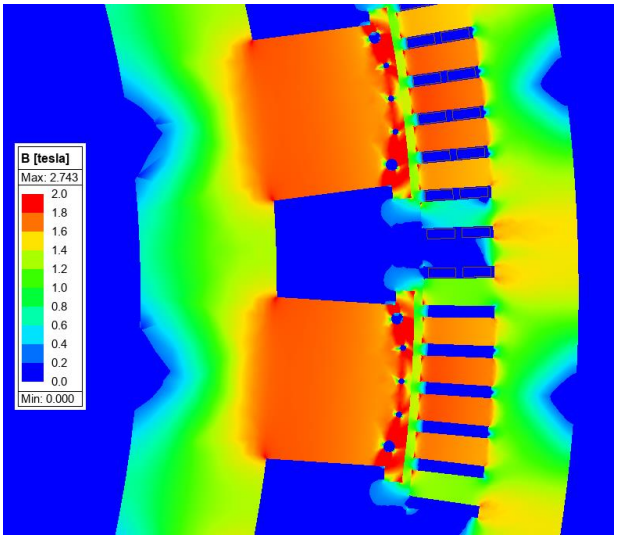

Figure 5.3: Pole–pair B field distribution of the existing Westinghouse generator.

As previously discussed, the validation of the model is achieved through the com-

parison of open–circuit (OC) and short–circuit (SC) curves. The OC curve provides insight into the steady–state performance of the machine, while the SC curve reflects its transient behavior. Therefore, a close agreement between the results obtained from actual tests and finite element (FE) simulations is considered sufficient for validating the model.

5.1.1 Open–Circuit Curve of Existing Generator

Open–circuit (OC) tests, also known as zero power factor tests, are essential for characterizing a hydro generator. These tests must be performed prior to the generator's initial operation. Core losses are also experimentally determined through the open-circuit test [27]. Consequently, OC testing is a critical step during commissioning. The OC curves of the existing generator, including its commissioning test results from 1956, finite element (FE), and analytical model results, are presented in Figure 5.4. The results demonstrate that the airgap line extracted from the analytical model closely aligns with the linear regions of both the finite element (FE) analysis and the commissioning test results. This overlap indicates that the analytical model captures the unsaturated behavior of the generator accurately, validating the model's effectiveness in the linear operational range. However, as saturation occurs, the deviations become more pronounced as expected due to the nature of analytical model.

Figure 5.4 illustrates a noticeable discrepancy between the FEM results and the commissioning test data. While the linear region aligns relatively well, the deviation becomes evident in the saturation region. Several factors contribute to this difference.

Firstly, the material characteristics, such as the B–H and B–P curves, are unknown, making it challenging to accurately model the core material. Additionally, the finite element (FE) model is constructed based on ideal drawings without considering manufacturing and assembly tolerances. In reality, gaps between adjacent laminations increase the core's reluctance, affecting the results. Furthermore, the airgap in the model is based on ideal conditions, while in practice, assembly tolerances cause variations that impact the OC curve. Lastly, material aging plays a significant role, which can be seen in Figure 5.5. Over time, exposure to thermal and mechanical stresses

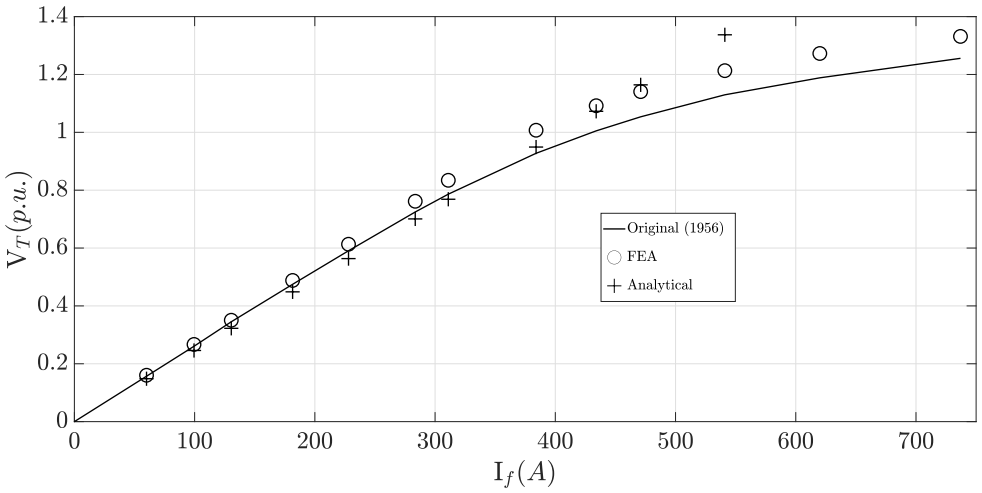

Figure 5.4: Open–circuit (OC) curves of the original machine tested after manufacturing, compared with the finite element (FE) and analytical model results.

can cause the material properties to deviate from those present at the time of manufacturing, further contributing to the observed discrepancies [25]. Figure 5.5 presents data gathered from an on-site test conducted in 2023. The primary objective of this test was to obtain reliable data to resolve inconsistencies identified in the original machine documentation.

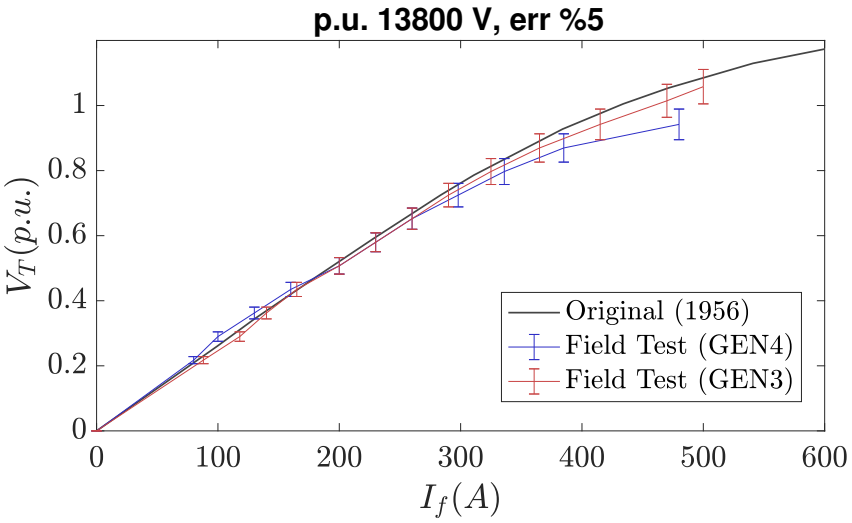

Figure 5.5: Open–circuit (OC) curves of the original machine commissioning test, compared with the on–site test conducted in 2023.

In summary, although the results from the analytical and FE models do not perfectly

match the real test data, they approximate the performance well enough given the available information. With more precise data, such as the exact geometry of the machine, the models could be further refined. For the time being, these models provide a sufficiently accurate representation of the actual machine and can be effectively used for its analysis [25].

5.1.2 Short–Circuit Curve of Existing Generator

The sustained short–circuit (SC) test is a crucial component of the commissioning and maintenance processes for hydro generators, as it provides essential insights into the machine's synchronous reactance, a key factor in steady-state operation. As discussed earlier, no-load losses are determined through the open–circuit (OC) test, while loaded losses are empirically derived from the SC test. Specifically, after determining the windage loss via the retardation test and extracting the core loss from the OC test, the copper losses can be calculated from the sustained SC test [27]. This test also serves to further validate the model, in addition to the OC test. The results of the SC test, as obtained from both the commissioning tests and finite element analysis (FEA), are presented in Figure 5.6. A slight discrepancy between the FEA and the original test results is evident, which mirrors the deviations observed in the open–circuit test (refer to Figure 5.4).

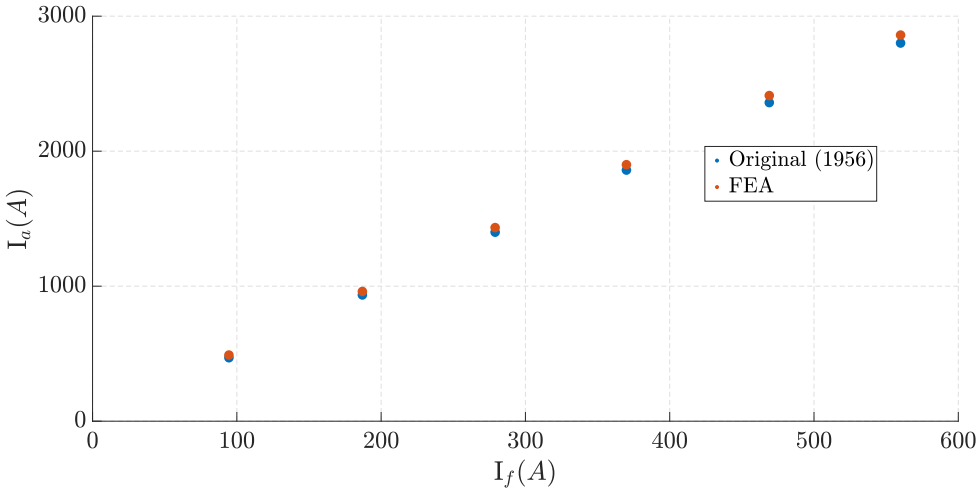

Figure 5.6: Sustained short–circuit curve of the Westinghouse generator, where I_a is rated armature current.

Furthermore, the direct–axis synchronous reactance (X_d) can be derived from the OC and sustained SC curves. Specifically, X_d is defined as the ratio of the field currents at rated armature current during the SC test to the rated armature voltage during the OC test [27], expressed as:

$$X_d = \frac{I_{FSI}}{I_{FG}} \quad p.u. \tag{5.1}$$

where I_{FSI} represents the field current required to produce the rated armature current during the sustained SC test, and I_{FG} is the field current necessary to induce the rated armature voltage during the OC test. Based on this, X_d was calculated to be 0.98 p.u. during commissioning, 0.91 p.u. in the analytical model, and 0.96 p.u. in the finite element analysis (FEA) model.

5.2 Analytical Modelling of Vibrational Deformations

Radial vibrations in hydro generators play a vital role in ensuring reliable operation, minimizing structural damage, and optimizing efficiency over their operational lifespan. These vibrations primarily result from electromagnetic forces in the air gap between the stator and rotor, influenced by factors such as winding layouts, air gap length, and spatial harmonics [36, 37]. Radial vibrations can lead to significant challenges, including structural fatigue, and increased maintenance costs.

Low–order (lower than number of poles) spatial harmonics in the radial force density significantly contribute to radial vibrations, sometimes aligning with structural natural frequencies and amplifying resonant vibrations [36, 38]. In other words, lower mode components in the radial force density can resonate at or near structural natural frequencies. This resonance amplifies radial vibrations, leading to core loosening and excessive stator deformation.

Excessive stator deformation can become permanent if vibrations exceed the structural capacity of the stator frame. Such deformations can lead to unbalanced magnetic pull (UMP), which poses a significant risk to the operational stability of the machine [39]. The presence of UMP has been reported to cause contact between the stator and rotor, a failure mode documented in prior studies [40]. This interaction can result in severe mechanical damage and operational downtime.

Given these risks, it is critical to assess the vibrational behavior of the machine thoroughly to prevent stator deformation and ensure mechanical stability. By ensuring lower vibration levels, the safe operational lifetime of hydro generators can be effectively safeguarded, thus improving their reliability and performance under continuous operation.

Since the electromagnetic performances of the candidate designs are comparable, the selection process prioritizes vibrational behavior as the key criterion. This study extends beyond the conventional scope of refurbishment by incorporating forced vibration as a critical design parameter during the refurbishment process. The primary objective is to identify the sources of radial magnetic forces and evaluate their impact on vibration and cogging torque, utilizing these factors as design criteria to prevent potential breakdowns of the generator.

Electromagnetic forces arise from the magnetic field generated in the airgap of the machine, resulting in an attractive force between the stator and rotor. If the stator frame is inadequately designed or the radial forces are not accurately analyzed, these forces can lead to significant vibrations. These attractions are caused by the magneto–motive forces (MMFs) of the stator and rotor, driven by the magnetic field distribution in the airgap.

The airgap magnetic field is a combination of the rotor and stator fields. The stator field is influenced by the stator current, slot number, and winding configuration. In many cases, fractional slots per pole per phase are employed in winding designs to enhance flexibility. However, this fractional slot arrangement introduces sub–harmonics into the stator MMF, with frequencies lower than the fundamental spatial harmonic of the magnetic field [41]. These sub–harmonics can induce severe vibrations in the stator, posing risks to the machine's structural integrity.

Radial magnetic forces are evaluated by analyzing the spatial distribution of the magnetic field within the airgap. This analysis begins with the introduction of the Maxwell stress tensor (σ), which plays a critical role in characterizing the forces acting in the airgap:

$$\sigma = \frac{B^2(\theta, t)}{2\mu_0} \tag{5.2}$$

where $B(\theta, t)$ is the airgap magnetic field with both space and time components. From

the Maxwell stress tensor, the radial component of the force density can be calculated as:

$$f_r = \frac{B_r^2 - B_t^2}{2\mu_0} \tag{5.3}$$

where f_r is the radial component of the force density, B_r , and B_t are the radial and tangent components of the airgap magnetic field, respectively. Following these, force density in the airgap becomes a function of both space and time:

$$f_r(\theta, t) = \hat{f}_r cos(m\theta - k\omega t) \tag{5.4}$$

where $\hat{f}_r$ is the amplitude of the radial force distribution.

Equation (5.3) demonstrates that if the airgap magnetic field contains an m^{th} harmonic, the resulting radial force density will exhibit a $2m^{th}$ harmonic component. Since the amplitude of the deformations caused by radial forces is inversely proportional to m^4, lower spatial harmonics of the airgap magnetic field are more likely to induce significant and potentially hazardous vibrations [42]. The amplitude of these deformations can be calculated using the relationship provided in [38]:

$$Y_{ms} = \frac{12RR_y^3 f_{rm}}{ET_y^3(m^2-1)^2} \tag{5.5}$$

Here, Y_{ms} represents the deformation caused by the m^{th} spatial harmonic, also referred to as the mode number. R denotes the inner radius of the stator, R_y is the average radius of the stator yoke, T_y is the radial thickness of the yoke, and E is the Young's modulus of the core material.

Although the analytical computation of vibrational forces and deformation amplitudes may not yield highly precise results, it provides a sufficiently accurate basis for comparing different machine designs [42].

The mode number represents the points of maximum attraction between the stator and rotor for $m \geq 2$, as illustrated in Fig. 5.7. Mode numbers less than 2 represent special cases: $m = 0$ corresponds to uniform attraction, while $m = 1$ indicates eccentricity. Specifically, the presence of the $m = 1$ mode in the force density signifies eccentricity and an asymmetrical flux density distribution within the airgap.

The deformation caused by the zeroth mode can be computed as [38]:

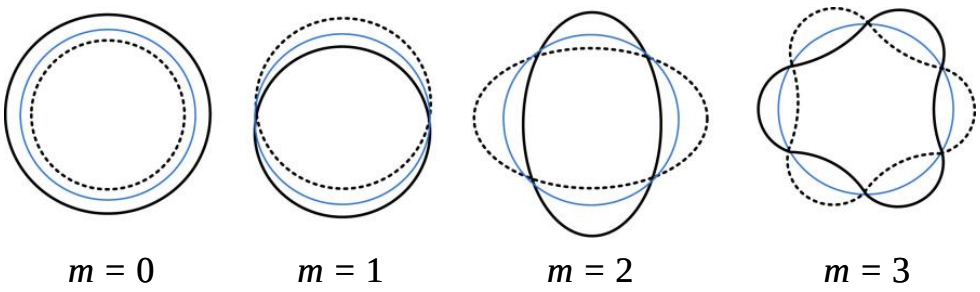

Figure 5.7: Visualization of mode numbers [43].

$$Y_{0s} = \frac{RR_y f_{r0}}{ET_y} \tag{5.6}$$

where Y_{0s} is the amplitude of deformation caused by zeroth mode, and f_{r0} is the amplitude of zeroth mode force density.

Under open–circuit conditions, the lowest harmonic component in the spatial distribution of the radial force density corresponds to the number of poles. Conversely, when the machine supplies an inductive load, the lowest harmonic component is determined by the greatest common divisor (GCD) of the slot and pole numbers.

This phenomenon arises because, during OC operation, no current flows through the armature windings, meaning the armature does not generate any magnetomotive force (MMF). Consequently, the magnetic field in the airgap is solely influenced by the rotor field.

However, under load conditions, when current flows through the armature windings, an armature–generated field is introduced. This armature reaction alters the airgap field, resulting in the presence of lower–order harmonics. These harmonics reduce the symmetry of the airgap field to the GCD of the slot and pole numbers.

When the machine operates under an inductive load, the only scenario in which a generator operates as over-excited, the armature current increases, intensifying the armature field. This, in turn, increases the risk of vibration due to the stronger lower spatial harmonics in the airgap field.

Table 5.1: Winding type of design candidates.

Q	p	$Winding$	GCD	N
240*	32	Lap	16	100
270	32	Wave	2	90
300	32	Wave	4	100
324	32	Wave	4	108

* *Reference machine.*

A smaller GCD indicates a higher probability of generating harmful vibrations, as the deformation amplitude is inversely proportional to m^4, as described in Equation (5.5). According to [38], mode numbers higher than 8 are typically not a practical concern for conventional machines. However, in hydro generators, higher mode numbers may induce significant vibrations due to the machine's eigenfrequencies [36].

On the other hand, a higher GCD increases cogging torque, which can adversely affect machine performance. Therefore, the design process must carefully balance vibrational effects with the mechanical and electromagnetic requirements of the machine.

The candidate design combinations identified in the previous chapter are summarized in Table 5.1. In this table, p denotes the number of poles, GCD represents the greatest common divisor of the slot and pole numbers, and N indicates the number of series turns. For comparison purposes, the existing generator is included as a reference. The parameters of the reference machine are provided in Table 5.2.

5.3 Vibration Characteristics of Generators

The machines considered in this study include configurations with 240 slots (the original design featuring multi–turn lap winding), 270 slots, 300 slots, and 324 slots, all paired with 32 poles, as outlined in Table 4.3. The original lap winding utilizes diamond–type coils, while the candidate wave–winding machines are designed with single–turn Roebel bars.

Table 5.2: Reference machine parameters.

Parameters	Value	Description
S (MVA)	44.444	apparent power
P (MW)	40	real power
D_i (mm)	6197.6	inner diameter
D_o (mm)	6858	outer diameter
g (mm)	18	air-gap
A (kA/mm)	57.4	electrical loading
Q	240	slot number
N	100	turn number
N_p	4	number of parallel branch
X_d (p.u.)	0.98	per unit inductance
T_y (mm)	178.2	yoke thickness

The airgap magnetic field for each configuration is determined using finite element analysis (FEA). Simulations are conducted in the ANSYS Maxwell 2D FE environment with a time–domain simulation setup. The finite–element models are based on the validated model discussed in Section 5.1. All simulations are performed under inductive load conditions (power factor of 0.9) since lower harmonic modes are more prominent when the machine supplies an inductive load. FE models of the 270, 300 and 324 slot machines are presented in Figures 5.8–5.10. The FE model of the 240 slot machine is previously presented in Figure 5.2.

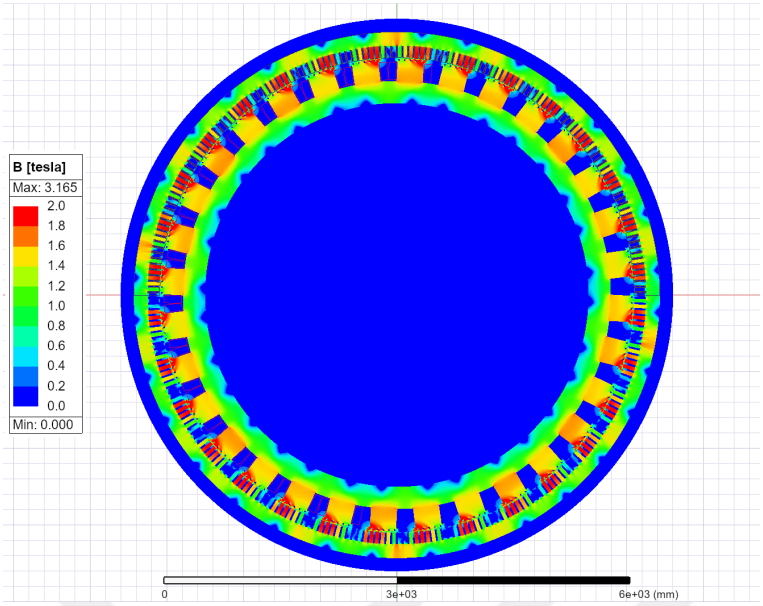

Figure 5.8: Flux density distribution of the 270 slot machine, obtained from ANSYS Maxwell FE environment.

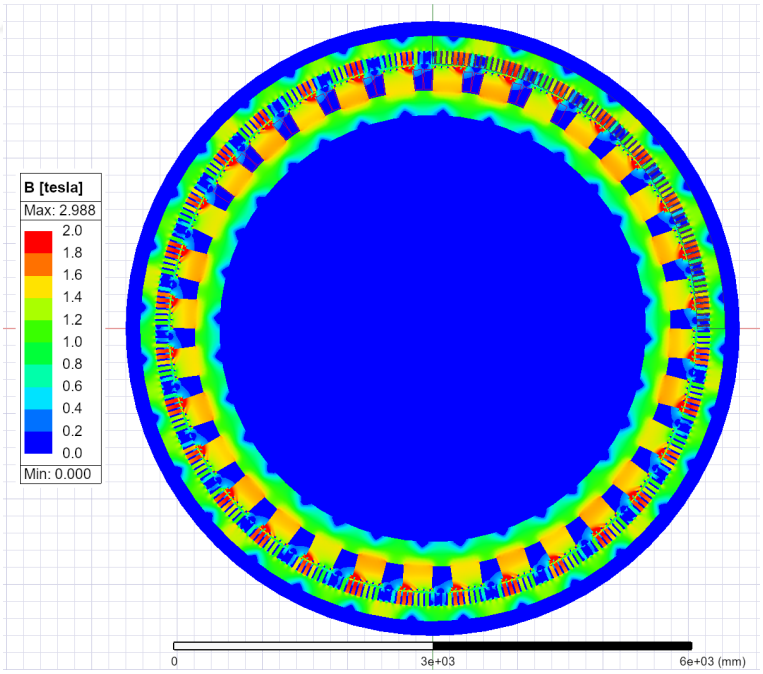

Figure 5.9: Flux density distribution of the 300 slot machine, obtained from ANSYS Maxwell FE environment.

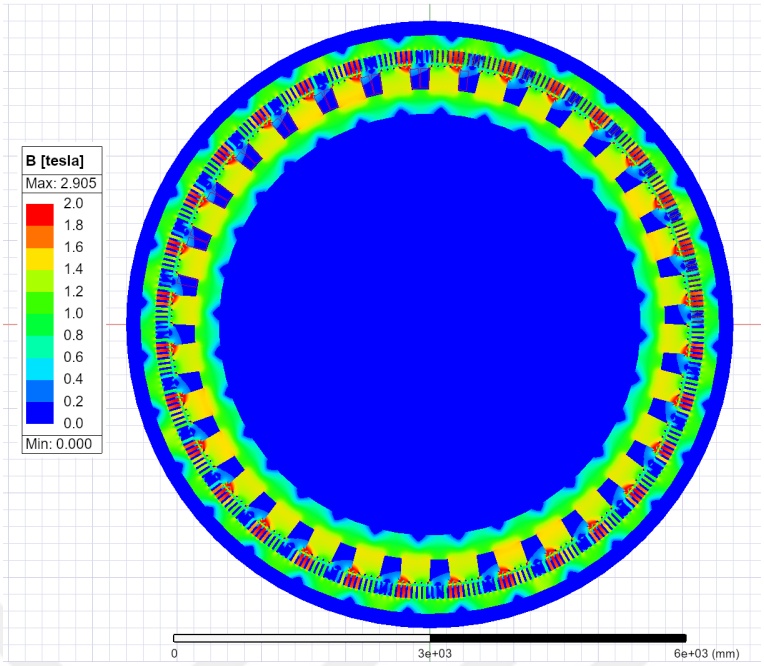

Figure 5.10: Flux density distribution of the 324 slot machine, obtained from ANSYS Maxwell FE environment.

All finite element models are meshed with uniform element sizes, with the total number of mesh elements ranging from approximately 20,000 to 150,000, depending on the machine's symmetry. Following this, the radial force density distribution is computed as described in the previous section.

Next, a Fourier transform is applied to determine the spatial harmonic distribution of the airgap flux density and radial forces. This process effectively involves a double Fourier operation across both spatial and time domains. Initially, space harmonics are calculated at 20 ms after the load is applied. Subsequently, the time harmonics are determined by analyzing the variation in the space harmonic coefficients (a_n and b_n).

5.3.1 Airgap Magnetic Field Distribution

Both tangential and radial airgap flux density components are extracted from FEA, and illustrated in Figure 5.11 for all machines. The harmonic content of the airgap magnetic field should be extracted because the harmonic spectrum of radial forces is

directly related to the airgap flux density harmonics. Fourier transform is performed on both radial and tangential flux densities. Figure 5.12 shows the harmonic content of airgap B–field. Also, a closer view of the radial component of the B–field is presented in Figure 5.13. It is seen that the fundamental spatial component in the flux density is the number of pole pairs. Also, the third–order spatial harmonics of the fundamental component are dominant. Although the subharmonics are smaller in magnitude when compared to the fundamental, their interactions have the capability of creating lower modes according to Equation (5.3).

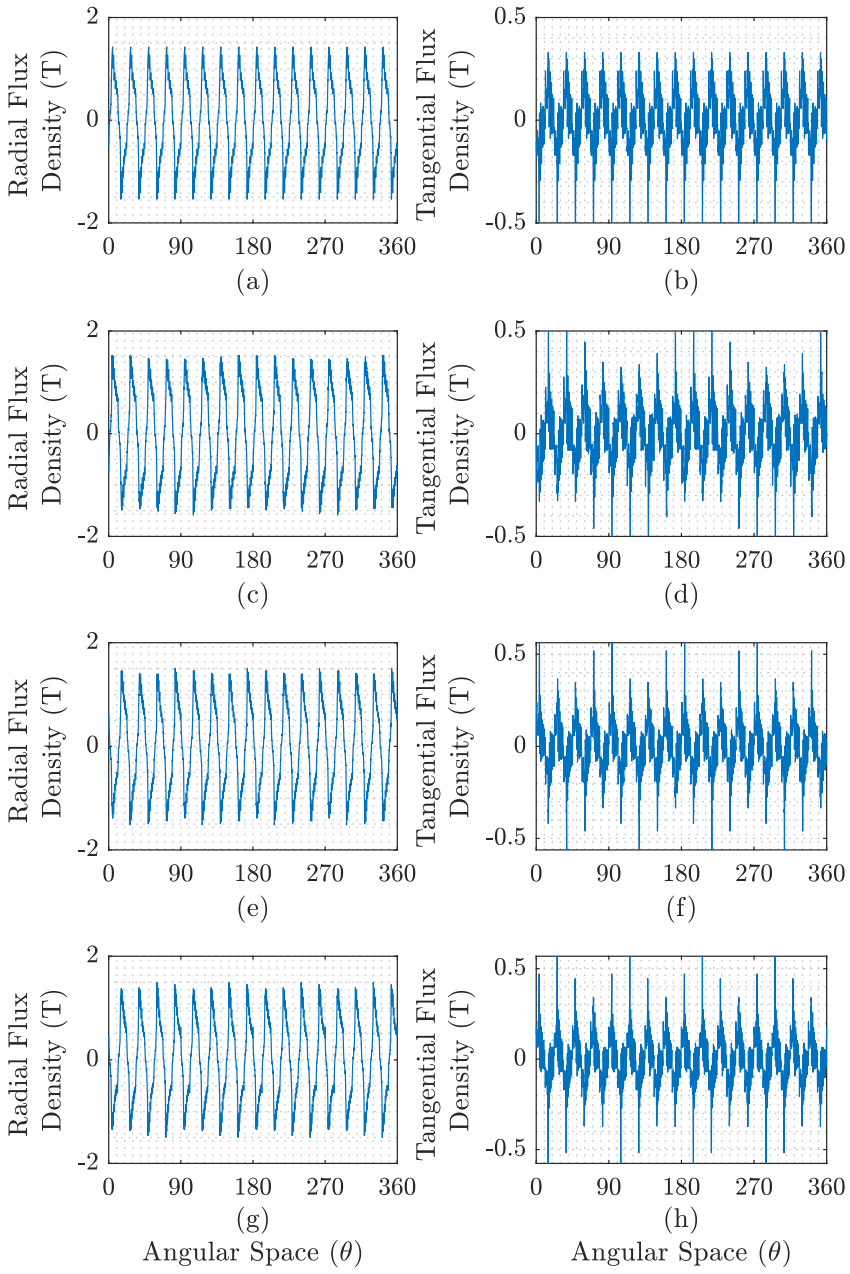

Figure 5.11: Airgap magnetic field under inductive load (lagging with 0.9 power factor). (a) and (b) are the results of existing generator, (c) and (d) are the 270 slot machine, (e) and (f) are the 300 slot machine, (g) and (h) are belonging to the 324 slot machine.

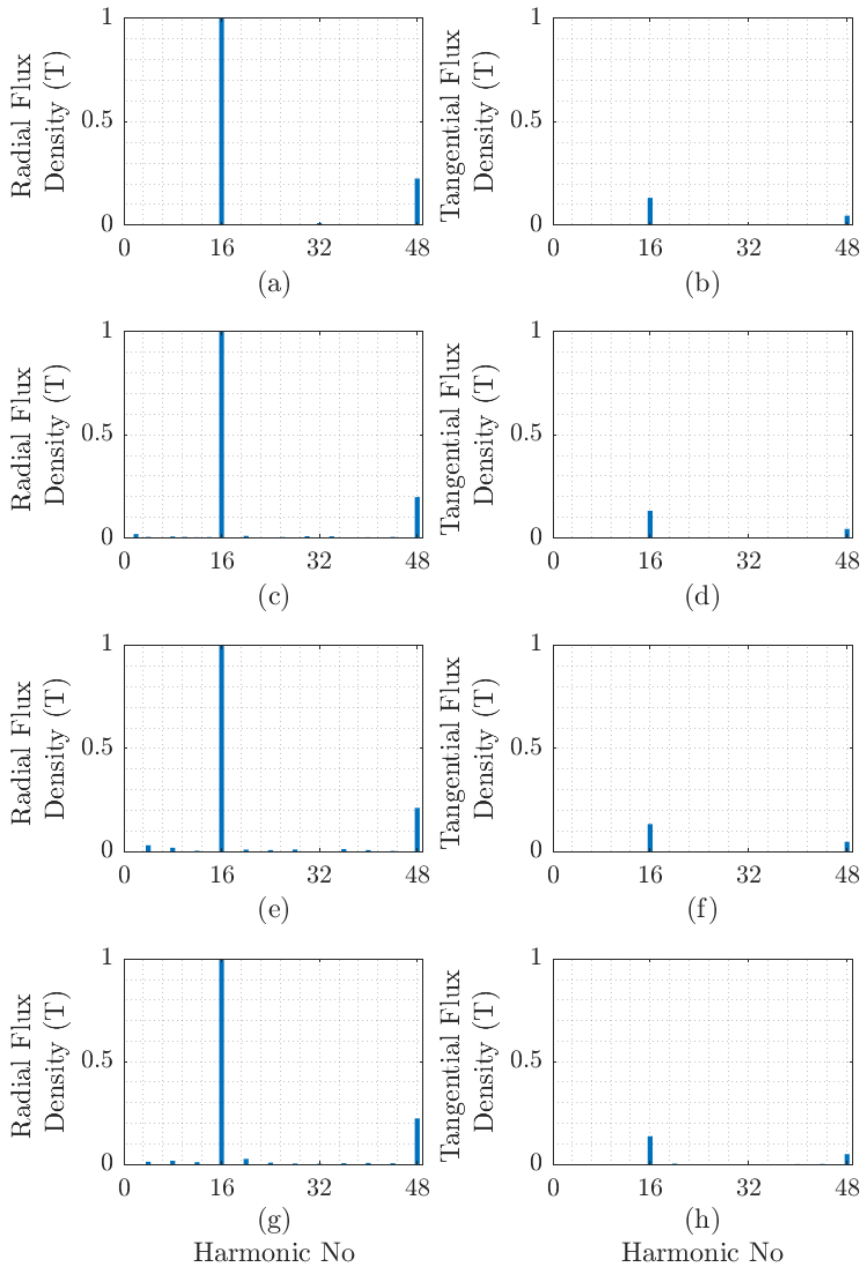

Figure 5.12: Spatial harmonic spectrum of airgap flux density. (a) and (b) are the results of existing generator, (c) and (d) are the 270 slot machine, (e) and (f) are the 300 slot machine, (g) and (h) are belonging to the 324 slot machine.

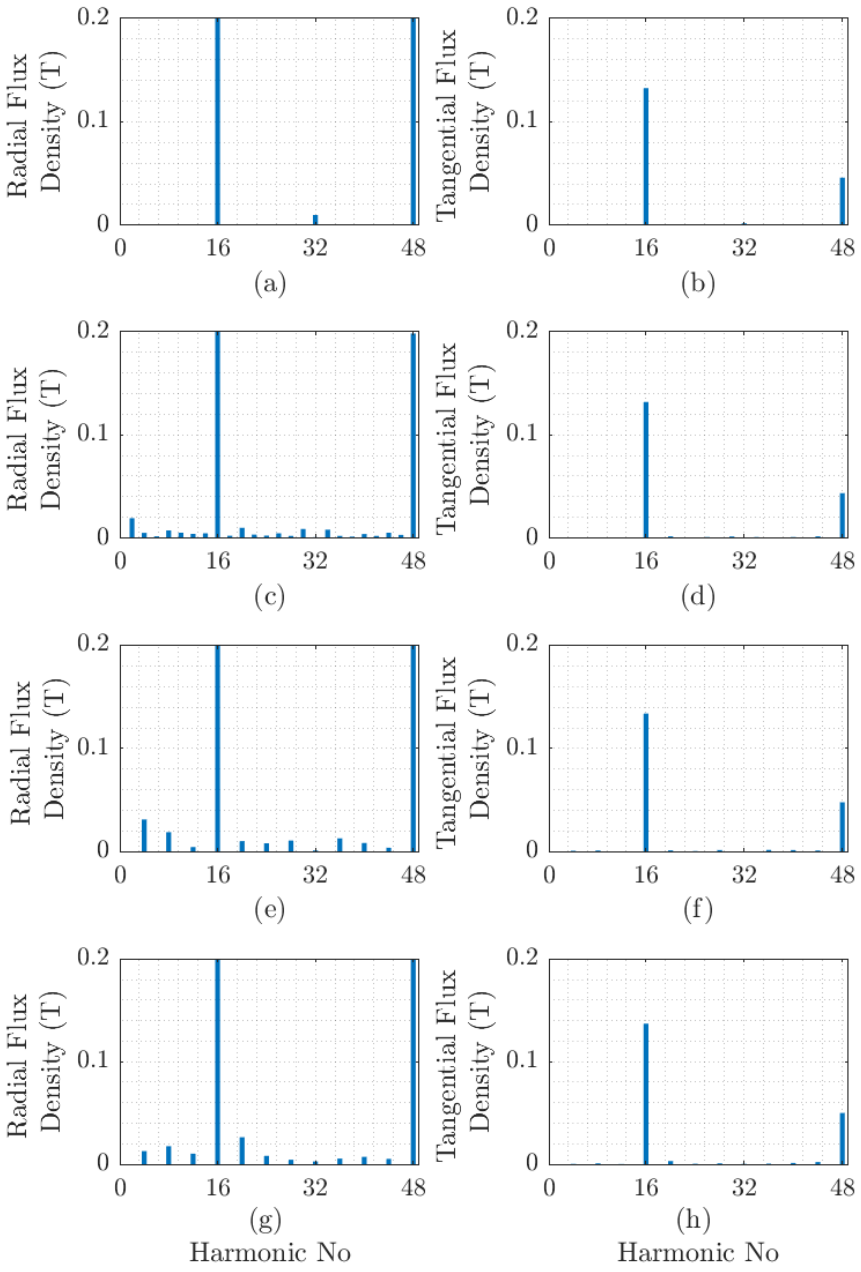

Figure 5.13: Spatial harmonic spectrum of airgap radial flux density. (a), (b), (c), and (d) are the results of existing generator with 240 slot, 270 slot, 300 slot, and 324 slot machines, respectively.

5.3.2 Radial Forces Exerting on the Stator

From Equation (5.3), radial force density is calculated. Corresponding radial force density distributions are presented in Figure 5.14.

Being calculated those, spatial harmonic analysis should be performed on them to evaluate the harmonic contents. The spatial harmonic spectrums of the force densities are given in Figure 5.15. Also, only the dangerous modes are presented in Figure 5.16.

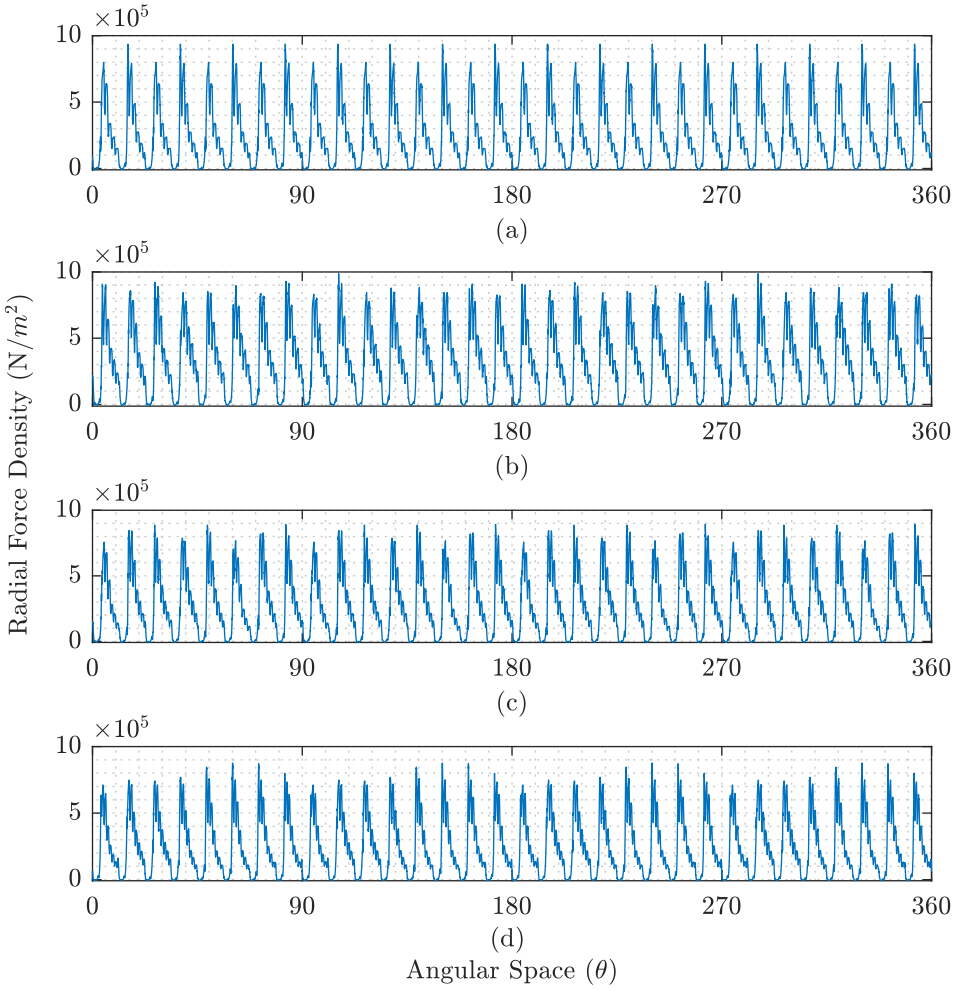

Figure 5.14: Radial force densities in the airgap. (a), (b), (c), and (d) are the results of existing generator, 270 slot, 300 slot, and 324 slot machines, respectively.

The original machine (240 slots/32 poles) has a GCD of 16, which also appears in harmonic content. The vibration due to 16^{th} spatial harmonic is expected to be small in

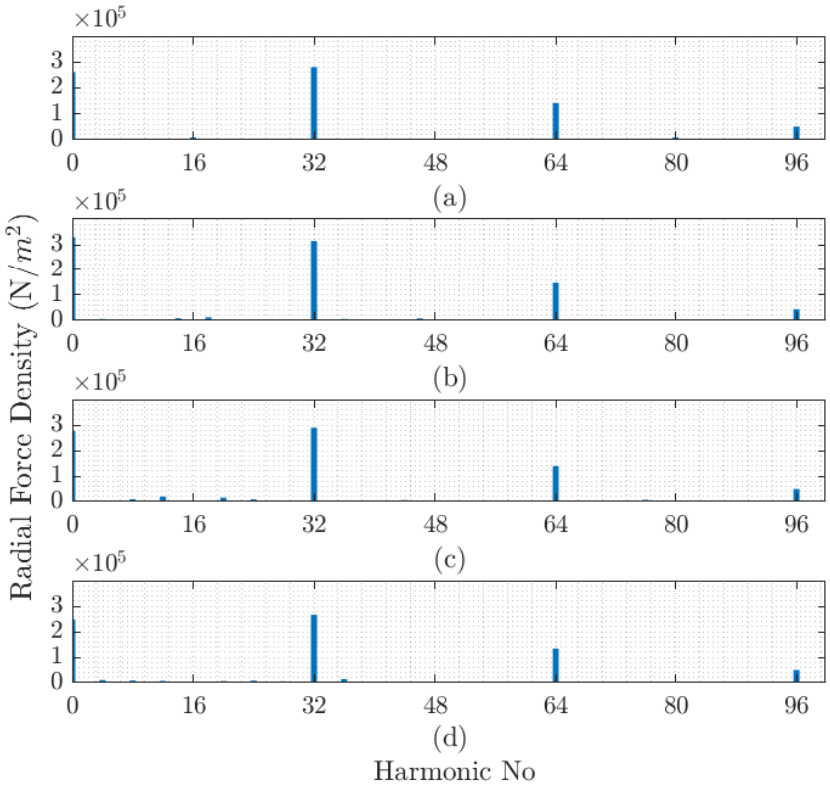

Figure 5.15: Spatial harmonic spectrum of radial force density.

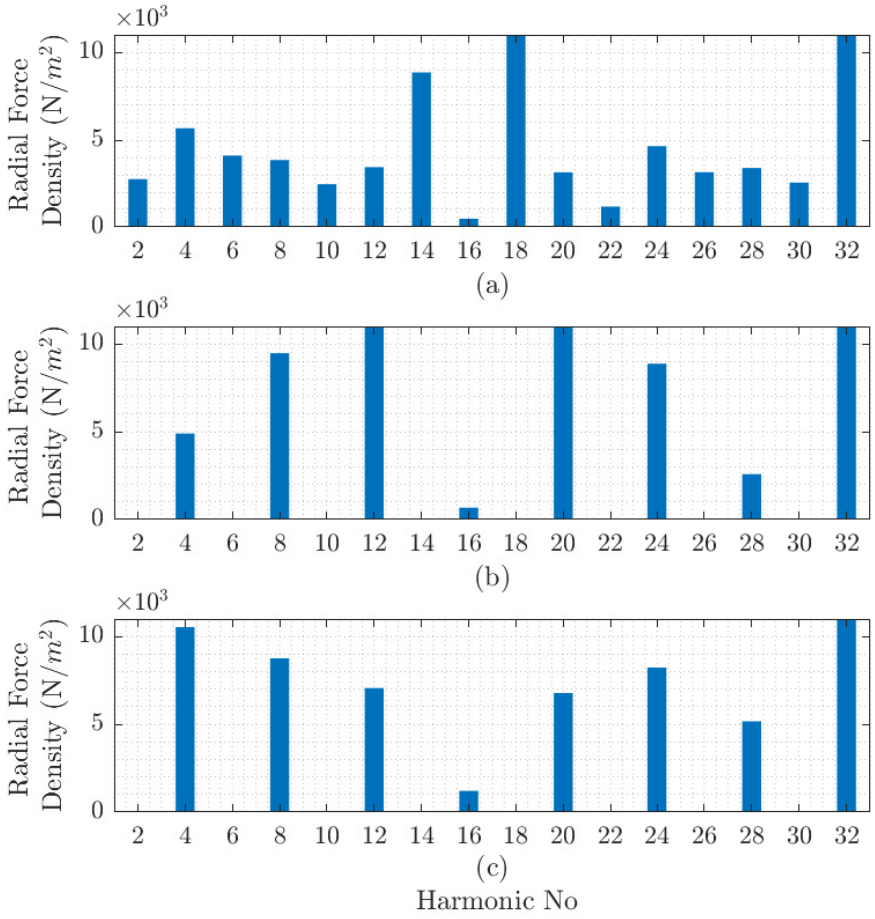

Figure 5.16: Dangerous modes of radial force density. (a), (b), and (c) are the results of 270 slot, 300 slot, and 324 slot machines, respectively.

magnitude; however, it needs to be identified as previously mentioned in Section 5.2. The main drawback of the existing generator may be the cogging torque being the largest. Cogging torque should also be observed to make a viable design selection because it also causes vibrations, which are one of the reasons for long term degradation. As a result, it should also be reduced if possible.

In contrast, the machine with 270 slots has a GCD of 2, which is the lowest among all machines. It indicates that dangerous vibrations may occur. The harmonic spectrum of force density distribution of this machine contains the harmonic orders of 2. As a result, this machine contains all possible dangerous modes; i.e., 2^{nd}, 4^{th}, 6^{th}, and 8^{th} modes. The second mode harmonic is minimal as expected when compared to 4^{th} and 8^{th} ones. As all the harmonics of flux density cause both double of its frequency and 0^{th} mode of vibration (assuming no interaction of other harmonics), the 2^{nd} harmonic in the spatial flux density causes 4^{th} and 0^{th} mode of vibration. However, zeroth mode of deformation is not the main focus of this study. Similarly, the 8^{th} mode of vibration is created with interactions of harmonic orders ± 4, and vice versa. The third–order harmonics of 16^{th} harmonic of flux density with their corresponding sideband harmonics also have the effect of creation of lower mode vibrations but at a smaller level when compared with the fundamental harmonic of 16.

300 and 324 slots both have a GCD of 4, which means their harmonic spectrum contains 4^{th} and 8^{th} modes that can be considered as dangerous.

Upon comparing the amplitudes and lowest mode numbers across all machines, preference emerges for either the original design or the 300 slot machine since the 300 slot machine does not contain 2^{nd} order modes, and has lower 4^{th} mode vibration than the 324 slot. The original design maintains its viability due to its relatively greater GCD, consequently yielding a larger minimum mode number under inductive loads. Consequently, the anticipated radial forces within the existing generator are expected to be minimized. By comparing the cogging torque and zeroth mode deformations, the selection can be made.

Conversely, while the 300 slot design exhibits increased susceptibility to radial forces, it presents a diminished cogging torque in comparison to the existing generator and less vibration than other alternative designs. However, further modal analysis should

be done to ensure the safety of the machine.

5.3.3 Vibration Levels of Generators

There are two type of resonance frequeuncies associated with radial forces denoted as f_0^s and f_m^s whose are shown in the following where Δm refers to mass correction factor which considers tooth and yoke masses, m_t, and m_y [38];

$$f_0^s = \frac{1}{2\pi}\sqrt{\frac{4E}{\rho \Delta m D_m^2}} \tag{5.7}$$

$$f_m^s = \frac{f_0^s T_y m(m^2-1)}{2\sqrt{3}R_y\sqrt{m^2+1}} \tag{5.8}$$

where E is the Young's modulus of the material, ρ is the material density, and D_m is the average diameter of the stator. Δm is defined as:

$$\Delta m = 1 + \frac{m_t}{m_y} \tag{5.9}$$

From the Equations (5.7)–(5.9), it can be inferred that an increase in yoke thickness (T_y) and yoke radius (R_y) leads to a reduction in the resonance frequency. This relationship is particularly significant for hydro generators, which typically operate at lower rotational speeds and higher torques. These operational characteristics necessitate a higher pole number and larger machine diameter, resulting in a thinner yoke. Consequently, hydro generators tend to have lower resonant frequencies.

Lower resonant frequencies pose a critical challenge, as they may coincide with the power frequency (100 Hz) or with radial force excitations arising from lower harmonic modes. This coincidence increases the risk of resonance, which can amplify vibrations and lead to structural damage or breakdown of the machine components. Such risks are particularly pronounced in machines with large diameters and high pole counts, where the reduced yoke thickness further lowers the resonant frequency, making it more susceptible to these excitations [44, 45].

The calculated resonant frequencies are provided in Table 5.3, while the eigenfrequency analysis of the generator, conducted using finite element methods (FEM), is illustrated in Figure 5.17.

The FE model for eigenfrequency analysis was developed by mechanical engineer co–workers. Model is anisotropic, and incorporating the stator frame and keybars. The generator exhibits a resonant frequency of 92.2 Hz at $m = 6$, which closely aligns with the analytical calculations, with a deviation of only 4.2%. The inclusion of the stator frame and keybar positions in the mechanical analysis ensures a comprehensive evaluation. Additionally, an anisotropic material model was employed to account for the effects of stator laminations.

There is a hazardous condition at $m = 6$, which is in close proximity to the resonance frequency of the machine, 100 Hz. A numerical model is created to assess the precision of the analytical calculation. Figure 5.17 displays the eigenfrequency analysis of the generator under investigation.

Table 5.3: Resonant frequencies for various modes, based on analytical calculations given between Equations (5.7)–(5.9). FEM calculation is 92.19 Hz for $h = 6$.

m	f_r **(Hz)**
2	7.47
3	21.12
4	40.49
5	65.49
6	**96.07**
7	132.22
8	173.95

Vibration levels should be corrected considering the resonance gain, η which can be written as where $\Delta_f = \frac{f}{f_m^s}$, and ζ is damping term, which can be approximated as 0.01 as a worst case scenario [38].

$$\eta = \left((1 - \Delta_f^2)^2 + (2\zeta\Delta_f)\right)^{-0.5} \tag{5.10}$$

Analytically calculated vibration levels for different slot numbers are demonstrated in Table 5.4. It should be noted that vibration levels are hazardous (> 7 mm/s [38]) for $Q = 270$ since it contains force excitation at $m = 6$.

Table 5.4: Vibration analyses pertaining to the amplification of resonance for various slot numbers.

	Q = 270		**Q = 300**		**Q = 324**	
m	F ($\frac{N}{mm^2}$)	v($\frac{mm}{s}$)	F ($\frac{N}{mm^2}$)	v($\frac{mm}{s}$)	F ($\frac{N}{mm^2}$)	v($\frac{mm}{s}$)
2	2750	0.89	-	-	-	-
4	5633	2.53	4863	2.23	10344	4.81
6	4084	9.94	-	-	-	-
8	3802	0.75	9444	1.85	8741	1.70
RMS		10.33		2.89		5.10

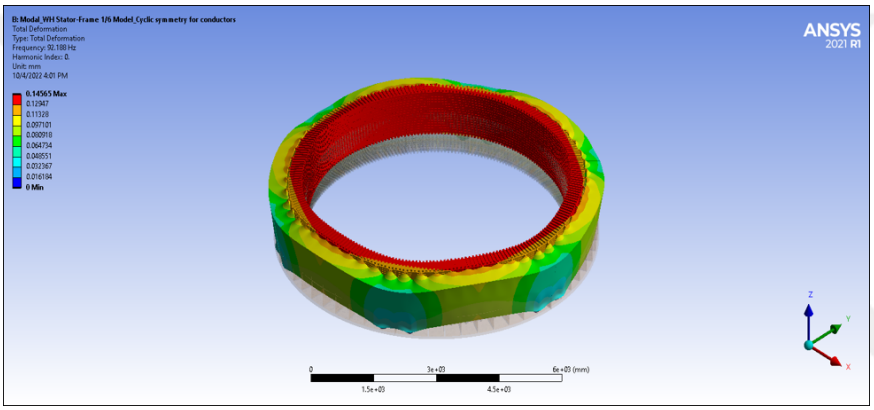

Figure 5.17: Eigenfrequency analysis of the investigated generator.

5.3.4 Cogging Torque and Zeroth Mode Deformation

Unlike the deformations caused by radial forces, cogging torque is proportional with the GCD, i.e. as the symmetry of the machine increases, cogging torque increases. Therefore, the cogging torque is expected to be minimum in the 270 slot machine and maximum in the existing generator. The cogging torque values are extracted from the FEA, and given in Figure 5.18.

Fig. 5.18 clarifies that cogging torque is maximum in existing generator as expected. The cogging torque values of 270, 300, and 324 slots machines are nearly the same. Thus, the selection between candidates depends on mostly their lower mode vibrational characteristics, as discussed in the previous section. These results yield us to

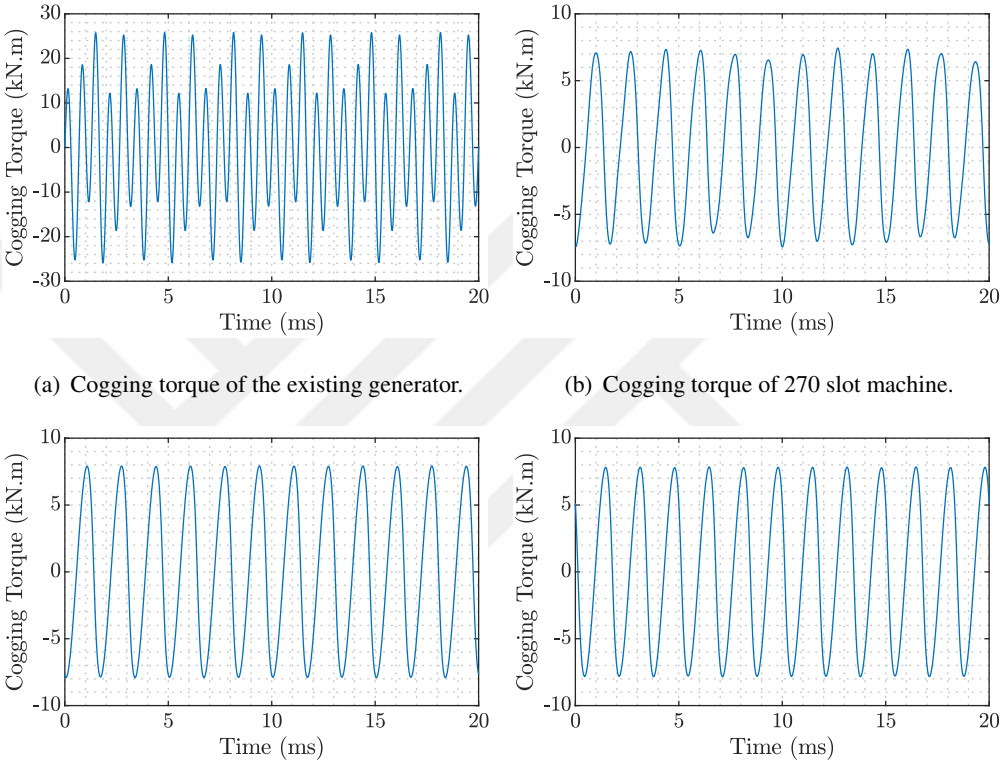

(a) Cogging torque of the existing generator.

(b) Cogging torque of 270 slot machine.

(c) Cogging torque of 300 slot machine.

(d) Cogging torque of 324 slot machine.

Figure 5.18: Cogging torques of reference (existing generator) and candidate machines.

zeroth mode deformation calculation.

The zeroth mode force amplitude can be seen in Figure 5.15. The maximum zeroth mode force density appears in the 270 slot machine. Therefore, maximum deformation is occurring in this machine according to Equation (5.6) given that the stator geometries are similar. The zeroth mode forces are similar in the existing generator and 300 slot machine. It becomes minimum in 324 slot candidate.

Although the 324 slot machine gives the minimum zeroth mode deformation, it has higher 4^{th} mode vibration than the 300 slot machine. Since the existing generator already withstands higher zeroth mode forces, a 300 slot machine can be selected because it offers less 4^{th} mode vibration.

5.4 Conclusions

Comparing all these results (see Table 5.5) with the limitations previously discussed indicates that a viable selection should be either manufacturing the existing generator with the same design or single–turn Roebel bars with 300 slot. When the existing generator is produced with the Roebel bar with the 240 slots, the required field current exceeds the ratings–because the turns–per–phase is reduced. Since there will be no change in the exciter system, building the existing generator with the Roebel bar by using the same stator geometry is almost impossible.

In addition, 270 slot machine contains dangerous modes such as 2^{nd}, 4^{th} and 6^{th}. Knowing that the overall electromagnetic performances of the candidate machines are more or less the same, it is risky to go with the 270 slot machine–since the dangerous vibrations are exerting on the existing frame, which does not in the existing generator.

Furthermore, the 300 and 324 slot machines contain 4^{th} mode as the lowest mode and 8^{th} mode. From Equation (5.5), the deformations are inversely proportional with the m^4. Figure 5.16 shows that the 4^{th} mode amplitude is higher in 324 slot machine, which will cause more deformations than 8^{th} mode. Thus, the 300 slot machine is becoming a viable selection.

Note that the analytical formulations are arguable in terms of accuracy. If the other

	GCD	Dangerous Modes	Vibration Level	Cogging Torque
Existing Generator	16	-	<1 mm/s	18.4 kN.m
270 Slot	2	2, 4, 6, 8	10.33 mm/s	5.1 kN.m
300 Slot	4	4, 8	2.89 mm/s	5.7 kN.m
324 Slot	4	4, 8	5.10 mm/s	5.6 kN.m

6^{th} *mode resonance frequency is close to the power frequency.*

Vibration level of 7 mm/s is considered as acceptable limit.

Table 5.5: Comparison of candidate machines in vibrational perspective.

designs were better regarding their electromagnetic performance and stability, further modal analysis can be conducted for design selection. In contrast, modeling the old stator frame is challenging due to the aging behavior of the materials. In other words, conducting a modal analysis with high accuracy may not be feasible in the matter of time and computation because of modeling challenges and computational burden.

CHAPTER 6

CONCLUSIONS

This thesis presents a comprehensive methodology for the refurbishment of an aging hydro generator, focusing on the replacement of the existing diamond–type coils with Roebel bars. Key challenges, including the modeling of the existing machine and the impact of increased slot numbers on vibration behavior due to the change from lap winding to wave winding, have been addressed. A hybrid approach was proposed, combining analytical design, optimization, and finite element (FE) modeling, along with vibration assessment, to ensure both improved electromagnetic performance and reliable operation.

6.1 Outcomes and Discussions

The methodology begins with the creation of an analytical model for the existing generator using standard electric machinery analysis techniques. Essential parameters, such as machine reactances, which directly influence electromagnetic performance, are calculated. The model is validated through comparison with commissioning test data, ensuring the accuracy of the results.

Following model validation, a candidate machine design is generated using the analytical approach. It is found that minor adjustments to the stator could increase efficiency from 97.8% to 98.1%. This design featured 300 slots while maintaining the original inner and outer diameters. Subsequently, a multi–objective optimization algorithm, specifically the Non–dominated Sorting Genetic Algorithm–II (NSGA–II), is employed. The optimization process, which included iterative design adjustments for the Roebel bars, yields several viable designs, with efficiencies ranging

from 98.2% to 98.4% and payback periods between 4 and 8 years. A 270–slot design is selected based on its shorter payback period and an efficiency of 98.3%.

Given the expected operational lifespan of 30 to 60 years for the newly designed machine, vibrational analysis is performed to ensure long–term safety and operational reliability. FE models of the candidate designs is created based on the validated model of the existing generator, enabling the extraction of the spatial flux density distribution in the airgap. These models is further used to calculate radial force densities, which plays a crucial role in the vibration analysis. Although analytical methods provided initial estimates of vibration trends, existing generator is used as reference. A more accurate assessment is achieved through modal analysis, which identifies resonance frequencies that could potentially cause operational issues. It is found that 6^{th} mode resonance frequency close to the power frequency of 100 Hz, posing a significant risk of harmful vibrations. Consequently, 270 slot machine is deemed unsuitable because there exists 6^{th} mode in radial force density, and vibration level is around 10 mm/s, which is beyond than the acceptable limit of 7 mm/s. In contrast, the 300–slot design, with no 6^{th} spatial harmonics and lower vibration levels, is identified as the most reliable option. Comparison of vibrational behaviors of the 270 and 300 slot machines are given in Table 6.1.

This study demonstrates the importance of not solely relying on electromagnetic performance when designing generators, as it may lead to misleading conclusions. Although the 270–slot design shows the best theoretical electromagnetic performance, its vibration issues made it unsuitable for long–term use. The 300–slot design, however, provides a balanced solution, optimizing both electromagnetic and vibrational characteristics. A comparative analysis between the existing generator and the proposed 300-slot design is presented in Table 6.2.

This research contributes valuable insights into the refurbishment of hydro generators, emphasizing the need to consider both electromagnetic performance and vibration characteristics in the design process. The hybrid methodology, combining analytical, optimization, and finite element approaches, offers a robust framework for the design and long–term operation of refurbished machines.

	Q = 270	**Q = 300**
m	**v** ($\frac{\mathbf{mm}}{\mathbf{s}}$)	**v** ($\frac{\mathbf{mm}}{\mathbf{s}}$)
2	0.89	-
4	2.53	2.23
6	9.94	-
8	0.75	1.85
RMS	**10.33**	**2.89**

Table 6.1: Comparison of vibration levels of 270 and 300 slot designs.

	Existing Generator	**New Design**
Winding Type	Diamond	Roebel
Number of Slots	240	300
Turns per Coil	5	1
Number of Parallel Circuit	4	1
Efficiency	97.8 %	98.1%
SCR	1.02	1.1
Cogging Torque	18.4 kN.m	5.7 kN.m
Airgap	18 mm	18 mm
Stator Inner Diameter	6197.6 mm	6197.6 mm
Stator Outer Diameter	6858 mm	6858 mm
Number of Ventilation Ducts	16	20
Height of Ventilation Ducts	9 mm	6.5 mm

Table 6.2: Comparison of the existing Westinghouse generator and new design machine.

6.2 Potential Improvements and Future Work

While this thesis has provided a thorough investigation into the refurbishment of hydro generators and offered a hybrid methodology for rewinding of an old hydro generator, there are several areas for further improvement:

- This study was constrained by several limitations, including the exciter circuit, unaltered rotor geometry, and fixed outer diameter. The impact of rotor geometry on vibration characteristics was not explored, but future work could focus on optimizing rotor pole shapes, as these may influence vibration behavior. Research into the effects of pole shape optimization in hydro generators is suggested [46, 47, 48].
- The reduction of unbalanced magnetic pull in wave windings, which can be challenging due to the series connection of all turns unlike the use of parallel circuits. Investigating methods to mitigate unbalanced magnetic pull in machines with wave windings could enhance the safety and performance of these machines.
- While the effect of core materials on electromagnetic performance was considered in this study, further research into the role of insulating materials and manufacturing methods for Roebel bars could lead to more accurate designs. Investigating these factors would also ensure longer operational lifespans for Roebel bars, thus improving the overall reliability and durability of hydro generators.

REFERENCES

[1] U.S. Department of Energy, “Types of Hydropower Plants,” 2024.

[2] Hannah Ritchie and Max Roser, “Renewable Energy,” 2024.

[3] International Energy Agency, “Hydroelectricity,” 2024.

[4] International Hydropower Association, “Discover Facts About Hydropower,” 2024.

[5] P. G. Özuyar, E. C. Gürcan, and E. Bayhantopçu, “The policy orientation of turkey’s current climate change strategy,” *Belt & Road Initiative Quarterly*, vol. 2, no. 3, pp. 31–46, 2021.

[6] N. Tosun, G. Gülletutan, M. S. Yakut, D. Alp Yilmaz, Bayer, and O. Keysan, “Winding type alternation of a refurbished old generator,” in *2023 IEEE Workshop on Electrical Machines Design, Control and Diagnosis (WEMDCD)*, pp. 1–6, 2023.

[7] R. of Turkey Ministry of Energy and N. Resources, “Türkiye national energy plan.” https://enerji.gov.tr/bilgi-merkezi-enerji-hidrolik-en, 2022.

[8] M. M. Znidarich, “Upgrading and uprating of hydro generators: An australian perspective,” *Australian Journal of Electrical and Electronics Engineering*, vol. 10, no. 1, pp. 75–84, 2013.

[9] M. S. Yakut, G. Gülletutan, N. Tosun, and O. Keysan, “Rewinding of old 44 mva hydro generator considering vibrational forces,” in *2024 International Conference on Electrical Machines (ICEM)*, pp. 1–7, 2024.

[10] A. Phyrönen, J. Nerg, and P. Kurronen, *Design of Rotating Electrical Machines*. Chichester, UK: John Wiley & Sons, 2nd ed., 2016.

[11] P. Kundur, *Power System Stability and Control*. New York, NY: McGraw-Hill, 1994.

[12] G. Mottershead, S. Bomben, I. Kerszenbaum, and G. Klempner, *Handbook of Large Hydro Generators: Operation and Maintenance*. 2021.

[13] Ansaldo Energia, "Hydrogenerators," 2024.

[14] M. M. Znidarich, "Hydro generator stator cores part 1 - constructional features and core losses," *2008 Australasian Universities Power Engineering Conference*, pp. 1–8, 2008.

[15] M. Znidarich, "Hydro generator high voltage stator windings: Part 1 – essential characteristics and degradation mechanisms," *Australian Journal of Electrical and Electronics Engineering*, vol. 5, no. 1, pp. 1–17, 2008.

[16] M. Znidarich, "Hydro generator high voltage stator windings: Part 2 - design for reduced copper losses and elimination of harmonics," *Australian Journal of Electrical and Electronics Engineering*, vol. 5, no. 2, pp. 119–135, 2009.

[17] M. Znidarich, "Hydro generator high voltage stator windings: Part 3 - stator winding slot support systems," *Australian Journal of Electrical and Electronics Engineering*, vol. 6, no. 1, pp. 1–10, 2009.

[18] M. Znidarich, "Hydro generator high voltage stator windings: Part 4 – type and routine production testing," *Australian Journal of Electrical and Electronics Engineering*, vol. 6, no. 2, pp. 93–108, 2009.

[19] V. O. Belko, Y. K. Petrenya, A. M. Andreev, A. M. Kosteliov, and M. B. Roitgarz, "Numerical simulation of discharge activity in hv rotating machine insulation," in *2019 IEEE Conference of Russian Young Researchers in Electrical and Electronic Engineering (EIConRus)*, pp. 800–802, 2019.

[20] M. W. Smith, "Waterwheel generators and synchronous condensers for long transmission lines," *Transactions of the American Institute of Electrical Engineers*, vol. XLII, pp. 1043–1053, 1923.

[21] C. F. Wagner, "Damper windings for water-wheel generators," *Transactions of the American Institute of Electrical Engineers*, vol. 50, no. 1, pp. 140–151, 1931.

[22] E. I. Pollard, “Calculation of no-load damper winding loss in synchronous machines,” *Transactions of the American Institute of Electrical Engineers*, vol. 51, no. 2, pp. 477–481, 1932.

[23] EPİAŞ Transparency Platform, “Real-Time Electricity Generation Data,” 2024.

[24] M. M. Znidarich, “Hydro generator stator cores part 2 - core losses, degradation mechanisms, testing and specification,” in *2008 Australasian Universities Power Engineering Conference*, pp. 1–9, 2008.

[25] J. C. Akiror, P. Pillay, and A. Merkhouf, “Challenges in modeling of large synchronous machines,” *IEEE Transactions on Industry Applications*, vol. 54, no. 2, pp. 1652–1662, 2018.

[26] Ansys, Inc., “Electronics Products,” 2024.

[27] “Ieee guide for test procedures for synchronous machines part i—acceptance and performance testing part ii—test procedures and parameter determination for dynamic analysis,” *IEEE Std 115-2009 (Revision of IEEE Std 115-1995)*, pp. 1–219, 2010.

[28] F. Carter, “Air-gap induction,” *Electrical World and Engineering*, vol. XXXVIII, no. 22, pp. 884–888, 1901.

[29] C. Steinmetz, “On the law of hysteresis,” *Proceedings of the IEEE*, vol. 72, no. 2, pp. 197–221, 1984.

[30] G. Bertotti, “General properties of power losses in soft ferromagnetic materials,” *IEEE Transactions on Magnetics*, vol. 24, no. 1, pp. 621–630, 1988.

[31] L. A. Kilgore, “Calculation of synchronous machine constants- reactances and time constants affecting transient characteristics,” *Transactions of the American Institute of Electrical Engineers*, vol. 50, no. 4, pp. 1201–1213, 1931.

[32] L. A. Kilgore, “Effects of saturation on machine reactances,” *Transactions of the American Institute of Electrical Engineers*, vol. 54, no. 5, pp. 545–550, 1935.

[33] S. H. Wright, “Determination of synchronous machine constants by test reactances, resistances, and time constants,” *Transactions of the American Institute of Electrical Engineers*, vol. 50, no. 4, pp. 1331–1350, 1931.

[34] R. Reichard, Y.-T. Lin, and M. Patel, "Core losses in synchronous machines," in *Conference Record of the 2001 IEEE Industry Applications Conference. 36th IAS Annual Meeting (Cat. No.01CH37248)*, vol. 3, pp. 1584–1590 vol.3, IEEE, 2001.

[35] K. Vogt, *Berechnung rotierender elektrischer Maschinen*. Berlin: VEB Verlag Technik, 1988.

[36] G. Traxler-Samek, T. Lugand, and M. Uemori, "Vibrational forces in salient pole synchronous machines considering tooth ripple effects," *IEEE Transactions on Industrial Electronics*, vol. 59, pp. 2258–2266, May 2012.

[37] K. Engevik, L. E. Norum, and O. B. Fosso, "Electromagnetic forces in synchronous machines: Analysis of harmonic content and air-gap geometry effects," in *Proceedings of the International Conference on Electrical Machines and Systems (ICEMS)*, pp. 1–5, IEEE, 2017.

[38] B. Cassoret, J. P. Lecointe, and J. F. Brudny, "Chapter 9: Noise and vibrations of electrical rotating machines," in *Power Electronics and Motor Drives*, CRC Press, 2011.

[39] N. L. Lundström and J.-O. Aidanpää, "Dynamic consequences of electromagnetic pull due to deviations in generator shape," *Journal of Sound and Vibration*, vol. 301, no. 1, pp. 207–225, 2007.

[40] P. Talas and P. Toom, "Dynamic measurement and analysis of air gap variations in large hydroelectric generators," *IEEE Transactions on Power Apparatus and Systems*, vol. PAS-102, no. 9, pp. 3098–3106, 1983.

[41] T. L. G. Traxler-Samek and M. Uemori, "Parasitic forces in large synchronous machines considering tooth ripple effects," in *The XIX International Conference on Electrical Machines - ICEM 2010*, pp. 1–6, 2010.

[42] M. Valavi, J. Pascal, and A. Nysveen, "Analysis of radial magnetic forces in hydrogenerators with fractional-slot windings," in *2016 XXII International Conference on Electrical Machines (ICEM)*, pp. 1318–1324, 2016.

[43] D. Zhao, “Chapter 1 - introduction of self-sustained thermoacoustic instability,” in *Thermoacoustic Combustion Instability Control* (D. Zhao, ed.), pp. 1–112, Academic Press, 2023.

[44] M. I. Friswell, J. E. T. Penny, S. D. Garvey, and A. W. Lees, *Dynamics of Rotating Machines*. Cambridge Aerospace Series, Cambridge University Press, 2010.

[45] M. L. Adams, *Rotating Machinery Vibration: From Analysis to Troubleshooting, Second Edition*. CRC Press, 2nd ed., 2009.

[46] M. Ranlöf and U. Lundin, “Form factors and harmonic imprint of salient pole shoes in large synchronous machines,” *Electric Power Components and Systems*, vol. 39, no. 9, pp. 900–916, 2011.

[47] R. W. Wieseman, “Graphical determination of magnetic fields practical applications to salient-pole synchronous machine design,” *Transactions of the American Institute of Electrical Engineers*, vol. 46, pp. 141–154, 1927.

[48] A. Bell and P. Anpalahan, “Optimisation of salient-pole rotor for synchronous generators,” in *2018 XIII International Conference on Electrical Machines (ICEM)*, pp. 339–344, 2018.